PHENOMENOLOGY AND NUMERICAL ANALYSIS OF RELAXATION PROPERTIES AND FAILURE OF MATERIALS WITH DEFECTS UNDER DYNAMIC LOADING

Final Technical Report
By

Oleg Naimark
(September, 2002)

United States Army

EUROPEAN RESEARCH OFFICE OF THE U.S. ARMY

London, England

CONTRACT NUMBER N 6871-00-M-6230

Todd McKamey

Approved for Public Release; distribution unlimited

REPORT DOCUMENTATION PAGE

Public reporting burden for this collection of information is estimated to average 1 hour per response, including the time for reviewing instructions, searching existing data sources, gathering and maintaining the data needed, and completing and reviewing this collection of information. Send comments regarding this burden estimate or any other aspect of this collection of information, including suggestions for reducing this burden to Washington Headquarters Services, Directorate for Information Operations and Reports, 1215 Jefferson Davis Highway, Suite 1204, Arlington, VA 22202-4302, and to the Office of Management and Budget, Paperwork Reduction Project (0704-0188), Washington, DC 20503

1. AGENCY USE ONLY (Leave blank)	2. REPORT DATE 2002	3. REPORT TYPE AND DATES COVERED Final 23 May-23 September

4. TITLE AND SUBTITLE
Phenomenology and numerical analysis of relaxation properties and failure of materials with defects under dynamic loading.

5. FUNDING NUMBERS
N68171-00-M-6230

$R\partial\partial$ 8936-AN-01S

6. AUTHOR(S)
Oleg Naimark

7. PERFORMING ORGANIZATION NAME(S) AND ADDRESS(ES)

Institute of Continuous Media Mechanics   1, Ak. Korolev Street
Russian Academy of Sciences   Perm 614013, Russia

8. PERFORMING ORGANIZATION REPORT NUMBER
ARL-3-2000

9. SPONSORING / MONITORING AGENCY NAME(S) AND ADDRESS(ES)

U.S. Naval Regional Contracting Center   Det. London
Covemment Buildings, Block2, Wing 12
Lime Grove, Ruislip,
Middlesex HA4 8bx England

10. SPONSORING / MONITORING AGENCY REPORT NUMBER

11. SUPPLEMENTARY NOTES

12a. DISTRIBUTION / AVAILABILITY STATEMENT

12b. DISTRIBUTION CODE

13. ABSTRACT *(Maximum 200 Words)*

Statistically based phenomenology of materials with typical mesoscopic defects is developed with the aim to link the behavior of defect ensembles with relaxation ability and failure of materials under dynamic loading and the elaboration of numerical codes for the simulation of fracture and plasticity dynamically loaded materials. Statistical approach allowed the definition of nonlinearity of thermodynamic potential and the description of plastic instability and damage localization as the generation of collective modes in defects ensemble. Experimental study was carried out to confirm the responsibility of these modes for the plastic relaxation and damage localization in dynamically loaded materials. These experiments included the framing and high speed recording of dynamics of crack propagation in PMMA, the investigation of strain-rate sensitivity of copper in the Hopkinson-bar tests, the scaling analysis of failure surfaces with the usage of the high-resolution interferometer. Original finite element code was developed and applied for the simulation of plate impact tests. The applicability of proposed phenomenology was estimated in the course of comparative analysis of plane wave propagation in copper in the framework of developed model, Bodner-Partom and Follansbee models. The analysis revealed the principal limitation of last models for the description of dynamically loaded materials due to the subjective role of the variables responsible for the defect evolution to the stress-strain variables.

14. SUBJECT TERMS
Defect induced collective modes, strain-rate sensitivity, stress wave fronts, damage localization.

15. NUMBER OF PAGES
53

16. PRICE CODE

17. SECURITY CLASSIFICATION OF REPORT	18. SECURITY CLASSIFICATION OF THIS PAGE	19. SECURITY CLASSIFICATION OF ABSTRACT	20. LIMITATION OF ABSTRACT

PHENOMENOLOGY AND NUMERICAL ANALYSIS OF RELAXATION PROPERTIES AND FAILURE OF MATERIALS WITH DEFECTS UNDER DYNAMIC LOADING

1. INTRODUCTION

During the last few decades the interrelation between structure and properties of solids has been the key problem in physics and mechanics. An extensive study of transformation of structure stimulates bridging the gap between general approaches of physics and mechanics of solids. This tendency provides the deeper insight into general laws of plasticity and failure, which can be also treated as structural transitions induced by defects.

Real solids are complex in structure defined as a hierarchy of different scale levels. Solids under loading demonstrate changes on all structural levels. On analyzing, these changes have been qualified as plastic deformation and damage processes, realized by nucleation, evolution and interaction of defects on appropriate structural levels as well as by the interaction of defects between levels. Until recently, no unified multifield theory of solids has been developed to describe a variety, complexity and interaction of processes commonly observed on all levels of structure.

To construct the model allowing for the material structure and its variation, the prime attention should be given to the choice of physical level of microstructure and, consequently to the type of defects. Furthermore, each structural level involves the results of process developed on smaller scale levels. These questions are discussed in **Section 2** and **Section 3.**

Section 4 is devoted to the development of statistical model and thermodynamics for the description of collective behavior of typical mesoscopic defects (microcracks, microshears) and the definition of specific nonlinear form of thermodynamic potential (free energy) of materials in the presence of defects.

The results of statistical consideration were used in **Section 5** and statistically based phenomenology was proposed for the description of the influence of defects on the plastic relaxation and damage-failure transition. Continuum theory of plasticity and failure was developed as specific form of free energy expansion in the term of defect induced strain (defect density tensor) that allowed the derivation of kinetic equations for defect density tensor and the description of plastic relaxation ability and damage-failure transition in the linkage with the generation of collective modes in defect ensemble. It was shown the linkage of the orientation transition in defect ensemble with plastic strain instability and the generation of "blow-up" regimes of defect kinetics as the fracture precursor. Above mentioned scenarios of defect evolution have the presentation as specific forms of self-similar solutions corresponding to the solitary wave solution of the orientation transition front and the "blow-up" dissipative structures of damage localization kinetics. These solutions represent the set of collective modes in the defect ensembles with characteristic spatial and temporal scales.

The role and the influence of these modes were studied in **Section 6** with the application to the problem of nonlinear crack dynamics (transition from the steady-state to the branching regime of crack propagation and the nature of fragmentation). It was shown that collective blow-up modes at the crack tip is the image of the daughter-cracks and represent the set of new phase variables providing qualitative new crack dynamics and scaling properties of materials. These theoretical results were supported by the direct experimental study of crack dynamics with the usage of high speed recording of stress pattern at the tip of propagating crack, the investigation of the scaling properties, recording the stress phase portraits (Poincare cross-section) at the crack tip area, and the measurement of the correlation index due to the laser profilometry and the New View scanning of fracture surface roughness.

The established self-similar nature of collective modes of defects allowed one to give in **Section 7** the interpretation of the self-similar features of spall failure and the failure wave phenomenon as the resonance excitation of blow-up damage localization zone in shocked glasses and ceramics.

Section 8 and **Section 9** are devoted to the study of the structure of stress waves in the linkage with nonlinear properties of materials induced by defects. It is shown that plastic flow can be interpreted as continuous orientation transition due to the rescaling in mesodefect ensemble, when more coarse mesodefect substructures are involved in the orientation transition. The self-similar nature of these transitions is considered as the reason for the universality of viscosity (the Sakharov data) and the steady-state plastic stress front in shocked materials (the Barker-Grady four power law of stress-strain rate relation). Developed approach allowed the interpretation of stress front in shocked materials, the explanation of the strain rate dependent range of the Hugoniot elastic limit.

The experimental study of mechanical properties of copper in the large range of the strain rates is presented in **Section 10** and **Section 11** in the linkage of above mentioned mechanisms of plastic flow with collective behavior of defect ensemble and scaling properties of collective modes.

The comparative analysis of conventionally used phenomenological models (Follansbee-MTS Model and Bodner-Partom Model) and developed model is carried out in **Section 12** and **Section 13**. It is shown the limited applicability of MTS and Bodner- Partom Models for the description of transient effects (transition from the Hugoniot to the plastic front, elastic precursor decay, plastic instability and localization) in dynamically and shock loaded materials.

2. MESODEFECT PROPERTIES

2.1. Dislocation Substructures

It is well-known, that the dislocation density increases due to the plastic deformation and the consequent changes of dislocation substructures are observed. These phenomena occur under the active loading, fatigue, creep, dynamic and shock wave loading. The consequent structure evolution has not the arbitrary but regular character. Despite the variety of the deformed materials the limited types of the dislocation substructures are observed. As it was shown in [1] the transitions in dislocation substructures have general scenario for polycrystalline materials and monocrystals. The succession in this transition is the property of the dislocation interaction and the temperature. Some times, the transition from one type of dislocation substructure to another leads to sharp changes in mechanical properties of metals and alloys. The main mechanisms of the dislocation friction (viscoplastic material responses) and the deformation hardening have the relationship to the reconstruction of dislocation substructures.

Each type of dislocation substructures exists in the corresponding range of the dislocation density and it is important that these ranges are stable for large classes of materials. The reason of such universality is related to the inherent property of dislocation ensembles as the essentially non-equilibrium system which reveals self-similarity features in the sense of characteristic nonlinear responses. This universality in the behavior of dislocation systems appears in the experiments as the low sensitivity of the evolution of dislocation structures to the external stress, but the high sensitivity to structural stresses induced by dislocation interaction.

The increase of the dislocation density is accompanied by the decrease of the distance between the dislocations and the stresses of the dislocation interaction generated on the corresponding dislocation substructures. The collective properties in dislocation ensembles begin to play the leading role in these transitions and the substructure formation.

The driving force of the reconstruction of dislocation ensembles is the tendency to reach the relative minimum of total energy due to the creation of dislocation substructures [2]. The energy of the dislocation substructure includes two parts: the own dislocation energy and the energy of the dislocation interaction. The reconstruction of the dislocation substructure leads to the change of both parts. As the consequence, the energy of new formed dislocation substructure is less than the energy of the preceding substructure.

The main part in the energy of the dislocation substructure belongs to the own dislocation energy [2]

$$\Delta U = \frac{\rho G b^2}{2\pi} \ln \frac{L}{r_0},$$ (2.1)

where ρ is the dislocation density in the dislocation substructure, b is the Burgers vector, G is the shear elastic modulus, r_0 is the radius of the dislocation nucleus, L is the screening radius of the elastic field created by the dislocations. The last scale plays the important role in the evolution of dislocation substructures: the increase of the dislocation density leads to the decrease of the L-scale in the order of the substructure succession. The typical dislocation substructures that are experimentally observed are chaotic, tangle, walls of the cells, sub-boundaries of strip substructures. The value of L is close to the grain size of chaotic substructures and has the order of the width of cell walls or high density dislocation area in strip substructures.

Under the transition to miss-oriented substructures the dislocation charges arise, that leads to the decrease of the energy of these substructures due to the turn of charge signs in their spatial distribution and, simultaneously, to the refinement of substructure parameters.

Such character of the formation of dislocation substructures reflects the self-organizing tendency of reconstruction in the dislocation ensemble. The existence of critical dislocation density corresponding to the creation of dislocation substructures was discussed in [1]. Typical values of critical dislocation density are presented in Table 1 for the copper alloys.

As usual, the appearance of the local fluctuation of dislocation density proceeds to the transformation of one substructure to another. The growth of these fluctuations leads to the change of the distribution function for the dislocation density caused by the second mode generation. These regularities of the evolution of defect substructures allow one to consider these substructures as the independent subsystem for the materials during the

deformation. In this case the list of government parameters, like temperature and stress, can be added by the order parameters related to the dislocation substructures.

Table 1. *Types of transition in dislocation substructures* [1]

Type of Transition	$<\rho_c> 10^{-10}, cm^{-2}$
Chaotic substructure → tangles	0.2
Tangles →orientated cells	0.2 – 0.5
orientated cells→ disorientated cells	0.4 – 0.6
pile-ups → homogeneous net substructure	0.2 – 0.3
disorientated cells → net substructure strips	0.5 -2
disorientated cells → strips	3.0
strips → substructure with continuous disorientation	3 – 4

It supports the view on the significance of collective effects in the dislocation ensemble and more pronounced sensitivity of the structural transformation to the current value of the dislocation density, but not to the current external stress.

These data support also the assumption concerning the essential influence of the dislocation density, as the independent variable, on the qualitative changes in the material structure and mechanical responses. The stages of deformation curves, the hardening parameter have the linkage with the transformations in the substructures.

2.2. Microcrack (Microshear) Ensemble

Of all structural levels of sub-dislocation defects, the level of microcracks and microshear may be considered as the representative for developed stage of plastic deformation and failure. The rest of defects (point defects, dislocations, dislocation pile-ups) have the smaller values of intrinsic elastic fields and energies in the comparison with microcracks and microshears. Moreover, the nucleation and growth of these defects (that are closest to the macroscopic level) are some final acts of the previous rearrangement of the dislocation substructures, when all the defects take part in the present local volume of the material.

The density of these defects reaches 10^{12}-10^{14} cm^{-3}, but each mesoscopic defect consists of a dislocation ensemble and exhibits the properties of this ensemble. Scenarios of the evolution of ensembles of these mesoscopic defects show features of non-equilibrium kinetic transitions, and experimental data obtained in a wide range stress intensities and rates of strain confirm the universality of structural evolution and its effect on relaxation properties and failure.

The typical sizes and concentration for the microcrack ensemble in different materials are represented in Table 2 [3].

Table 2

Material	l, μm		n, cm^{-3}	
	X-ray	Microscopy	X-ray	Microscopy
Aluminum	0.14	0.2	10^{11}	--
Nikel	0.08	0.1	10^{12}	$2\ 10^{12}$
Gold, silver	--	0.2	--	$2\ 10^{11}$
Copper, zinc	--	0.25	--	$5\ 10^{11}$
Beryllium	0.12	--	$5\ 10^{12}$	--
Steel 30CrMCN2A	--	0.1	--	--
NaCl	2	1-3	10^{8}-10^{9}	10^{9}
Polyetylene	--	0.015	--	$6\ 10^{15}$
Polypropylene	--	0.02	--	$7\ 10^{14}$
PMMA	--	0.02	--	$4\ 10^{12}$

The important features of the quasi-brittle fracture were established for the understanding of various stages of failure: damage, damage localization, crack nucleation and propagation. It was shown that microcracks have the dislocation nature and represent the hollow nuclei of the dislocation pile-ups. The model representation of microcrack as dislocation pile-up [4] allowed the estimation of the own microcrack energy [3,5]

$$E \approx \left[\frac{G}{V_0} \ln \frac{R}{r_0} \right] s_2, \qquad (2.2)$$

where $\vec{B} = n\vec{b}$ is the total Burgers vector; $s = B\ S_D$ is the penny-shape microcrack volume; S_D is the microcrack base; $V_0 = \frac{4}{3} r_0^3$ is the volume of the defect nuclei; r_0 is the characteristic size of the dislocation hollow (defect nuclei); R is the characteristic scale of the elastic field produced by microcrack. The estimation given in [3,4] showed that the power of the dislocation pile-up is close to $n \approx 20$.
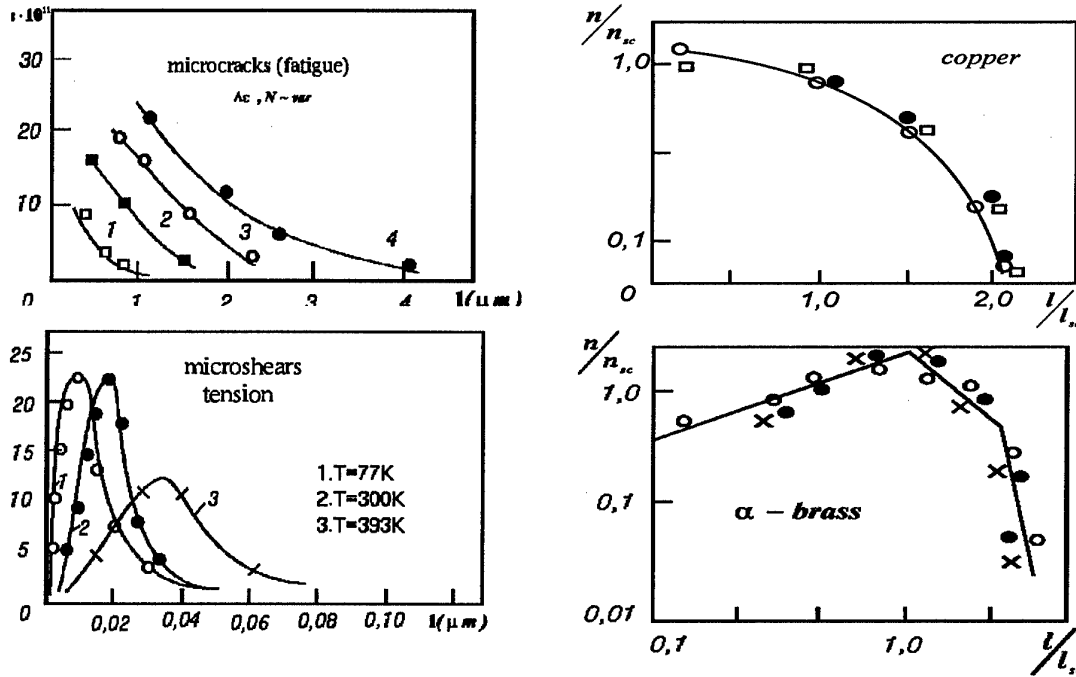

Figure 2.1. Distribution of microcracks and microshears in dimension and dimensionless coordinates: n is the microcrack concentration, l is characteristic size; n_{SC}, l_{SC} are scaling parameters [6].

Two reasons are important for the dislocation representation of microcracks. The first one is the determination of the microcrack energy as the energy of the dislocation pile-up. The second reason is the determination of microscopic parameters for the microcracks as the consequence of the symmetry change of displacement field due to the microcrack nucleation and growth. Study of the microcrack (microshear) size distribution for the different spatial scales revealed the self-similarity of the mesodefect pattern, Fig. 2.1 [6]. The statistical self-similarity reflects the invariant form of the distribution function for the mesodefects of different structural levels. This fact has important consequence for the development of the statistical multifield theory of the evolution of the defect ensemble.

3. ORDER PARAMETERS OF CONTINUUM WITH DEFECTS

3.1. Some Results of Gage Field Theory

The gage theory is presently widely used for analysis of structural and physical properties of materials with defects, being very helpful in developing continuum models of such media. The reasons for this are the follows. Nucleation and growth of defects changes the diffeomorphic structure of displacement fields. Using the formalism of gage field theory (the Yang-Mills formalism [7]), these changes can be introduced as the localization of the corresponding symmetry group of the distortion tensor and considered as additional internal coordinates that are kinematically allowed.

The structure of the so-called gage fields must correspond to the type of defects. The basis for the application of gage theory to the problem considered is the establishment of the internal symmetry group for the medium with defects. Most mechanical models of deformed continuum are invariant with the respect to the uniform groups of translations, $T(3)$, and rotations, $SO(3)$. This means that the Lagrangian of the system is invariant under the transformation

$$x \rightarrow x' = g(\xi, t) + \tau(\xi, t),$$

where x and ξ are the current and initial coordinates, $g(\xi, t)$ and $\tau(\xi, t)$ are the rotation and translation operators, respectively.

The differentiation operator is invariant with the respect to the transformations $T(3)$ and $SO(3)$, and is given by the covariant derivative

$$D_\mu x = \partial_\mu x + \Gamma_\mu x + \beta_\mu,$$

where Γ_μ and β_μ are the differential operators related to the rotation and translation [7].

For a medium with defects, the homogeneity of transformation $SO(3)$ and $T(3)$ is violated. In this case, the operators Γ_μ and β_μ correspond also to local rotations and translations related to the defects. The internal symmetry group of such a medium corresponds to the so-called semi-direct product $SO(3)\ T(3)$. The elements Γ_μ and β_μ of this group, which are functions of coordinates and time, are called the gage fields.

Another important result of applying gage theory to the medium with defects is that we can construct a Lagrangian of the medium with defects. Using the minimum expansion, we can write the Lagrangian of the system with two additional variables Γ_μ and β_μ [7]

$$L = -\frac{1}{2} C_1 g^{(1)}_{\mu\lambda} g^{(1)}_{\nu\chi} \alpha_{\mu\nu} \alpha_{\lambda\chi} - \frac{1}{2} C_2 g^{(2)}_{\mu\nu} g^{(2)}_{\nu\chi} \theta_{\mu\nu} \theta_{\lambda\chi}, \qquad (3.1)$$

where

$$\theta_{\mu\nu} = \partial_\mu \Gamma_\nu - \partial_\nu \Gamma_\mu + \Gamma_\mu \Gamma_\nu - \Gamma_\nu \Gamma_\mu,$$
$$\alpha_{\mu\nu} = \partial_\mu \beta_\mu - \partial_\nu \beta_\nu + \Gamma_\mu \beta_\nu - \Gamma_\nu \beta_\mu + \theta_{\mu\nu} x$$

are the so-called intensities of the gage fields related to the local rotations and translations due to the presence of defects; g_{ik} are the components of the metrical tensor.

The phenomenological parameters C_1 and C_2 in the Lagrangian L are the constants of dislocation interaction. Expression (3.1) for the Lagrangian will future be used in our analysis of the statistical properties of the ensembles of defects.

3.2. Microscopic and Macroscopic Variables for Microcracks (Microshears) Ensemble

Structural parameters associated with microcracks and microshears were introduced [3] as the derivative of the dislocation density tensor. These defects are described by symmetric tensors of the form

$$s_{ik} = s v_i v_k \qquad (3.2)$$

in the case of microcracks and

$$s_{ik} = 1/2s(v_i l_k + l_i v_k) \qquad (3.3)$$

for microshears. Here $\vec{v}$ is unit vector normal to the base of a microcrack or slip plane of a microscopic shear; $\vec{l}$ is a unit vector in the direction of shear; s is the volume of a microcrack or the shear intensity for a microscopic shear.

The change of the diffeomorphic structure of the displacement field due to these defects has also important consequences from point of view of the symmetry change of the system "solid with defects". This symmetry aspect can be used to model arbitrary defects both in crystalline and amorphous materials without the assumption concerning the dislocation nature of the defects that originally is the property of crystalline materials.

The average of the "microscopic" tensor s_{ik} gives the macroscopic tensor of the microcrack or microshear density

$$p_{ik} = n\langle s_{ik} \rangle, \qquad (3.4)$$

that coincides with the deformation caused by the defects, n is the defect concentration.

4. STATISTICAL MODEL OF CONTINUUM WITH DEFECTS

4.1. Effective Field Method

The effective field method is frequently used to refer to any auxiliary field (real or virtual) introduced into a theoretical model in order to construct a simplified way of taking into account the effect of complicated factors like interparticle interactions, which are either too difficult to evaluate rigiriously or are even not yet clear in detail.

In our consderation the reference to the «effective field method» means that we use the concept of an auxiliary external multicomponent field, constructed in such a way that in addition of the corresponding term to the Hamiltonian of the system under consideration makes it state an equilibrium one at any given instant in time. This simple idea has proved itself as a useful approximation or the treatment of a number of problems.

The effective field method was reintroduced in [8] into statistical physics a fruitful physical idea put forward in thermodynamics by Leontovich [9]. According to Leontovich for an arbitrary nonequilibrium state of any thermally uniform system, that is characterized by definite values of internal parameters, the transition into the equilibrium state with the same values of those internal parameters may be performed by introducing an additional force field. By definition, the entropy of this nonequilibrium state is equal to the entropy of the equilibrium (being that due the presence of the additional force field) state characterized by the same values of the considered material parameters.

The microscopic kinetics for the parameter s_{ik} is determined by the Langevin equation

$$\dot{s}_{ik} = K_{ik}(s_{lm}) - F_{ik} \qquad (4.1)$$

where $K_{ik} = \partial E/\partial s_{ik}$, E is the energy of the defect and F_{ik} is a random part of the force field and satisfies the relations $\langle F_{ik}(t) \rangle = 0$ and $\langle F_{ik}(t')F_{ik}(t) \rangle = Q\delta(t - t')$. The parameter Q characterizes the mean value of the energy relief of the initial material structure (the energy of defect nuclei).

Statistical model of the defect ensemble was developed in the terms of the solution of the Fokker-Plank equation in [2,3]

$$\frac{\partial}{\partial t} W = -\frac{\partial}{\partial s_{ik}} K_{ik} W + \frac{1}{2} Q \frac{\partial^2}{\partial s_{ik} \partial s_{ik}} W ,$$ (4.2)

According to the statistical self-similarity hypothesis the distribution function of defects can be represented in the form $W = Z^{-1} \exp\left(-\frac{E}{Q}\right)$, where Z is the normalization constant. As it follows from (4.2) the statistical properties of the defect ensemble can be described after the determination of the defect energy E and the dispersion properties of the system given by the value of Q.

In the term of the microscopic and macroscopic variables and according to the presentation of these mesodefects as the dislocation substructure the energy of these defects (the Lagrangian) can be written in the form

$$E = E_0 - H_{ik} s_{ik} + \alpha s_{ik}^2 ,$$ (4.3)

where the quadratic term represents the own energy of defects (2.2) and the term $H_{ik} s_{ik}$ describes the interaction of the defects with the external stress σ_{ik} and with the ensemble of the defects in the effective field approximation:

$$H_{ik} = \sigma_{ik} + \lambda p_{ik} = \sigma_{ik} + \lambda n \langle s_{ik} \rangle ,$$ (4.4)

where α, λ are the material constants. The average procedure gives the self-consistency equation for the determination of the defect density tensor

$$p_{ik} = n \int s_{ik} W(s, \vec{v}, \vec{l}) ds_{ik} .$$ (4.5)

For the dimensionless variables $\hat{p}_{ik} = \frac{1}{n} \sqrt{\frac{\alpha}{Q}} \, p_{ik}, \ \hat{s}_{ik} = \sqrt{\frac{\alpha}{Q}} \, s_{ik}, \ \hat{\sigma}_{ik} = \frac{\sigma_{ik}}{\sqrt{Q\alpha}}$ self-consistency equation has the form

$$\hat{p}_{ik} = \int \hat{s}_{ik} Z^{-1} \exp\left((\hat{\sigma}_{ik} + \frac{1}{\delta} \hat{p}_{ik}) \hat{s}_{ik} - \hat{s}_{ik}^2 \right) d\hat{s}_{ik} ,$$ (4.6)

that includes the single dimensionless material parameter $\delta = \frac{\alpha}{\lambda n}$. The dimension analysis allowed us to estimate that

$$\alpha \sim \frac{G}{V_0}, \lambda \sim G, n \sim R^{-3}$$

Here G is the elastic modulus, $V_0 \sim r_0^3$ is the mean volume of the defect nuclei, R is the distance between defects. Finally we obtain for δ the value $\delta \sim \left(\frac{R}{r_0}\right)^3$ that is in the correspondence with the hypothesis concerning the statistical self-similarity of the defect distribution on the different structural level.
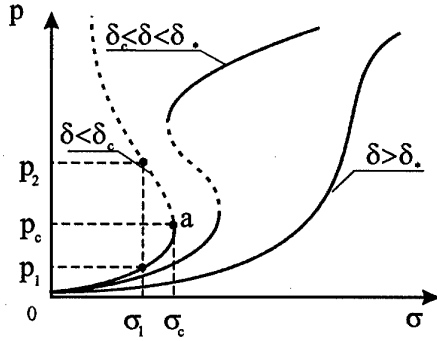
7

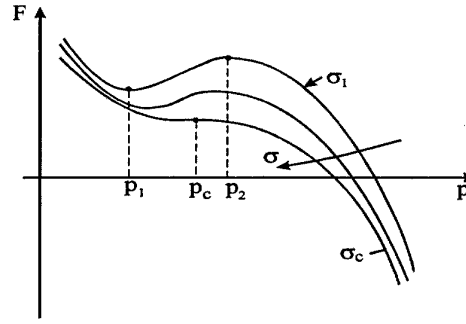*Figure 4.1. Characteristic responses of materials on defect growth.*

Figure 4.2. Free energy dependence on stress and defect density for $\delta < \delta_c \approx 1$.

The solution of the self-consistency equation (4.6) was found for the case of the uni-axial tension and simple shear [2], (Fig.4.1). The existence of characteristic nonlinear behavior of the defect ensemble in the corresponding ranges of δ ($\delta > \delta_* \approx 1.3$, $\delta_c < \delta < \delta_*$, $\delta < \delta_c \approx 1$) was established, where δ_c and δ_* are the bifurcation points. It was shown [3,4] that the above ranges of δ are characteristic for the quasi-brittle ($\delta < \delta_c \approx 1$), ductile ($\delta_c < \delta < \delta_*$) and nanocrystalline ($\delta > \delta_* \approx 1.3$) responses of materials. It is evidence from this solution that the behavior of the defect ensemble in the different ranges of δ is qualitative different. The replace of the stable material response for the fine grain materials to the metastable one for the ductile materials with the intermediate grain size occurs for the value of $\delta = \delta_* \approx 1.3$, when the interaction between the orientation modes of the defects has more pronounced character. It means that the metastability has the nature of the orientation ordering in the defect ensemble. It will be shown in Section 8 that continuous orientation transition due to the growth of the defect density (and, as the consequence, the decrease of δ) provides the specific mechanism of the momentum transfer that is conventionally known as the plastic flow. As it will be discussed in Section 6 the range of $\delta < \delta_c \approx 1$ provides the specific non-linear kinetics of defect evolution, which leads to the nucleation of failure hotspots.

5. COLLECTIVE PROPERTIES OF ENSEMBLES OF DEFECTS

5.1. Phenomenology of Solid with Defects. Free Energy.

The statistical description allowed us to propose the phenomenology of solid with defects based on the appropriate presentation of the free energy form F. Taking in view that Eqn.4.5 corresponds to the equation $\partial F / \partial p = 0$, the simple phenomenological form of the part of the free energy caused by defects (for the uni-axial case $p = p_{zz}, \sigma = \sigma_{zz}, \varepsilon = \varepsilon_{zz}$) is given by the six order expansion, which is similar to the well-known Ginzburg-Landau expansion [11].

$$F = \frac{1}{2} A(1 - \frac{\delta}{\delta_*})p^2 - \frac{1}{4} Bp^4 + \frac{1}{6} C(1 - \frac{\delta}{\delta_c})p^6 - D\sigma p + \chi(\nabla_l p)^2. \tag{5.1}$$

The bifurcation points δ_*, δ_c play the role that is similar to the characteristic temperatures in the Ginzburg-Landau expansion in the phase transition theory. The gradient term in (5.1) describes the non-local interaction in the defect ensemble in the so-called long wave approximation; A, B, C, D and χ are the phenomenological parameters.

The defect kinetics is determined by the evolution inequality [5]

$$\frac{\delta F}{\delta t} = \frac{\delta F}{\delta p} \frac{dp}{dt} \leq 0 \tag{5.2}$$

that leads to the kinetic equation for the defect density tensor

8

$$\frac{dp}{dt} = -\Gamma\left(A(1-\frac{\delta}{\delta_*})p - Bp^3 + C(1-\frac{\delta}{\delta_c})p^5 - D\sigma - \frac{\partial}{\partial x_l}(\chi\frac{\partial p}{\partial x_l}) \right),$$ (5.3)

where Γ is the kinetic coefficient.

Kinetic equation (5.3) and the equation for the total deformation

$$\varepsilon = \hat{C}\sigma + p$$ (5.4)

($\hat{C}$ is the component of the elastic compliance tensor) represent the system of the constitutive equations of solid with considered types of the defects.

5.2. Collective Properties of Defect Ensemble

As it follows from the solution of (4.5), presented in Fig. 4.1, transitions through the bifurcation points δ_c and δ_* lead to a sharp change in the symmetry of the distribution function as a result of the appearance of some orientationally pronounced macroscopic modes of the tensor p_{ik}. The effect of transitions on the evolution of the defect ensemble is determined by the type of bifurcation - the group properties of the kinetic equation for the tensor p_{ik} for different domains of $\delta(\delta > \delta_*, \delta < \delta_*, \delta < \delta_c)$. The qualitative relationships governing the changes in the behavior of the system are reflected in Fig.5.1 in the form of families of heteroclines, which are the solutions of equation

$$A\left(1-\frac{\delta}{\delta_*}\right)p - Bp^3 + C\left(1-\frac{\delta}{\delta_c}\right)p^5 - D\sigma - \frac{\partial}{\partial x_l}\left(\chi\frac{\partial p}{\partial x_l}\right) = 0.$$ (5.5)

In the region $\delta > \delta_*$ this equation is of the elliptic type with periodic solutions with spatial scale Λ and possesses p anisotropy determined mainly by the applied stress. This distribution of p gives rise to weak pulsations of the strain field. As $\delta \to \delta_*$ the solution of Eqn. 5.5 passes the separatrix S_2, and the periodic solution transforms into a solitary-wave solution. This transition is accompanied by divergence of the inner scale $\Lambda : \Lambda \approx -\ln(\delta - \delta_*)$. In this case the solution has the form $p(\zeta) = p(x - Vt)$. The wave amplitude, velocity and the width of the wave front are determined by the parameters of non-equilibrium (orientation) transition:

$$p = \frac{1}{2}p_a[1 - tahn(\zeta l^{-1})] \, l = \frac{4}{p_a}\left(2\frac{\chi}{A}\right)^{\frac{1}{2}}.$$ (5.6)

The velocity of solitary wave is $V = \chi A(p_a - p_m)/2\zeta_2$, where $(p_a - p_m)$ is the jump in p in the course of an orientational transition. A transition through the bifurcation point δ_c (separatrix S_3) is accompanied by the appearance of spatio-temporal structures of a qualitatively new type characterized by explosive accumulation of defects as $t \to t_c$ in the spectrum of spatial scales («blow-up» regime) [12, 13]. In this case the kinetics of p is determined by the difference of the power of the terms in the expansion (5.1).
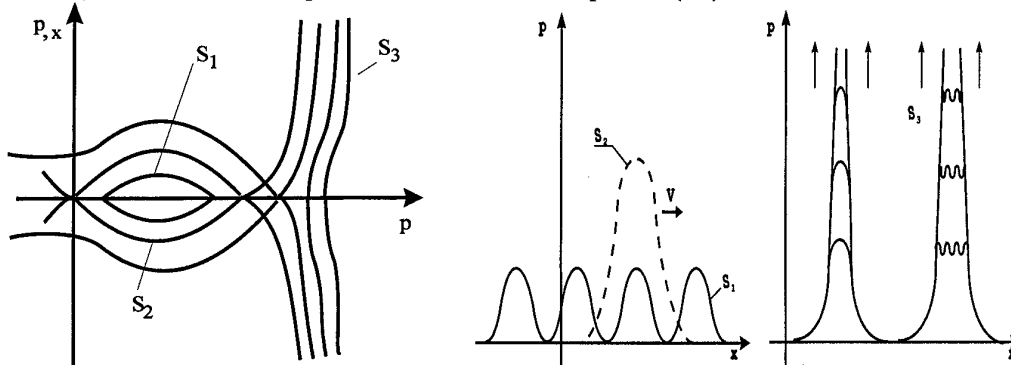

Figure 5.1. Types of heteroclines and the corresponding characteristic forms

9

Assuming a power-law dependence of the nonlocality parameter on p, the kinetic equation (5.3) can be written in the form

$$\frac{\partial p}{\partial t} \approx S(p_c)p^{\omega} + \frac{\partial}{\partial x}\left(\chi_0(p_c)p^{\beta}\frac{\partial p}{\partial x}\right),$$

(5.7)

where $\omega = 5/3$. It is shown in [12, 13] that for this type of the equations the developed stage of kinetics of p in the limit $t \to t_c$ can be described by a self-similar solution

$$p(x,t) = \phi(t)f(\zeta), \quad \zeta = \frac{x}{L_c}, \quad \phi(t) = \Phi_0\left(1 - \frac{t}{t_c}\right)^{-m},$$

(5.8)

where $m > 0$, $\Phi_0 > 0$ are the parameters related to the nonlinear form of Eqn. 5.3; L_c and t_c are the scaling parameters. The function $f(\zeta)$ is determined by solving the corresponding eigenvalue problem. For example, for the case $\omega = \beta + 1$ the self-similar solution of Eqn. 5.7 has the form

$$p(x,t) = [S(t - t_c)]^{-\frac{1}{\beta}}\left(\frac{2(\beta+1)}{\beta(\beta+2)}\sin^2\left(\frac{\pi x}{L_c} + \pi\theta\right)\right)^{\frac{1}{\beta}},$$

(5.9)

where θ is a random value in the interval (0,1). The scale L_c, the so-called fundamental length [13], has the meaning of a spatial period of the solution (5.8)

$$L_c = \frac{2\pi}{\beta}\left((\beta+1)\chi_0 S^{-1}\right)^{\frac{1}{2}}.$$

The self-similar solution (5.8) describes the blow-up damage kinetics for $t \to t_c$ on the set of spatial scales $L_H = kL_c$, $k = 1,2,...K$. The blow-up kinetics of damage localization allowed us to link the hotspots of failure with the above mentioned self-similar structures.

6. COLLECTIVE BEHAVIOR OF CRACKS AND DEFECTS

6.1. Introductory Remarks

The interaction of the main crack with the ensemble of the defects is the subject of intensive experimental and theoretical studies that revealed some unresolved puzzles in the quasi-brittle failure. The long-standing problem is the limiting velocity of a crack. The linear elastic theory predicted that a crack should continuously accelerate up to the Rayleigh wave speed, V_R, however, the experiments on a number of brittle materials [14] showed that the crack will seldom reach even the half of this value. A view of the dissipation process was suggested in [5, 15] where the main role in the explanation of qualitative new mentioned effects was assigned to the collective modes of the defect ensemble and the interaction of these modes with a moving crack. In the present paper we will discuss the phenomena investigated intensively during the past decade under the study of nonlinear dynamics of crack propagation. These phenomena demonstrate the qualitative new features of a crack behavior caused by the interaction of the crack with the ensemble of defects in the so-called the process zone.

The rebirth of interest in the issue of dynamic fracture is observed during last decade due to the variety of new experimental results which are not explainable within the prediction of classical fracture mechanics, where it was shown that the crack in infinite plane specimen has two steady-state velocities: zero and the Rayleigh speed [16]. The recent experimental study revealed the limiting steady state crack velocity, a dynamical instability to micro-branching [16, 17], the formation of non-smooth fracture surface [18], and the sudden variation of fracture energy (dissipative losses) with a crack velocity [19]. This renewed interest was the motivation to study the interaction of defects at the crack tip area (process zone) with a moving crack. The still open problem in the crack evolution is the condition of crack arrest that is related to the question whether a crack velocity smoothly approaches to zero as the loads is decreased from large values to the Griffith point [20]. There

is also problem at the low end of crack velocity. How a crack that is initially at rest might achieve its steady-state.

6.2. Some Results in Crack Mechanics

The subject of the rapid propagation of crack in a brittle material is one whose roots go back to the classical works of Griffith and Mott [22,23]. Since that time a great deal of both analytical and experimental work [24,25,26] has been dedicated to understanding the phenomenon of fracture, where the behavior of crack driven by externally imposed stresses is studied. With a goal to study the crack stability problem and the interaction of the main crack with the defect ensemble in the process zone we will consider briefly the classical results in the crack mechanics were much analytical progress has been made in assuming that the medium behaves according to the equations of linear elasticity. The important step to model the brittle failure was made by Griffith [22] when the additional characteristics of the crack resistance were introduced in the form of the energy of the development of the new surface at the crack tip. According to the Griffith theory the energy U of elastic materials with a crack is represented in the form (Fig.6.1, curve 1)

$$U = -\frac{\sigma^2}{2G}\left(\frac{\pi a^2}{4}\right) + 2\gamma a,$$

(6.1)

where γ is the surface energy; σ is the applied stress; a is the crack length; G is the elastic modulus.
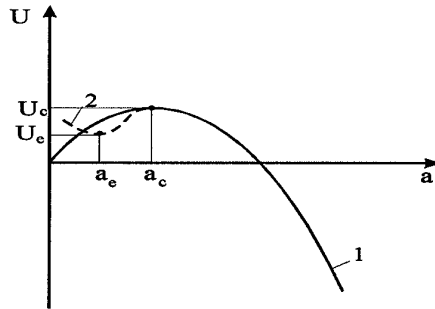

Figure 6.1. The Griffith (1) and Fraenkel (2) energy form of elastic solid with a crack.

Irwin [24] developed the Griffith conception and proposed the force version of the crack stability to introduce the stress intensity factor

$$K_I = \sigma\sqrt{\pi a} \ .$$

(6.2)

Barenblatt [25] proposed a variant of the force version of the crack stability that reflects another view on the role of stress in the crack tip area. It was assumed the existence at the crack tip over the area $0 < s < d$ of the cohesion forces $G_B(s)$. These forces have the molecular nature and divert the singularity of the stress field.

Two hypothesis were assumed in the Barenblatt approach:

small size of the crack tip zone in comparison with the crack length ($\frac{d}{a} \ll 1$);

autonomous behavior of crack tip, i.e. the self-similar evolution of the crack tip in the steady-state regime.

This hypothesis is in correspondence with the properties that reveal quasi-brittle materials. The self-similarity features of the crack tip evolution are the consequence of the small ratio of the applied stress σ and the cohesion force $G_B : \frac{\sigma}{G_B} \ll 1$. This fact reflects the intermediate-asymptotic character of quasi-brittle failure theories and the material parameter was introduced, the so-called the cohesive modulus, as the independent strength property of materials: $K_B = G_B\sqrt{d}$. Despite the similar form of the cohesive modulus K_B and the stress intensity factor K_I there is a difference between the Irwin criteria and the cohesive modulus

11

proposed by Barenblatt. The cohesive modulus determines the steady-state character of crack propagation, but not the catastrophic one corresponding to the Griffith-Irwin approach. The qualitative difference between above mentioned approaches can be shown taking in view the remarks by Fraenkel [27] under the critical analysis of the Griffith approach. Fraenkel wrote that the physically realistic form of the energy U must contain the local minimum $U_e(a_e)$ (Fig.6.1, curve 2). The difference in the energy $\Delta U = U_c - U_e$ determines the work of the stress field at the crack tip under transition from the steady-state to the unstable regime of crack propagation. This work provides the surmount of this energy barrier. It is natural to assume that the cohesive modulus is the force version of this energy barrier. We will show in the following that the metastable energy form, assumed by Fraenkel, has the relationship to the collective behavior of the defect ensemble in the process zone and to the interaction of the defects with the main crack.

6.3. Origin of Crack Instability

The classic theory of fracture treats a cracks as mathematical branch cuts which begin to move when an infinitesimal extension of the crack releases more energy then it is needed to create fracture surface. This idea is successful in some cases in practice but conceptually incomplete. The experiments fail to confirm this idealized picture. The surface created by the crack is not necessarily smooth and flat. In a series of experiments on the brittle fracture the simultaneous propagation of an ensemble of microcracks, instead of a single propagating cracks, was observed [15]. The fracture process was viewed as a coalescence of defects situated in the crack path; the mean acceleration drops, the crack velocity develops oscillations and a structure is formed on the fracture surface [17,18,19,20]. As the branches grow in size, they evolve into macroscopic large scale crack branches.

A theoretical explanation of the limited steady-state crack velocity and the transition to branching regime was proposed in [28,29,30] due to the study of collective behavior of the microcrack ensemble in the process zone. It was shown by the solution of evolution equation for the defect density tensor that the kinetics of microcracks accumulation at the final damage stage includes the generation of spatial-temporal structures (dissipative structures with blow-up damage kinetics) that is the precursor of the nucleation of the "daughter" cracks. The kinetics of the daughter crack generation is determined by two parameters, which are given by the self-similar solution (5.8)

$$p(x,t)=\phi(t)f(\zeta),\zeta=\frac{x}{L_c},\phi(t)=\Phi_0(1-\frac{t}{t_c})^{-m}, \qquad (6.3)$$

where L_c and t_c are the scaling parameters which can be found under the solution of the corresponding nonlinear eigen-function problem [12,13,29]. These parameters are the spatial scales L_C of the blow-up damage localization and the so-called "peak time" t_c, which is the time of damage localization in the self-similar blow-up regime. The velocity limit V_C of the transition from the steady-state to the irregular crack propagation is given by the ratio: $V_C \approx L_C/t_c$. As it was shown in Section 5 the set of spatial scales L_H (daughter crack sizes) is proportional to L_C and represents new set of independent coordinates (collective modes of the defect ensemble) of the nonlinear system for $\sigma > \sigma_c$. These coordinates characterize the property of a second attractor that could subject the behavior of the nonlinear system. The first attractor corresponds to the well-known self-similar solution (6.2) for the stress distribution at the crack tip that is the background for the stress intensity factor conception. This solution is available in the presence of the metastability (local minimum) for p in the range $\sigma < \sigma_c$.

The steady-state crack propagation is realized in the case when the stress rise in the process zone provides the failure time $t_f > t_c = \frac{L_c}{V_C}$ for the creation of the daughter crack only in the straight crack path. The failure time t_f follows from the kinetic equation (5.3) and represents the sum of the induction time t_i (the time of the approaching of the defect distribution to the self-similar profile on the $L_H = kL_c$ scales) and the peak time t_c: $t_f = t_i + t_c$. For the velocity $V < V_C$ the induction time $t_i >> t_c$ and the daughter crack appears only along the initial main crack orientation. For the crack velocity $V \approx V_C$ there is a transient regime ($t_i \approx t_c$) of the creation of number of the localization scales (daughter cracks) in the main crack path. The crack velocity growth in the area $V > V_C$ leads to the sharp decrease of the induction time $t_i \rightarrow 0$, $t_f \rightarrow t_c$ that is accompanied by the extension of the process zone in both (tangent and longitudinal) directions where the multiple blow-up structures (daughter cracks) and, as the consequence, the main crack branching appears. The last situation is qualitatively

similar to the resonance excitation of the numerous mirror zones under the spall condition but in the non-uniform stress field in the range of angle with $\sigma > \sigma_c$.

6.4. Experimental Study of Nonlinear Crack Dynamics

Experimental setup

Direct experimental study of crack dynamics in the preloaded PMMA plane specimen was carried out with the usage of a high speed digital camera Remix REM 100-8 (time lag between pictures $10 \, \mu s$) coupled with photo-elasticity method, Fig. 6.2 [29,30,31].
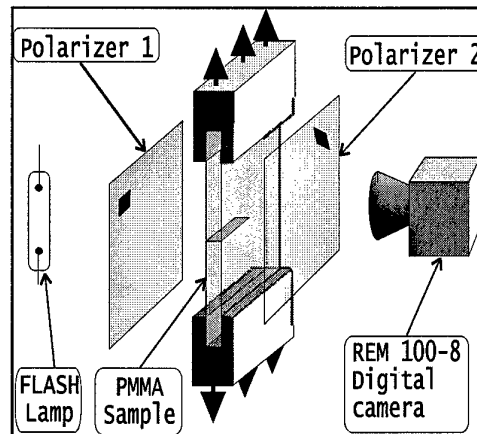

Figure 6.2.   Scheme of experiment

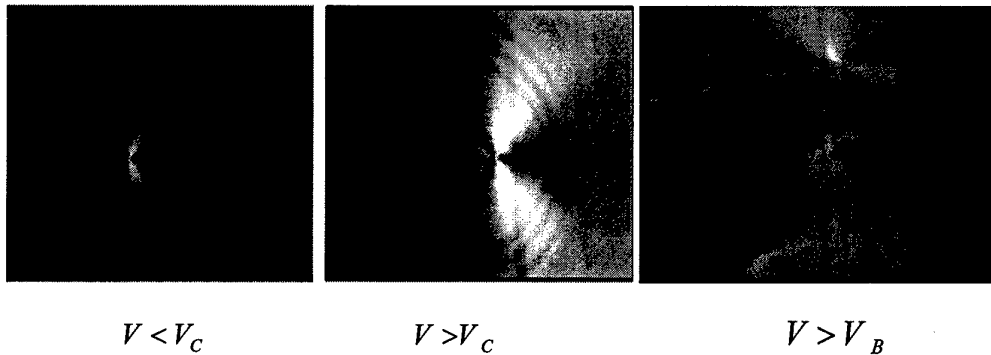$$V < V_C \qquad\qquad V > V_C \qquad\qquad V > V_B$$

Figure 6.3. Different regimes of crack dynamics.

The pictures of stress distribution at the crack tip is shown in Fig.6.3 for slow ($V < V_C$) and fast ($V > V_C$) cracks. The experiment revealed that the path of the critical velocity V_C is accompanied by the appearance of a stress wave pattern produced by the daughter crack growth in the process zone. Independent estimation of critical velocity from the direct measurement of crack tip coordinates and from pronounced stress wave Doppler pattern gives a correspondence with the Fineberg data ($V_C \approx 0.4 V_R$) [16].

Characteristic crack velocity

The dependence of crack velocity on the initial stress is represented in Fig.6.4.
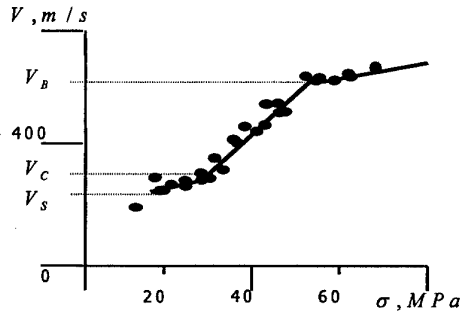
13

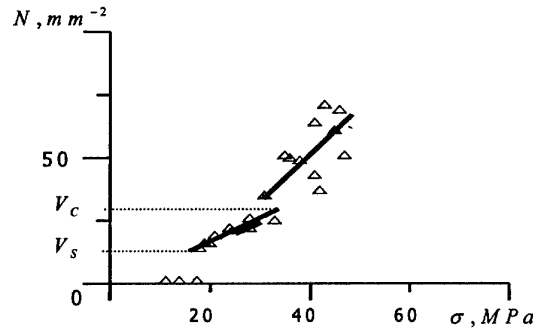*Figure 6.4. Crack velocity versus applied stress*

Figure. Figure 6.5. Mirror zone concentration versus applied stress

Three portions with different slopes can be shown. The existence of these portions determines three characteristic velocities: the velocity of the transition from the steady-state to the non-monotonic straight regime $V_S \approx 220\,m/s$, the transient velocity to the branching regime $V_C \approx 330\,m/s$ and the velocity $V_B \approx 600\,m/s$ when the branches behave autonomous.

The characteristic velocity $V_C \approx 330\,m/s$ allowed us to estimate the peak time t_c to measure the size of the mirror zone $L_C \approx 0.3\,mm$: $t_c = \dfrac{L_C}{V_C} \approx 1 \cdot 10^{-6}\,s$. This result allowed also the explanation of the linear dependence of the branch length on the crack velocity [20]. Actually, since the failure time for $V > V_C$ is approximately constant ($t_f \approx t_c \approx 1\mu s$), there is a unique way to increase the crack velocity to extend the size of the process zone. The crack velocity V is linked with the size of the process zone L_{PZ} by the ratio $V = \dfrac{L_{PZ}}{t_c}$.

In our experiments the dependence of the density of the localized damage zone on the stress was observed (Fig.6.4). Since the branch length is limited by the size of the process zone, we obtain the linear dependence of branch length on the crack velocity. This fact explains the sharp dependence (quadratic law) of the energy dissipation on the crack velocity established in [20].

Scaling Properties of Failure

The scaling properties of failure has spurred great interest in the context of the general problem of disordered media when the self-affinity of the failure surface was established in the terms of the universality of the so-called roughness exponent. The self-affinity of the fracture surface was established first by Mandelbrot [32] as the existence of the power law of the distance r measured within the horizontal plane for the points at which the heights $h(r)$ are measured. This defines the surface-roughness index ζ as $h(r) \propto r_\zeta$. Experimental data of the past decades on the measurement of the roughness exponent revealed the self-affinity of the fracture surface and it was established that the pattern of the fracture surface can be considered as scale invariant objects with the roughness index $\zeta \approx 0.8 \pm 0.05$ [33]. This fact allowed the determination of the length scales $r > r_0$ where the roughness exponent is the invariant. The range of scales $r > r_0$ for many materials show the universal scaling properties (the roughness exponent $\zeta \approx 0.8$). For the scales $r < r_0$ the roughness exponent can change.

The scale invariant properties for $r > r_0$ means the transition from the roughness statistics caused by the initial structural heterogeneity (size of blocks, grains) to the statistics given by the collective properties of defects under transition from damage to fracture.

In our experiments the roughness profile was determined for the PMMA fracture surface (Fig. 6.6) using the laser scanner system. Fracture surface analysis revealed the correspondence of the sharp change of the crack dynamics for the velocities V_C and V_B, and the fractographic pattern. The fractographic image of the fracture surface was studied in the velocity range $V \sim 300 - 800\,m/s$ when different regimes of the crack propagation were observed.
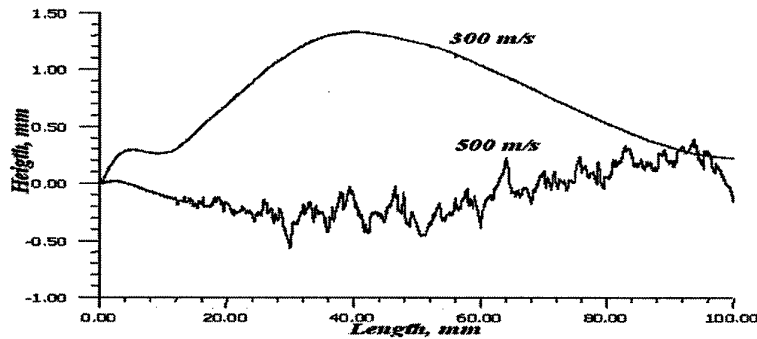
Figure 6.6. The roughness of failure surface in PMMA

The first regime $V \sim 220-300 \, m/s$ is characterized by the mirror surface pattern (Fig.6.7). The increase of the crack velocity in this range leads to characteristic pattern on the mirror surface in the form of the so-called conic markings [34]. The conic markings are the traces of the junctions of the main crack and the damage localization zones that nucleate in the process zone. These data reflect the influence of the damage kinetics on the characteristic size of above mentioned failure structures on the surface.
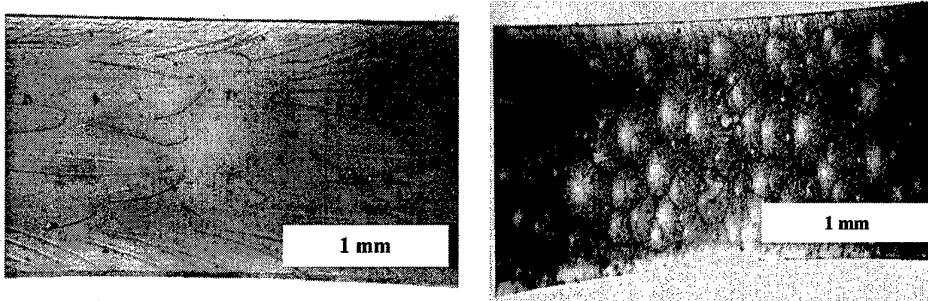

Figure 6.7. Failure surface for slow $(V < V_C)$ and fast $\left(V_B > V > V_C\right)$ crack

The second regime appears in the velocity range $300-600 \, m/s$ and the surface pattern includes the numerous mirror zones.

The analysis of the roughness data in the term of the roughness exponent showed the dependence of the scaling properties on the regime of crack propagation. However, the group of specimen was found with the exponent $\zeta \approx 0.8$. This fact allowed us to assume the existence of the regime of crack propagation with universal scaling index close to $\zeta \approx 0.8$. The existence of different scaling indexes for other regimes of crack propagation reflects the variety of the behavior of investigated nonlinear system. As it was shown, the crack dynamics in quasi-brittle materials is subject to two attractors. The first attractor is given by the intermediate asymptotic solution of the stress distribution at the crack tip. The self-similar solution (9) describes the blow-up damage kinetics on the set of spatial scales and determines the properties of the second attractor. This attractor controls the system behavior for $V > V_B$ when there is a range of angles with $\sigma > \sigma_c$. The universality of the roughness index can be considered also as the property of this attractor. In the transient regime $V_B > V > V_C$ the influence of two attractors can appear. This reason can be considered as a mechanism of the dispersion of experimentally measured roughness on the scale $r > r_0$.
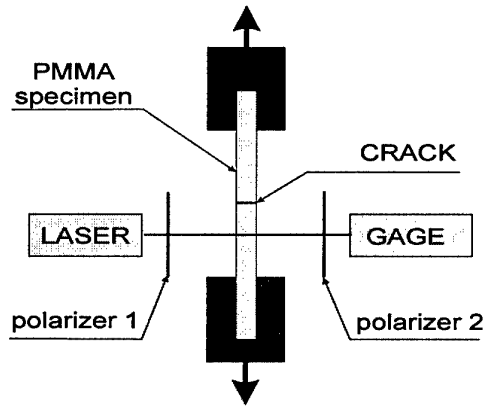
Figure 6.8. Scheme of stress phase portrait recording

The scaling properties of failure were studied also under the recording of the stress dynamics using the polarization scheme coupled with the laser system, Fig.6.8.

a

b
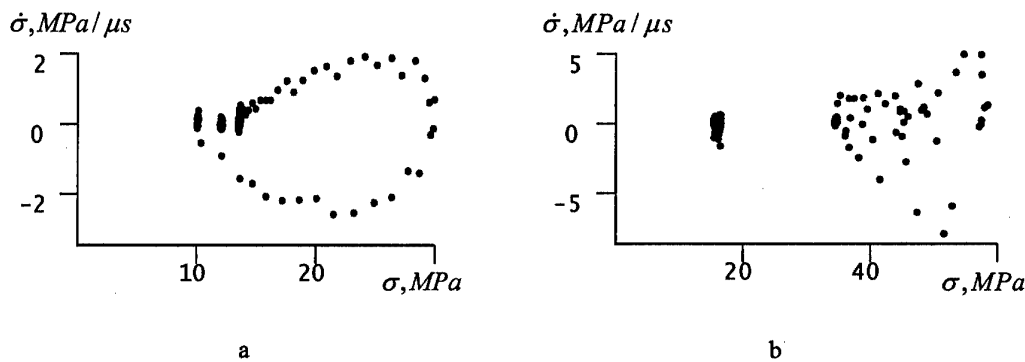
Figure 6.9. The Poincare cross-section for the phase variables $\dot{\sigma} \sim \sigma$:
$$a - V = 200\,m/s, \quad b - V = 615\,m/s$$

The stress temporal history was measured in the marked point deviated from the main crack path on the fixed (4 mm) distance. This allowed us to investigate the correlation property of the system using the stress phase portrait $\dot{\sigma} \sim \sigma$ for slow and fast cracks, Fig.6.9. These portraits display the periodic stress dynamics (Fig.6.9a) that in the correspondence with the local ellipticity of Eqn.5.3 for $\sigma < \sigma_c$ ($V < V_c$) and the stochastic dynamics (Fig.6.9b) for $V > V_c$ corresponding to the second type of the attractor. In the transient regime $V \approx V_c$ the coexistence of two attractors can appear that can lead to the intermittency effect as the possible reason for the scaling index dispersion.

Figure 6.10. The stress history

Figure 6.11. Correlation integral

16

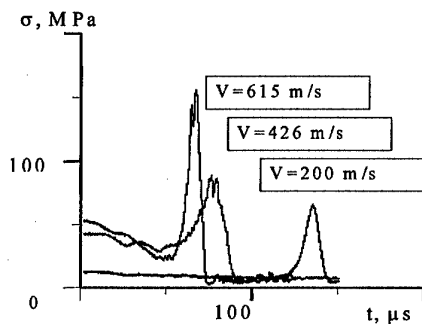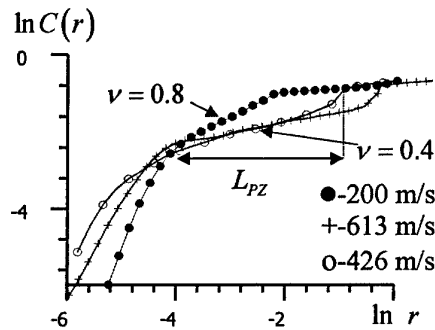The recording of the temporal stress history in the marked point for $V > V_C$ revealed the appearance of finite amplitude stress fluctuations, which reflect the qualitative new structural changes in the process zone for the fast crack (Fig.6.10). The scaling properties as the above attractor properties were studied in the term of the correlation integral calculated from the stress phase pattern using the formula [35]

$$C(r) = \lim_{m \to \infty} \frac{1}{m2} \sum_{i,j=1}^{m} H(r - |x_i - x_j|) \approx r^{\nu},$$

where x_i, x_j are the coordinates of the points in the $\dot{\sigma} \sim \sigma$ space, $H(...)$ is the Heaviside function. The existence of the scales $r > r_0$ with the stable correlation index was established for the regimes $V < V_C$ and $V_B > V > V_C$, Fig.6.11. The values of the correlation indexes in these regimes show the existence of two scaling regimes with the deterministic ($V = 200 m/s$, $\nu \approx 0.8$) and stochastic ($V = 426, 613 m/s$, $\nu \approx 0.4$) dynamics. The extension of the portions with the constant indexes determines the scale of the process zone L_{PZ}. The length of the process zone increases with the growth of the crack velocity in the range $V_B > V > V_C$ with the maintain of the scaling property of the dynamic system. Numerical simulation of the damage kinetics in the process zone allowed us to conclude that this scaling is the consequence of the subjection of the failure kinetics to the blow-up self-similar solution which determines the collective behavior of the defect ensemble in the process zone [29,30,31].

6.5. Low Velocity Limit. Crack Arrest

In this part we have addressed the question of how a dynamic crack will approach zero velocity. This fact was discussed in [21] and it was shown considering a simplified version of the strip specimen with the radiation at the boundaries that steady-state velocity law with a square-rot behavior is expected as a function of the excess load over the Griffith load. This means that the steady-state velocity increases with an infinite slope near zero overload, but in a smooth fashion with a load. It was shown also that if the crack has no field inertia, the pass of the "trapping limit" will lead to the crack move. But if the crack has a field inertia the crack velocity will exhibit a transient oscillation. The similar conclusion can be made to compare the estimation of the crack velocity, given in [21] $V = w\sqrt{(E_e - 2\gamma)/(C(w))}$, where w is the Barenblatt cohesive zone of the crack, $(E_e - 2\gamma)$ is the Griffith static term, $C(w)$ is material parameter, and the results predicted above statistical model. Taking in view that w is similar $L_{PZ} \sim L_H$, the root term is the inverse characteristic time t_C given by the self-similar solution. This fact allowed us to determine the range of the application of this generalized Griffith relation, where the crack can approach to the rest smoothly: $V < V_C$. For $V > V_C$, when the "wave part" of energy will increase with crack velocity, the crack arrest will appear non-smoothly for the energy metastability providing the "crack trapping". The similar view can be developed to analyze the crack overload above the Griffith value before any state motion.

7. RESONANCE EXCITATION OF FAILURE

7.1. Delayed Failure Phenomenon. Failure Waves

The phenomenon of failure wave in brittle materials is the subject of intensive study during last two decades. The term "failure wave" was introduced in [37] as the limit case of damage evolution when the number of microshears will be large enough for the determination of front with characteristic group velocity. This front separates the structured material from the failed area. The important feature of failure wave phenomenon is that the velocity of failure wave doesn't depend on the velocity of propagation of the single crack having the theoretical limit equals to the Rayleigh wave velocity. The stored elastic energy in material is the main factor, which provides the ability of brittle solid to the generation of failure wave. The high capacity of elastic energy in material can be created under the bulk compression or in the condition of loading providing the state close to the bulk compression, for instance, under impact loading. The necessity to provide the high capacity of elastic energy can be realized by the removal of surface defects or the structure homogenization. The brittle materials (glasses and ceramics) exhibit very high dynamic compressive strength, the Hugoniot elastic limits [38]. For the glasses with high strength or the high latent compressive stress self-keeping failure can be observed not only for the compression but also for bending and tension.

Rasorenov *et al* [39] were the first to observe the phenomenon of delayed failure behind the elastic wave in glass. Such a wave was introduced in [40] were the concept of a wave of fracture was discussed to

explain the nature of elastic limit. The existence of failure wave was established by considering a small recompression signal in the VISAR record of the free surface velocity of K19 glass (similar to soda-lime). This recompression signal resulted from a release returning after reflection of the shock at the glass rear surface reflecting again in compression at the lower impedance failure front. Recent studies have suggested that a wave of failure propagates behind the elastic wave in glass with a velocity in the range 1.5-2.5 km/s. Failure wave appeared in shocked brittle materials (glasses, ceramics) as a particular failure mode in which they lose strength behind a propagating front. Generally, the interest to the failure wave phenomenon is initiated by the still open problem of physical interpretation of traditionally used material characteristics as the Hugoniot elastic limits, dynamic strength, the relaxation mechanism of the elastic precursor.

The recent research has shown that glasses having open structures may fail in a characteristic way when loaded with plane shock waves. More filled materials such a soda lime glass have an elastic response to 6 or 7 GPa and plastic behavior beyond. The experiments in [41] confirmed the existence of these waves and extended measurements to glass states behind the shock (but ahead of the failure front) and behind the failure wave using manganin stress gauges. The tensile (spall) strength of the glass remained high behind the shock but dropped to zero behind the failure front. Additionally, the shear strength of the material was dropped from a high value ahead becoming lower behind the failure front. The experimental study established the sharp light opacity behind front under high speed videocamera recording [42], reduction in acoustic impedance, lowered sound speed [39]. The material states behind and ahead of moving boundary (behind the shock) allowed the measurement of failure wave speed [43]. The comparison of these data with high speed framing in soda-lime and borosilicate (Pyrex) glasses [38,44] revealed the constant value of the failure wave speed.

Qualitative changes in silicate glasses behind the failure wave under the measure of the refractive index (refractive index increased) allowed Gibbons and Ahrens [45] to qualify this effect as the structural phase transformation. These results stimulated Clifton [46] to propose the phenomenological model in which the failure front was assumed to be a propagating phase boundary. According to this model the mechanism of failure wave nucleation and propagation results from local densification followed by shear failure around inhomogeneities triggered by the shock.

The description of failure wave phenomenon as the consequence of the generation of collective burst modes of mesodefects was proposed in [47,48,49] in the course of study of non-equilibrium transition in defect ensemble. It was shown the existence of the self-similar solution for the microshear density tensor, which describes the qualitative changes in the microshear density kinetics in the course of the non-equilibrium transition. The failure waves represent the specific dissipative structures (the "blow-up" dissipative structures) in the microshear ensemble that could be excited due to the pass of the elastic wave.

Self-Similar Solution

Equation (5.3) describes the characteristic stages of damage evolution. In the range of stress $\sigma < \sigma_c$ and the defect density $p < p_c$ the damage kinetics is subject to the "thermodynamic branch" oa corresponding to the local minimum of the free energy (Fig.2.1; 2.2). At the approaching of stress to the critical value σ_c ($p \to p_c$) the properties of the kinetic equation (5.3) change qualitatively (from elliptic to parabolic) and the damage kinetics is subject to specific spatial-temporal structures which appear in the defect ensemble in the course of the interaction between defects [12]. These structures describe the damage localization and the nucleation of failure hotspots.

The spatial-temporal structures are given by the self-similar solution (5.8) of the kinetic equation (5.3) under the pass of the critical point p_c. The substitution of (5.8) into (5.2) leads to the equation for $f(\xi)$

$$-\frac{1}{\beta-1}f-\frac{\beta-(\omega+1)}{2(\beta-1)}\xi\frac{df}{d\xi}=\frac{d}{d\xi}\left[f^\omega\frac{df}{d\xi}\right]+f^\beta . \tag{7.1}$$

The conditions for f at the front ξ_f of the dissipative structure and the symmetry conditions at the center of structure are

$$\xi=\xi_f: f=0, f^\omega\frac{df}{d\xi}=0 , \tag{7.2}$$

$$\xi=0: f^\omega\frac{df}{d\xi}=0 . \tag{7.3}$$

We assume that the defect density in the dissipative structure exceeds essentially this density outside the failure hotspot. The difference in the number of conditions (7.2) and (7.3) and the differential power of Eqn. 7.1 means that the solution exists only for specific values of $\xi_f = \overline{\xi}_f$, i.e. the eigen-value problem for ξ_f arises. The method for the solution of this problem was developed in [13] that allowed the estimation of $\overline{\xi}_f$ and the definition of failure front propagation.

$$x_f = \overline{\xi}_f \chi_0^{1/2} \, S^{-\frac{\omega}{2(\beta-1)}} \, t^{\frac{\beta-\omega+1}{2(\beta-1)}} \, . \tag{7.4}$$

Eqn. 7.4 determines three of self-similar regimes depending on the relations between the parameters of the non-linear medium. If the material properties and the stress level provide the damage localization kinetics with parameters $\beta > \omega + 1$ the failure wave front will propagate with a group velocity given by the solution (7.4).

Some Experimental Results

The blow-up kinetics of damage localization allowed us to link the hotspots of failure with the above mentioned self-similar structures. The correspondence of these hotspots having the image of mirror zones to above self-similar structures was confirmed experimentally in [50,51]. The multiple mirror zones with an equal size were excited on different spall cross sections in the shocked PMMA cylindrical rod when the stress wave amplitude exceeded some critical value corresponding to the transition to the so-called "dynamic branch" under spalling (Fig. 7.1). The constant size of damage localization corresponds to the damage kinetics (free energy release rate) given by the following relationship between non-linearity parameters $\beta \approx \omega + 1$.

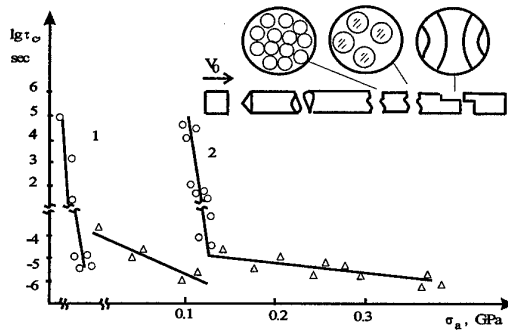Figure 7.1. Fracture time t_f for shocked rod of PMMA (1) and ultraporcelain (2) versus stress amplitude σ_a. Inset: surface pattern with mirror zones in different spall cross sections.

The "dynamic branch" corresponds to the stress $\sigma > \sigma_c$, where the failure scenario is determined by the generation of the collective mode in defect ensemble in the form of the dissipative structure with blow-up damage kinetics. The self-keeping features of failure corresponding to the condition of failure wave where observed also in the condition of dynamic crack propagation. The framing of crack dynamics in the preloaded PMMA plane specimen established the existence of the transient velocity $V_B \approx 600 \, m/s$, when the branches behave autonomous, Fig. 6.4. The low rise of velocity for $\sigma > 60 \, MPa$ reflects the stress independent character of failure similar to the dynamic branch in spall fracture. The pictures of stress distribution at the crack tip is shown in Fig.6 for slow ($V < V_C$), fast ($V > V_C$) and branching ($V > V_B$) cracks.

7.4. Simulation of Failure Waves

The study of failure wave initiation and propagation was carried out on the basis of constitutive equation (4) coupled with momentum transfer equation. The defect density tensor in the compression stress wave represents the microshear density.
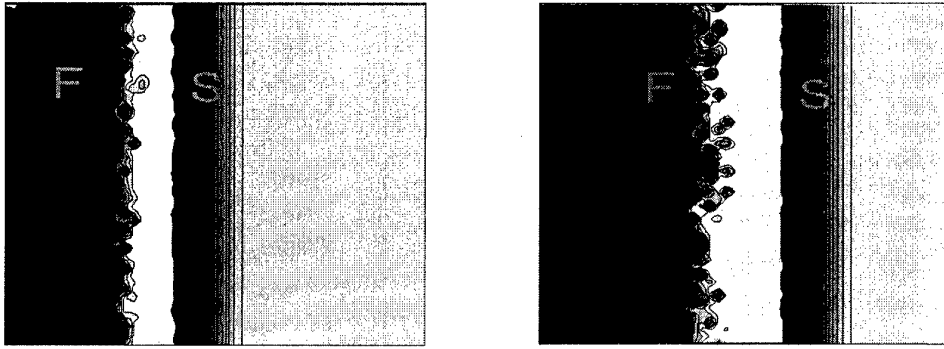
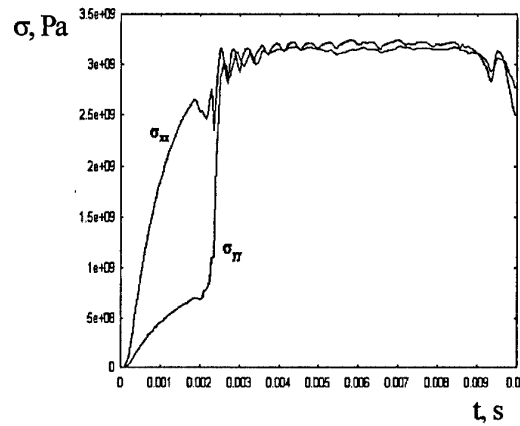*Figure 7.2. Propagation of stress (S) and failure (F) waves.*

Figure 7.3. Longitudinal σ_{xx} and transverse σ_{yy} stress kinetics.

The system of equations was solved using original finite element code. The simulation confirmed the delayed propagation of the failure front behind the stress wave, Fig.7.2. We observed also that the shear stress vanishes in the failure wave. The failure wave propagation leads to qualitative change in the transverse stress when this stress is approaching to the longitudinal stress level, Fig.7.3.

Statistics of Fragmentation

Qualitative new features in the crack dynamics (transition from the steady state branching regimes and the fragmentation), the phenomenon of the delayed failure revealed specific features of dynamic failure that is the property of non-equilibrium system with nonlinear and stochastic behavior caused by the collective effects in defect ensemble. This allows us to develop the view on the dynamic fracture statistics (fragmentation problem) to link the nonlinear dynamic aspects of damage evolution with the change of symmetry properties in the system due to the generation of collective modes in the defect ensemble.

Some basic theories have emerged within the past 10 years for predicting the consequences of dynamic fragmentation induced by high velocity impact or explosive events. These theories have focused on the prediction of mean fragment size through energy and momentum balance principles [52-55], and on statistical issues of fragment size distribution [56,57]. However, there are a number of unresolved issues within the development of statistical energy balance theories of fragmentation.

The dynamic fragmentation was analyzed in [58] on the approach based on local energy inequality and minimum fracture time requirement. This theory was later modified in [54] to include the kinetic energy available for fragmentation. However, the theories are not complete because the evolution process that leads to the catastrophic failure of the materials was not considered.

Taking in view the dramatic changes in the scaling properties of nonlinear system "solid with defects" due to the re-subjection of the system behavior to the collective modes of defects, the following scenario of the dynamic fragmentation can be discussed. The existence of characteristic stages of dynamic fracture under crack propagation (Fig.6.4) allowed us to establish the correlation of the dynamic fragmentation statistics with the energy density imparted to the material. The energy density $E < E_C$ (E_C corresponds to the critical velocity

20

V_C of the steady state – branching transition) provides the stress intensity controlled failure scenario. The transient densities $E_B > E > E_C$ ($V_C < V < V_B$) lead to the fracture statistics that is sensitive to both self-similar solutions: the self-similar stress distribution at the crack tip and collective blow-up modes of damage localization. The intermittency effect, when the system reveals the complex statistics in the presence of two attractors, probably, has the phenomenological interpretation in the framework of the Weibull statistics. Taking in view theoretically predicted low limit of damage localization scale L_C, it can be assumed the existence of critical energy density, which provides the limit size of fragmented structure close to L_C. Taking in view that these energy densities can be imparted in material generally by shock, this homogeneous fragmentation can be realized due to the failure wave excitation. The experiments in [59] with large specimens (optical glass K5 impacted by blunt steel cylinder) visualized the several fracture nucleation in the form of failure waves. Several spherical or nearby spherical waves were formed ahead of the main front.

8. PLASTICITY AS METASTABLE ORIENTATION TRANSITION IN MICROSHEAR ENSEMBLE

8.1. Defect Induced Mechanisms of Momentum Transfer

The physical particularity of the momentum transfer under the plastic flow is the motion of the deformation carriers (microshears in our case) in the conservative (elastic) field. This fact reflects the principal difference of irreversible deformation caused by the dislocation structure rearrangement from conventionally known mechanism of the viscous flow in liquids, which occurs due to the momentum diffusion.

Much progress was attempt during last decades in the understanding of mechanisms of the plastic flow and the development of the phenomenology of plasticity for the large range of the stress and strain rate intensities. However, the attempt to use the structural aspects in the formulation of the plasticity constitutive equations did not allow the explanation of most principal questions related to the specific nature of deformation carriers responsible for the plastic flow. Still unresolved problems are the regularities of the strain localization due to the shear banding, the linkage of the structure evolution with deformation hardening, the explanation of the structure of the plastic wave front in shocked materials.

The experimental data concerning the transitions in dislocation substructures under the plastic flow and the results of the statistical description of collective behavior of microshear ensemble allowed the consideration of plasticity rules in the linkage with the structure evolution. It was discussed in Section 2 that the intermediate range of the structural heterogeneity (for instance, grain size) corresponds to the values of the structure sensitive parameter $\delta_c < \delta < \delta_*$ and provides the deformation response of solid caused by the generation of collective modes of the microshear ensemble with pronounced orientation. The formation of these modes is the consequence of the orientation instability in the microshear ensemble in the corresponding range of external stresses $\sigma_y^a < \sigma_y < \sigma_{HEL}$ for the given structural parameter δ (Fig. 8.1). These stresses determine the range of the yield stresses (σ_y^a, σ_{HEL}), where the orientation metastability occurs. The yield stresses from this range represent the sum of the stress σ_y^a (where orientation metastability can appear). This stress has the athermal nature and determines the initial point of availability of the coherent microshear behavior as qualitative new mechanism of stress relaxation. The part of yield stress ($\sigma_y^m - \sigma_y^a$) determines the additional stress, which provides the thermally activated transition $A \to D$ in the dislocation substructure in more orientated state D.
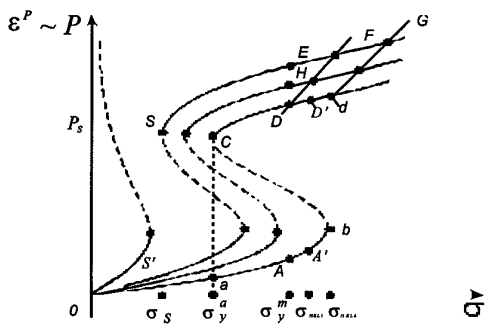

Figure 8.1. Metastable orientation transition in microshear ensemble
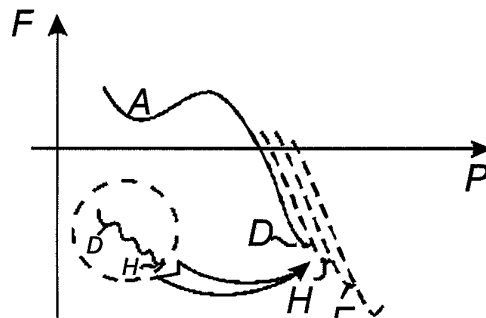
Figure 8.2. Free energy "transitions"

The jump in the microshear density parameter Δp_{AD} leads (according to Eqn. 5.4) to the sharp drop of elastic modulus, which precedes to the plastic flow. The possible scenario of the microshear ensemble evolution at the point D is shown in Fig. 8.1 and can involve two opportunities. The first one, along $BD'd$ trajectory, supposes high deformation hardening. The second scenario (along the trajectories DHE or DHF) assumes the increase of deformation caused by the defects in the continuous orientation ordering in the course of metastable transitions due to the change of value of structure sensitive parameter δ. Two realizations of this scenario (DHE and DHF) correspond to the typical plastic deformation of solid that are conventionally known as the perfect plasticity (DHE) and the plasticity with a hardening (DHF).

This type of the plastic flow is described in the framework of the incremental plasticity theory, when the increment of plastic deformation $d\varepsilon_{ik}^p$ $(= dp_{ik})$ is determined by the so-called normality rule

$$d\varepsilon_{ik}^p = d\lambda \frac{\partial \Phi}{\partial \sigma_{ik}},$$ (8.1)

where Φ is the plastic potential, λ is the multiplier. The incremental law of plastic flow determines the plastic strain decrement as the result of the "expansion" of the yield surface, given by the plastic potential Φ.

The consideration of the plastic flow as non-equilibrium orientation transition allowed the interpretation of the phenomenological background of the incremental plasticity. According to this result the driving force of the plastic deformation is the minimization of the free energy $F(\sigma, p, \delta)$ in the current system state, for instance $(\sigma_D, p_D, \delta_D)$, under the continuous ordering of defects ($D \rightarrow A \rightarrow ...$) and the formation of different dislocation substructures. The description of these transitions can be obtained as the generalization of the evolution inequality (5.2) considering δ as the independent variable

$$\delta F = \frac{\partial F}{\partial p} dp + \frac{\partial F}{\partial \delta} d\delta \leq 0 \quad \text{or} \quad \frac{\delta F}{\delta t} = \frac{\partial F}{\partial p} \frac{dp}{dt} + \frac{\partial F}{\partial \delta} \frac{d\delta}{dt} \leq 0.$$ (8.2)

Assuming the linear relations between the increments $(dp, d\delta)$ and thermodynamic forces $(\frac{\partial F}{\partial p}, \frac{\partial F}{\partial \delta})$, the equations for the transitions read

$$dp = -Y_p \frac{\partial F}{\partial p}, \quad d\delta = -Y_\delta \frac{\partial F}{\partial \delta}.$$ (8.3)

It is evident that the increment $d\delta$ plays the role of the increment $d\lambda$ and provides the change of the plastic flow potential in term of δ. For the quasi-static loading the relations (8.3) allowed the expression of the increment $d\delta$ in the term of current values of stress and defect induced plastic strain p. The unloading, for instance from point F occurs along the trajectory FES in the "partly unloaded state". The analog of σ_y^q under unloading is the threshold stress Σ_y^q of the metastability area LC under unloading. Taking in view that the plastic flow realizes as continuous orientation ordering of dislocation substructures with the scaling parameter δ related to the size of the dislocation substructure l_n and the distance between ones l_c, the real scenario of the plastic straining depends on the loading conditions, for instance, the stress or the strain rate.

The strain rate sensitivity of plastic flow is observed typically at strain rates exceeding $10^3 s^{-1}$. It is important to use in this range of strain rate $\dot{\varepsilon} > 10^3 s^{-1}$ the description of independent kinetics of defect induced plastic straining and the structure evolution in the form given by the second equation in (8.2).

$$\frac{dp}{dt} = -L_p \frac{\partial F}{\partial p},$$ (8.4)

$$\frac{d\delta}{dt} = -L_\delta \frac{\partial F}{\partial \delta},$$ (8.5)

where L_p and L_δ are the kinetic coefficients. The relations between the kinetics of the external loading (for instance imposed stress or strain rate), the kinetics of transition in the p metastability area and the kinetics of

structure sensitive parameter δ determine the variety of the material behavior for high strain rate loading and the response of shocked materials.

The kinetics of δ-parameter determines the hardening law due to the formation of new dislocation substructures responsible for the momentum transfer in more high structural level that is realized as the rescaling of initial structural scales $l_n \rightarrow L_n(p), l_c \rightarrow L_c(p)$. Experimental data concerning the variation of the flow stress with a strain rate established the dramatic increase of the flow stress at the strain rate $\dot{\varepsilon} > 10^3 \text{-} 10^4$ s^{-1}. The description of the plastic flow as metastable orientation transition in the defect ensemble allowed us to propose the explanation of the anomalous hardening. Eqn. 8.5 can be represented in the form

$$\frac{d\delta}{dt} = -\frac{1}{\tau_\delta}\frac{\partial \widetilde{F}}{\partial \delta},$$
(8.6)

where $\widetilde{F} = F/A$, $\tau_\delta = (L_\delta A)^{-1}$ is the characteristic time of structure rearrangement in the term of δ. The anomalous hardening for the strain rate $\dot{\varepsilon} > 10^3 - 10^4 s^{-1}$ is the consequence of limiting rate ability of materials to the dislocation substructure rearrangement with characteristic time $\tau_\delta \approx 10^{-5}$ s^{-1}. For the strain rates exceeding $\dot{\varepsilon} > 10^4$ s^{-1} the plasticity, as metastable transition to the dislocation substructure with more pronounced defect orientation on large spatial scales, could not be realized and defect ensemble evolution could occur along the branch $CDD'd$ with a constant value of δ and the maximal hardening.

9. KINETICS OF METASTABLE TRANSITIONS AND MECHANICAL RESPONSES OF SHOCKED CONDENSED MATTER

9.1. Structure of Stress Wave in Solid under Impact Loading

Complicate material responses to the increase of the strain rate are observed in the nonlinear behavior of deformation and in the changes of yield stresses of plasticity and strength. The attempts were undertaken in [47,50,51] to establish the linkages of the mesodefect evolution (microcracks, microshears) with relaxation properties and failure kinetics. Statistical approach allowed us to establish specific features of the defect ensemble evolution caused by the initial solid state (structural heterogeneity in the term of δ) and the interaction between defects. Scenario of defect ensemble evolution has the form of non-equilibrium kinetic transitions, which appear as a specific form of the self-similarity. This self-similarity is displayed particularly clear at plastic instability and damage localization under dynamic loading. The self-similarity in the behavior of solid loaded dynamically is caused by the excitation of spatial-time structures in the defect ensemble. The appearance of these structures is accompanied by the qualitative change of solid responses to dynamic loading.

The established correspondence of the nonlinear behavior of the defect ensemble and the structure of the shock wave profile allows the explanation of some regularity of shocked material responses.

One dimension plane shock waves have been widely used to study the mechanical response of solids to high velocity deformation. For many materials under a certain range of impact pressures, there exists a two-wave structures of which the first wave, the so-called, elastic precursor, travels at the velocity of sound waves, while the second wave, plastic shock wave, travels at a slower speed which increases with impact pressure. While the full two-wave structure is thus not steady (does not propagate without change of form), each component wave may be treated as steady after sufficient propagation distance.

The stress wave structure was examined in [60] for the impact loading of aluminum plate loaded by the quartz disk at the rate of $400 m/s$. In the case of the plane wave propagation in z direction the system of constitutive equations coupled with conservation laws of mass and impulse are written as

$$\frac{\partial p'_{zz}}{\partial t} = -L'_p \frac{\partial F'}{\partial p'_{zz}}, \quad \frac{\partial p_0}{\partial t} = -L^0_p \frac{\partial F_0}{\partial p_0}$$
(9.1)

$$\dot{\varepsilon}_{zz} = \dot{\varepsilon}^e_{zz} + \dot{p}_{zz} \ , \quad \dot{\varepsilon}^e_{zz} = \dot{\sigma}_{zz}/E \ ,$$
(9.2)

$$\rho \frac{\partial^2 u_z}{\partial t_2} = \frac{\partial \sigma_{zz}}{\partial z} \ ,$$
(9.3)

$$\varepsilon_{zz} = \frac{\partial u_z}{\partial z} \ ,$$
(9.4)

where $p_{\dot{t}z}$ and p_0 are devitoric and isotropc parts of p_{zz}, $F=F'(p'_{zz},\sigma'_{zz})+F$ (p_0,σ_0),

ρ is material density, L_p and L^0_p are the kinetic coefficients. There is only $p_{\dot{t}z}$ component in the compression waves.

The solution of system (9.1)-(9.4) has to satisfy the boundary and initial conditions:

$$\sigma_{zz}(0,t) = \sigma_0(t), \sigma_{zz}(h,t) = 0 ; v_z(z,0) = \sigma(z,0) = p_{zz}(z,0) = 0 ; \rho(z,0) = \rho_0,$$

where h is the plate thickness, $\sigma_0(t)$-function was determined on the basis of the solution of collision problem.

Material parameters have been determined from quasi-static data of aluminum testing (uni-axial tension) using direct methods of the registration of the microcrack accumulation. The parameters were taken

$$\rho = 2.71\cdot10_3 kg/m_3, \quad G = 109.7GPa, \quad \tau_p = L_p/G = 2.1\cdot10_{-6}\,sec, \quad \tau_l = h/C_l = 1.96\cdot10^{-6}\,sec \quad (C_l=(G/\rho)^{1/2}).$$

Presented in Fig. 9.1 are the results of numerical simulation of the stress wave propagation and the time-dependencies of stress and microcrack density parameter in the spall section. In the stress area corresponding approximately to the dynamic yield stress the orientation kinetic transition for the parameter p_{zz} is realized which results in the abrupt increase in stress relaxation tempo, a change in the plastic wave profile and the separation of the elastic precursor (bolt parts of the curves in Fig. 9.1).

A sharp transition to the highly ordered structure due to the metastable transition may lead to the behavior which has been commonly referred as dynamic failure due to the plastic shear instability. Spatial scales of the orientation area (shear localization zone) are determined by the parameters of the solitary wave of shear instability given by the solution (5.6).
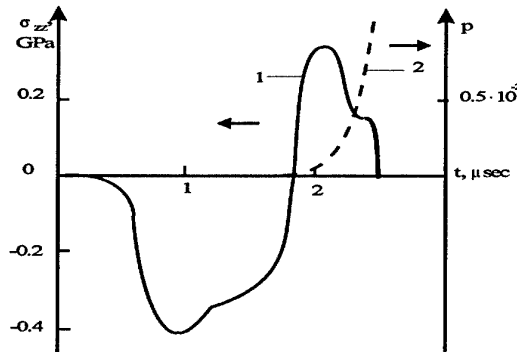
Figure 9.1. Structure of stress waves and damage kinetics in spall cross-section of aluminum target.

9.2. Strain Rate Universality at the Steady-State Plastic Wave

Experimental evidence of viscous like effects in solids was lacking until the results of Sakharov's group [61] when the measure of shock viscosity in solids was inferred using the indirect method. The existence of steady-wave shocks as significant feature of stress wave in solids is treated in [62,63]. With the development of laser interferrometry techniques the first direct measurements of high-resolution wave profiles were provided in [64] for aluminum. The observation of the shock wave rise showed the very rapid increase in steady-wave strain rate with increasing peak stress. This increase is substantially greater than would be predicted by a simple Newtonian proportionality between viscous stress and strain rate. The existence of steady-wave solutions for the Navier-Stokes equations has been recognized first by Rayleigh and Taylor [65,66]. Since then a large literature on this subject in the field of fluids has emerged [67,68].

The unique feature of large amplitude wave profile is the steady-wave plastic-shock profile. The steady-wave profile propagates without change in form and, as it pointed out in [69] is a consequence of a stable balance between the competing processes of stress-strain non-linearity and dissipative or viscous material behavior.

According to the results presented in Section 5 the steady-wave profile for different shock amplitudes appears as the self-similar auto-solitary waves induced by the collective orientation mode in the microshear

ensemble. The rescaling of current values of δ (*DHF* -path, Fig. 8.1) provides the self-similar auto-solitary response for the variation of the stress-amplitude.

The rate of the transition $\dot{p}_{zz}$ from the lower to upper branches reaches the maximum under the deepest penetration into the metastability area (point b in Fig.8.1). This is assumed to be a main reason of the universality of the plastic strain rate dependence on the stress amplitude $\dot{p}_{zz} \approx A\sigma_{amp}^4$ established by Barker and Grady for wide class of materials for strain rates $\dot{\varepsilon} > 10^5$ s⁻¹. This relation follows from the self-similar solution (5.6), when the driving force of the transition under the δ - rescaling can be represented in the term of stress as the difference in the free energy for the current level along the dG -path (Fig. 8.1) and the energy for metastability limits (the analog of point b, Fig. 8.1) for the curves corresponding to the current values of δ.

This result reflects the importance of the collective effects (orientation transition) in the system of defects providing the intriguing material independent feature in the steady shock process and reveals the specific character of the solid viscous response. On another side the universality of this fourth power dependence for a large class of the materials allows the assumption that in the intensive shock environment the complex structural processes that are involved due to the plastic flow become simpler. The study of these general mechanisms seems to be important for the understanding of the collective effects in the defect ensembles responsible for the irreversible deformation in solids.

Relaxation Properties and Defect Induced Instabilities in Shocked Liquid

The problem of the true structure of liquids can not at present be considered as finally explained. A dependence of mechanical properties on the relation between the relaxation time of the medium and the characteristic time of the loading is not only the property of solid but is also valid for a liquids. Any theories of viscous liquid flow starts out to some extent an assumption about the nature of structure of liquid. For this reason investigation of the relaxation properties of liquid under high strain rate loading produced by shock waves, are of great scientific and applied interest. The viscosity of condensed matter plays the principle role in effecting the irreversible shock compression. It is well known that without account of the viscosity one can not produce a continuous distribution of all thermodynamic quantities in the shock wave front (SWF).

The method of investigating viscosity of materials behind the SWF, proposed first by Sakharov [61], is based on the experimental study of small perturbations on the SWF and then by Barker [64] with the usage of the Doppler interferometry (VISAR) technique.

The still unresolved puzzle was established in the Sakharov experiments when the shocked liquid (water and mercury) and solid (aluminum and lead) reveled the same viscosity $\eta = 10^4$ *Pz* at approximately the same values of the strain rate $\dot{\varepsilon} = 10^5$ *s*⁻¹ at the SWF. It is necessary to underline that these substances so different under normal conditions. Nevertheless, for the pressure $P \approx 80 - 100$ *KBar* water and mercury are characterized by the same dynamic viscosity as that unmelted solid (pressure range $P \approx 400 - 500$ *KBar*) behind SWF. It allowed the conclusion that the mentioned liquids in the pressure range $P \approx 80 - 100$ *KBar* have a relaxation time $\tau > \dot{\varepsilon}^{-1} \sim 10^{-5}$ *s* differing by 6 orders from the molecular (diffusion) relaxation times estimated by the Einstein formula as $\tau_D = \Delta^2/6D_{sd} \sim 10^{-11}$ *s*, where Δ is the distance between the particles, D_{sd} is the self-diffusion coefficient. It means that a liquid behaves in the indicated experiments effectively like a solid.

The physical mechanisms leading to the development of instabilities in condensed media indicate the possibility of describing instabilities in liquids on the basis of an analysis of the kinetics of fluctuations, if the latter are viewed as defects in the structure of the liquids [12,70]. In the case of liquids the mesoscopic defects, being by their nature the fluctuation of the displacement field in solids, can be also regarded as real structural defects which are produced during collective motion of groups of molecules. This mechanism of motion does not correspond to the conventional diffusion mechanism of momentum transfer in simple liquids.

The attempt to explain the noncontradictory nature of the viscosity of shock compressed liquid and solid for the strain rate $\dot{\varepsilon} = 10^5$ *s*⁻¹ was undertaken by in [61] to use the Fraenkel idea concerning the role of defects ("holes") produced by the propagating SWF. The validity of this view was qualitatively confirmed by the measure of the electric conductivity of water behind the SWF, when the dramatic change of the receptivity was found.

Apparently, Fraenkel [71] was the first to call attention to the analogy in the mechanisms of flow of solids and liquids, noting that "... x-ray diffraction pictures of liquids are similar to those of microcrystalline solids, and it would be possible to interpret their general features on the basis of the idea that a liquid consists of a large number of randomly oriented submicroscopic-size crystals" and " the widely held view that the fluidity of liquids is caused by the absence of shear elasticity, i.e., by a zero shear modulus, ... is incorrect (except, possibly, for the case of liquid helium II)." These statements are confirmed in [72] by measurements of

relaxation spectra in a shear simple liquid flow accompanying the superposition of shear oscillations in a liquid at frequencies $10^5 Hz$ when the existence of shear elasticity was established. The explanation of this long relaxation time anomaly is linked in [72] with a coordinated displacement and reorientation of groups of molecules which involves longer times. A coordinated displacement of groups of molecules (similarly to the relative slipping of blocks or grains in solids) can be realized during nucleation of mesoscopic defects arising between these groups of molecules.

The dissipative function for a medium relaxing by flow and as a result of the development of defects has the form [12]

$$TP_s = -\frac{1}{T} q_k \nabla_k T + \sigma_{ik} e_{ik}^v - \frac{\delta F}{\delta p_{ik}} \dot{p}_{ik} \geq 0, \qquad (9.5)$$

where T is the temperature, q_k is heat flux, $\delta F / \delta p_{ik}$ is the thermodynamic force acting on a system when p_{ik} is different from its equilibrium value, and $e_{ik}^v = e_{ik} - \dot{p}_{ik}$ is the "viscous" component of the strain rate tensor. The condition that the dissipative function be positive-definite leads to a system of equations for the tensor variables:

$$\sigma_{ik} = \eta e_{ik}^v + \chi \dot{p}_{ik}, \qquad (9.6)$$

$$-\frac{\delta F}{\delta p_{ik}} = -\chi e_{ik}^v + \varsigma \dot{p}_{ik}, \qquad (9.7)$$

where $\eta, \chi,$ and ς are kinetic coefficients. For the case of simple shear, from Eqn. 9.6 follows an expression for the effective viscosity

$$\eta_{im} = \frac{\sigma_{xz}}{e_{xz}} = \eta - (\eta - \chi) \frac{\dot{p}_{xz}}{\dot{\varepsilon}_{xz}}. \qquad (9.8)$$

In the interval $\delta_c < \delta < \delta_*$ the strain rate fluctuations "conform" to the spectrum of solitary waves, meaning that $\dot{\varepsilon}_{ik} \approx \dot{p}_{ik}$, and Eqn.9.8 gives the asymptotic viscosity $\eta = \chi$. The independence of viscosity of condensed matter $\eta \approx 10^4\ Pz$ for the strain rates $\dot{\varepsilon} \approx 10^4 - 10^6 s^{-1}$ is the consequence of the subjection of the deformation response to the strain rates induced by the defect kinetics in the form of finite amplitude solitary wave disturbances.

The following scenario of the development of instabilities in a liquid is possible in accordance with the characteristic features of the nonlinear behavior of ensembles of defects.
The weak periodic pulsations of the velocity induced by defect induced fluctuations of the strain rates appear in the region $\delta > \delta_*$. The flow intensification can lead to the transition through the bifurcation point δ_* (the region $\delta_c < \delta < \delta_*$) and the nucleation of the cascade of solitary waves as a result of orientation transition in an ensemble of microscopic shears. The inertial cascade of the solitary waves is generated under the re-scaling of δ due to the appearance of new spatial scales linked with the solitary wave front. The second inertial interval appears in the course of the transition for $\delta = \delta_c$, when dissipative structures with blow-up kinetics of the defect induced strain rate are excited.

It is interesting to compare the real picture of turbulent flow with the scenario given by the dynamics of p_{ik}. The dynamics of the development of turbulence has been investigated in [73] in an analysis of the evolution of a turbulent spot in a Poiseuille flow with Reynolds number R~840-1500. It is observed that the turbulent spot has the form of a triangular wing, and the turbulent motion arises inside a region on the boundary of which disturbances in the form of solitary waves arise. These waves, generated on the boundary of the spot, propagate into the laminar zone and transform into quasi-periodic damped pulsations of the velocity. The motion of solitary waves in the direction of the spot results in secondary instability and growth of the spot. This experimentally observed scenario agrees with the nonlinear dynamics of macroscopic defect-induced strain rate fluctuations. The laws established for the development of instabilities in condensed media suggest the possible existence of a bifurcation tree, leading to turbulence [74], that can be described on the basis of a kinetic approach [75].

26

10. EXPERIMENTAL STUDY OF PLASTIC DEFORMATION OF COPPER UNDER SHEAR CONDITIONS

The samples from cold-rolled Oxyden Free Electronic (OFE) copper (99,99% Cu) were studied in the condition of plastic shear. The sizes and geometry of the samples are represented in Fig 1.

$$D_1 = 10^{-2} \ m; \quad D_2 = 1.3 \cdot 10^{-2} \ m; \quad h = 10^{-2} \div 2 \cdot 10^{-2} m;$$

$$L = 3 \cdot 10^{-2} \ m; \quad c_1 = c_2; \quad a = b = 1.4 \cdot 10^{-2} \ m; \quad d = 10^{-2}.$$
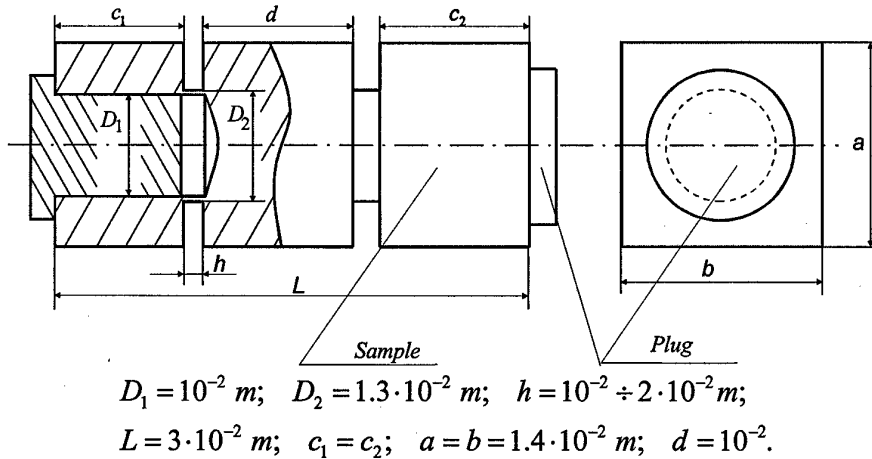
Figure 10.1. Geometry and size of the copper sample.

After mashinning, samples were given anneal heat treatments with the furnace cooling during 6 hour. Annealed temperatures was 350^0 C to, and annealed times was 60 minutes. To realize shear test the lever loading device was constructed, Fig. 2.
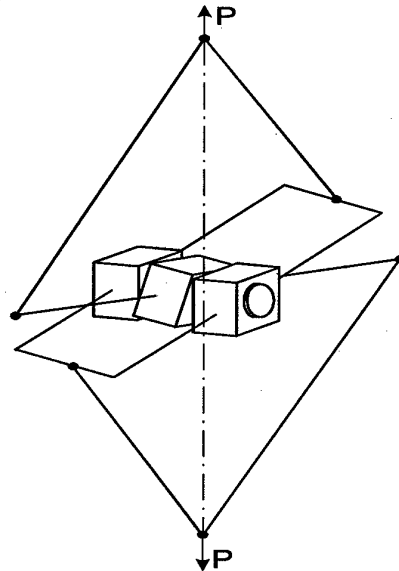
Figure 10.2. The scheme of the lever loading device.

The shear straining was realized along two ditch with width h =1 or 2 mm. Left and right parts of the sample are twisted to one side but the central part to another. The maximum twist angle was about 100-110^0 that corresponds to the deformation of about 600-1000% depends on h. Lever loading device was insert in the tensile testing machine 2167 P-50.

Experimental conditions:
maximum load is 5000 N;
strain rate is $\dot{\varepsilon} = 10^{-3} - 2 10^{-3} \ s^{-1}$.

room temperature.
The experimental equipment is presented in Fig. 10.3.

a)   b)
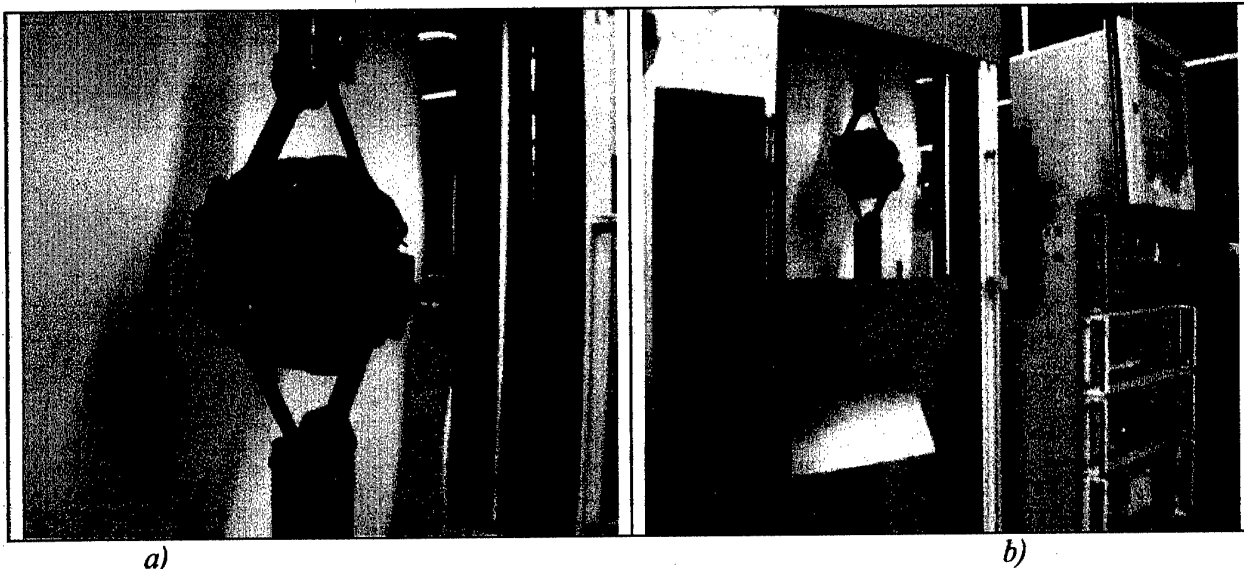
Figure 10.3. a) The lever loading device; b) The lever loading device inserted in the tensile testing machine 2167 P-50.

The load and displacement were registered during deformation process by tensile testing machine. "Load-displacement" diagram was recorded using double-coordinate self-recording system. Fig 10.4.

a)   b)

Figure 10.4. a) The samples before the deformation; b) The samples after the deformation.

The shear stress-shear strain curves $\tau - \gamma$ are presented in Fig.10.5 a,b.

$\tau, 10^7,$ Pa

a)

$\tau, 10^7,$ Pa

$\gamma, 10^2, \%$
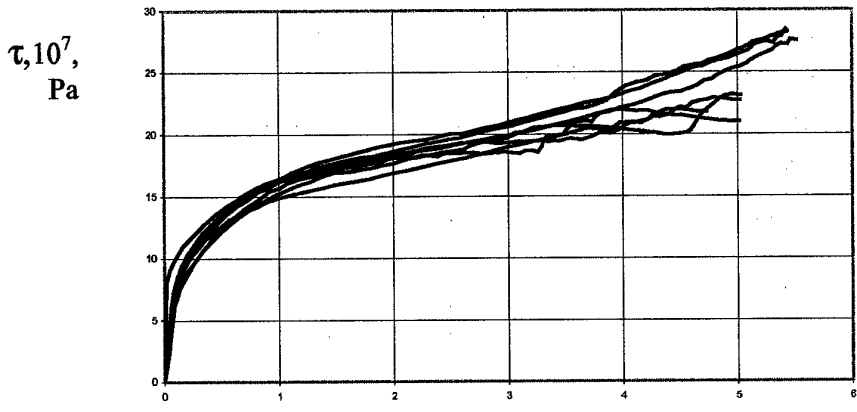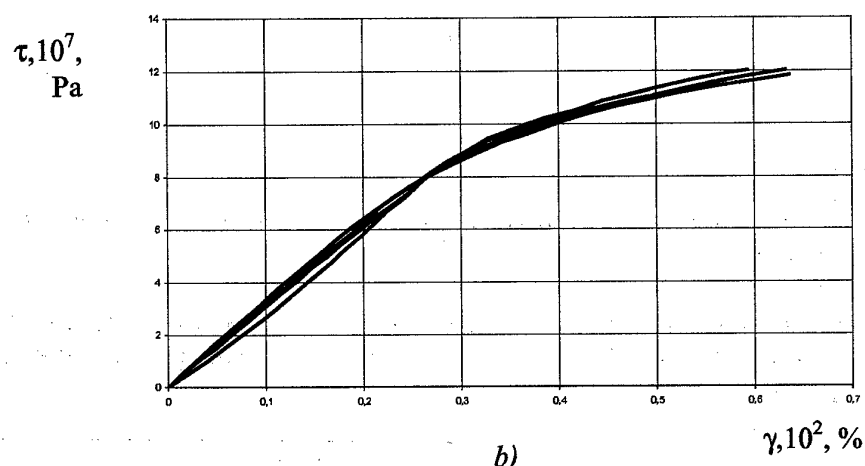
b)

Figure 10.5. The shear tress-shear strain curve a) $h = 2 \cdot 10^{-3} \, m; \dot{\varepsilon} = 10^{-3} \, s^{-1}$, *b)*

$h = 10^{-3} \, m; \dot{\varepsilon} = 10^{-3} \, s^{-1}$.

Fig. 6 illustrates the slip bands on the surface of the ditch after the shear deformation. The image was obtained using the microscope MBT 71Y4.2 and thedigital camera New View.

Figure 10.6. Slip bands on the surface of the ditch after the shear deformation (visible area 680x983 μm

29

11. EXPERIMENTAL STUDY OF COPPER UNDER DYNAMIC LOADING

11.1. Dynamically Loaded Copper Behavior

It is important to underline that data for the dynamically loaded copper obtained from different sources exhibit different dynamic stress-strain behavior or degrees of strain rate sensitivity. Data on copper have shown either no strain sensitivity at rates 10^3 s^{-1} [76] depending on the sours. This is attributed to either slight differences in material chemistry, microstructure or processing history. Data for annealed OFHC copper are presented in [77]. As for many of the other materials there appears to be a sudden increase in strain rate sensitivity at rates above 10^3 s^{-1}. The extrapolation of the uniaxial stress (quasi-static and Hopkinson bar data) shows that the HEL would correspond closest to data at the lowest constant strain value of 0.01. Degree of rate sensitivity is not constant over the range $10^{-3} - 10^3$ s^{-1}, but shows sudden upturns in the higher rate regime for some materials. Experimental data show a systematic increase of flow stress with strain rate over the strain rate range covered by the SHPB apparatus. At very low strain rates, below quasi-static a region of little or no strain rate sensitivity can be found. At higher rates in most metals, flow stress increases with strain rates in a linear manner with a logarithm of a strain rate.

At even higher rates, the degree of rate sensitivity increases dramatically when strain rates approach to the range of $10^3 - 10^4$ s^{-1}. One explanation for this behavior is based on the change in the rate-controlling deformation mechanism from thermally activated to linear viscous mode.

The behavior of copper, in particular, at very high strain rates is discussed in [76], where discrepancies in the rate sensitivity beyond a strain rate of 10^3 s^{-1} are highlight. However, the validity of some experimental results in this range of strain rate was questioned in [78]. It was not observed the apparent increase of the stress under uniaxial strain (plate impact) conditions at yield up to equivalent strain rates of 10^5 s^{-1}. In contradiction it was shown in [79] showed that OFHC copper revealed a highly rate-dependent properties. The rate-controlling mechanism in copper and sudden increase in rate dependence at rates exceeding 10^3 s^{-1} was linked with structure evolution plotting the data for constant strain. Using a "mechanical threshold stress" as a state variable which characterizes dislocation-dislocation interactions, they conclude that the increase in stress at high rates is due to the increased rate sensitivity at the strain hardening rather than to a true rate sensitivity at constant structure.

It was noted also in [76] that there is apparent change from a thermally activated mechanism to one causing a higher degree of rate sensitivity appears to accour for many materials at room temperature at strain rates which at upper limit of validity of the SHPB test technique.

11.2. The Hopkinson – Kolsky Technique

The Split Hopkinson pressure bar (SHPB) has become a very popular experimental technique for the study of the constitutive laws of materials at high strain rates ($10^2 - 10^4$ s^{-1}).

Kolsky`s original SHPB analysis is based on some basic assumptions: (i) The waves propagating in the bars can be described by one-dimensional wave propagation theory. (ii) The stress and strain fields in the specimen are uniform in its axial direction. (iii) The specimen inertia effect is negligible. (iv) The friction effect in the compression test is also negligible.

A typical SHPB set-up is outlined in Fig.11.1. It is composed of long incident and transmitted bars with a short specimen placed between them. The impact of the projectile (striker bar) at the free end of the incident bar develops a compressive longitudinal incident wave of strain ε_i. This elastic wave travels through the incident bar and then reaches the specimen, which is sandwiched between the incident and the transmitted bar. The amplitude of the wave is such that plastic deformation is imparted to the specimen. A part of the incident strain wave, ε_r, is reflected, whereas another part goes through the specimen and develops in the transmitted bar the transmitted strain wave ε_t. Those three basic waves recorded by the gages attached to both incident and transmitted bars. We measure the direct incident pulse, a reflected pulse, and a transmitted pulse, which have amplitudes $\varepsilon_i, \varepsilon_r$, and ε_t respectively. From these three pulses one can derive a stress-strain relationship for the specimen.

When the waves are known at bar-specimen interfaces, the stresses, the deformations and the deformation rates at both faces of the specimen are given by the following equation:

$$\sigma_s = E(A/A_s)\varepsilon_t,$$

$$\varepsilon_s = -2\,c_0/L \int_0^t \varepsilon_r dt,$$

$$\frac{d\varepsilon_s}{dt} = -\left(2c_0/L\right)\varepsilon_r.$$

where A – bar's cross-sectional area;
A_s – specimen's cross-sectional area;
E – Young's modulus;
C_0 – elastic wave speed.

The main assumption of the Kolsky method is satisfied during the entire test, namely:

$$\varepsilon_i = \varepsilon_r + \varepsilon_t,$$

where $\varepsilon_i, \varepsilon_r, \varepsilon_t$ - the incident strain wave, the reflected strain wave and the transmitted strain wave respectively. The Hopkinson bar is also used in tension, torsion, and shear.

11.3. Experimental set-up

The main components of the experimental set-up are loading devices with control system, and registering devices with PC for data processing. Pulsed loads in a SHPB are generated using 46-mm gas gun. The projectile is accelerated by compressed air. The gas gun makes it possible, in laboratory conditions, to accelerate projectile 200 mm long up to the impact velocities of 10-30 ms^{-1}.

Pressure test is conducted following the block-scheme (Fig.11.1). The both bars are 720-mm long and 30-mm diameter. The bars are made of steel. The specimens have the tablets shape.

The striker velocity is measured during it pass the fixed distance, where induction gauges are cemented. Two impulses are produced one by one and registered by the Counter.

The start of the registration system is produced by synchronization impulse, which are made by Pulse Generator. The impulsive generation of the Bridge Connection is produced by impulse of Pulse generator ($\tau = 1...2$ ms). The deformations in both pressure bars are measured with tensoresistors are connected by semi-bridge scheme (Fig.11.2).

The experimental information from the gauges cemented to the pressure bars equidistantly from the specimen is registered by the two-channel ADS. The processing program makes it possible to synchronize the registered impulses and to generate the dynamic deformation diagrams for tests.
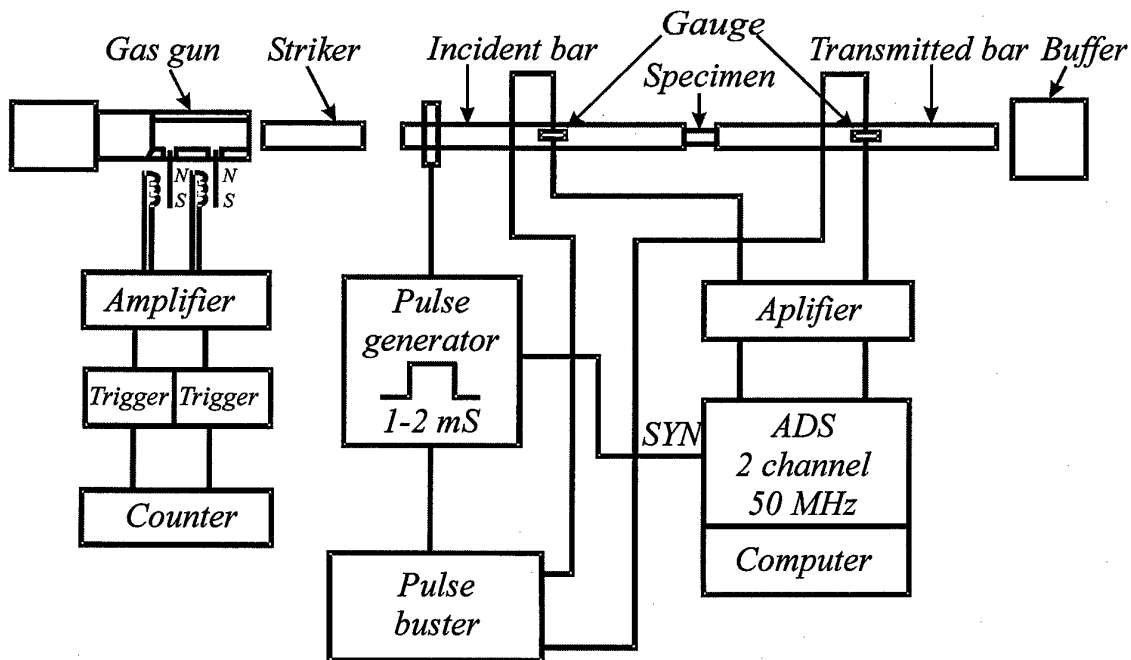
Figure 11.1 Split Hopkinson pressure bar
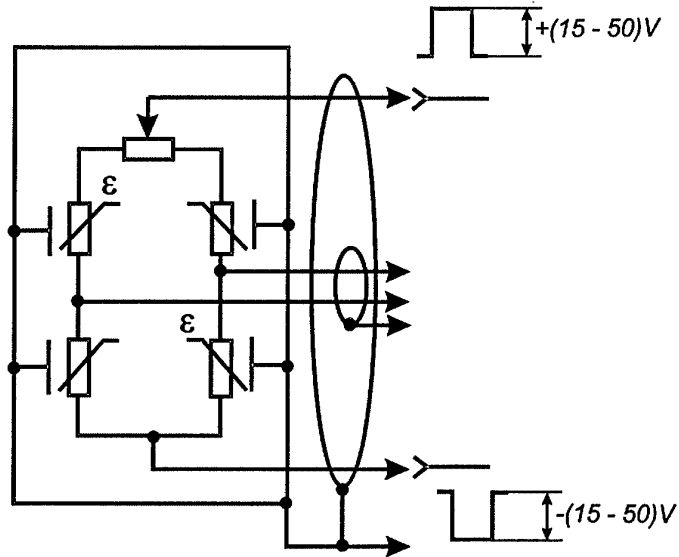
Figure 11.2.   Bridge Connection

11.4. Dynamic strain-stress diagrams for copper

Preparation of specimens.

Specimens made from copper of size 14 mm in diameter and 6mm in width were used to perform the experiment. In the preliminary stage the specimens were subjected to vacuum annealing at the temperature 500^0C. Then they were hold up for two hours. Finally they were cooled together with the oven. The annealed undeformed section specimen is shown in Figure 12.3. The average size of the grain is 0.6 mm.

Figure 11.3

SHPB experiment.

The split was modified to provide the single loading of the specimens in each experiment. The ends of the specimens were preliminary processed to achieve the purity Rz5. Just before placing the specimens between the bars, their ends were covered with a thin soap layer. This allowed us to avoid the buckling of the specimen during deformation. Each experiment was carried out on a series of five specimens, subjected to loading according to the following scheme: the first specimen – one impulsive force, the second specimen – two impulsive forces,…, and the fifth specimen – five impulsive forces. The velocity of the projectile was planned to keep the same during all the tests, but it did not always work. The experiments were carried out at the following velocities of the projectile: 4.6-5,5 m/s, 7-9 m/s, 15m/s.

experimental results

$\sigma \cdot 10^8 Pa$

Figure 11.4. Diagram $\sigma - \varepsilon$ for coppe (the specimen a18), impacts 1, 2, 3.
1 -- velocity of the projectile = 3.94 m/s, strain rate $d\varepsilon/dt=1124\ c^{-1}$;
2-- velocity of the projectile 6.41 m/s, strain rate $d\varepsilon/dt=1082\ c^{-1}$
3 -- velocity of the projectile 6.25 m/s, strain rate $d\varepsilon/dt=864\ c^{-1}$

$\sigma \cdot 10^8 Pa$

Figure 11.5. Diagram $\sigma - \varepsilon$ for copper (the specimen a18), impacts 1, 2, 3,4.
1 -- velocity of the projectile = 5.82 m/s, strain rate $d\varepsilon/dt=1124\ c^{-1}$;
2-- velocity of the projectile 6.41 m/s, strain rate $d\varepsilon/dt=1082\ c^{-1}$
3 -- velocity of the projectile 6.25 m/s, strain rate $d\varepsilon/dt=864\ c^{-1}$
4 -- velocity of the projectile 6.37 m/s, strain rate $d\varepsilon/dt=838\ c^{-1}$

$\sigma \cdot 10^8 Pa$

Figure 11.6. Diagram $\sigma - \varepsilon$ for copper (the specimen a18), impacts 1, 2, 3.
1 -- velocity of the projectile = 5.82 m/s, strain rate $d\varepsilon/dt=1124$ c^{-1};
2-- velocity of the projectile 6.41 m/s, strain rate $d\varepsilon/dt=1082$ c^{-1}
3 -- velocity of the projectile 6.25 m/s, strain rate $d\varepsilon/dt=864$ c^{-1}
4 -- velocity of the projectile 6.37 m/s, strain rate $d\varepsilon/dt=838$ c^{-1}
5 -- velocity of the projectile 7.01 m/s, strain rate $d\varepsilon/dt=1080$ c^{-1}

$\sigma \cdot 10^8 Pa$

Figure 11.7. Diagram $\sigma - \varepsilon$ for copper (the specimen a26), impacts 1, 2, 3.
1 -- velocity of the projectile = 3.94 m/s, strain rate $d\varepsilon/dt=759$ c^{-1};
2-- velocity of the projectile 5.03 m/s, strain rate $d\varepsilon/dt=935$ c^{-1}
3 -- velocity of the projectile 4.68 m/s, strain rate $d\varepsilon/dt=656$ c^{-1}

$\sigma \cdot 10^8 Pa$
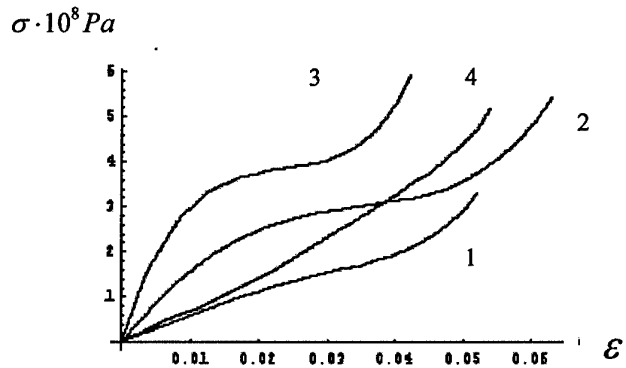
Figure 11.8 Diagram $\sigma - \varepsilon$ for copper (the specimen a26), impacts 1, 2, 3,4.
1 -- velocity of the projectile = 3.94 m/s, strain rate $d\varepsilon/dt=759$ c^{-1};
2-- velocity of the projectile 5.03 m/s, strain rate $d\varepsilon/dt=935$ c^{-1}
3 -- velocity of the projectile 4.68 m/s, strain rate $d\varepsilon/dt=656$ c^{-1}
4 -- velocity of the projectile 4.64 m/s, strain rate $d\varepsilon/dt=930$ c^{-1}

$\sigma \cdot 10^8 Pa$
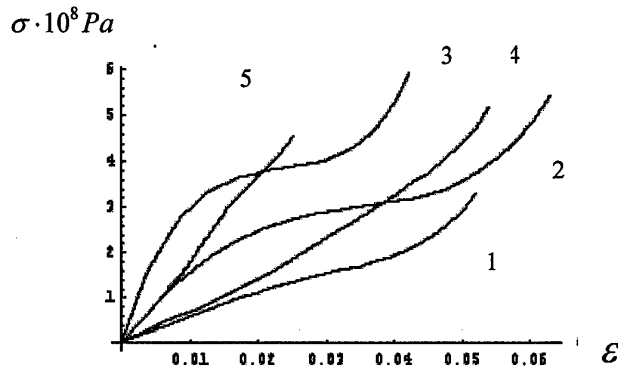
Figure 11.9 Diagram $\sigma - \varepsilon$ for copper (the specimen a26), impacts 1, 2, 3,4,5.
1 -- velocity of the projectile = 3.94 m/s, strain rate $d\varepsilon/dt=759 \ c^{-1}$;
2-- velocity of the projectile 5.03 m/s, strain rate $d\varepsilon/dt=935 \ c^{-1}$
3 -- velocity of the projectile 4.68 m/s, strain rate $d\varepsilon/dt=656 \ c^{-1}$
4 -- velocity of the projectile 4.64 m/s, strain rate $d\varepsilon/dt=930 \ c^{-1}$
5 -- velocity of the projectile 4.09 m/s, strain rate $d\varepsilon/dt=500 \ c^{-1}$
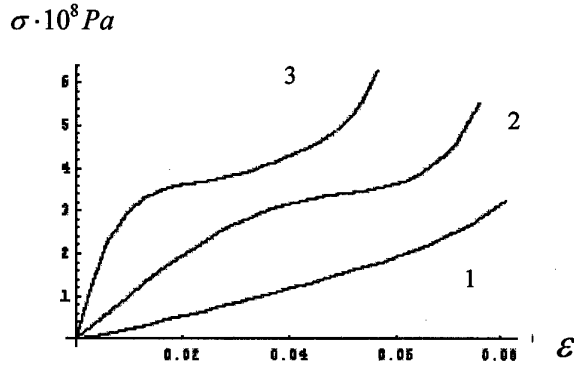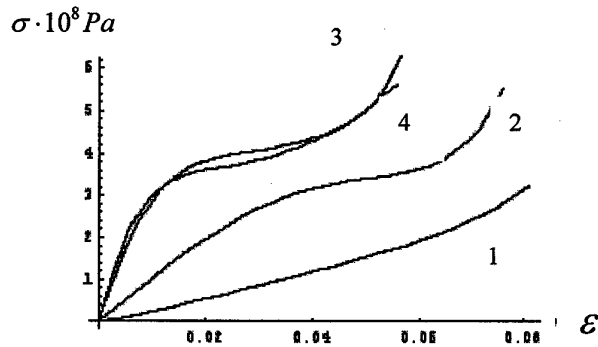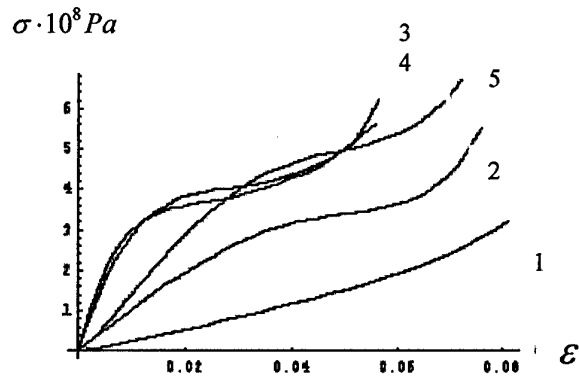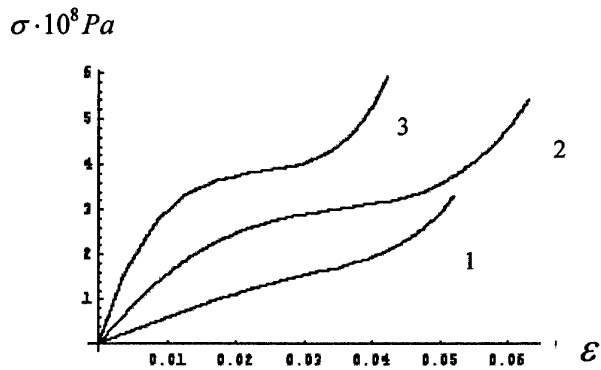
$\sigma \cdot 10^8 Pa$
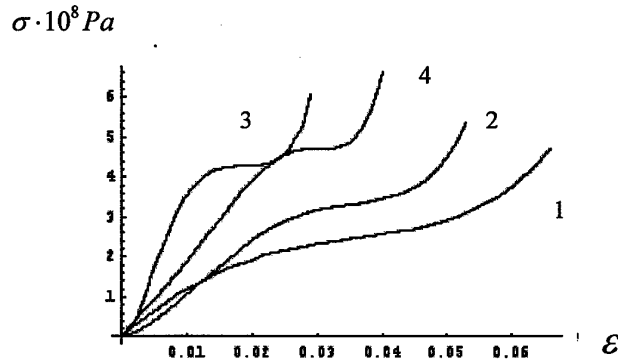
Figure 11.10. Diagram $\sigma - \varepsilon$ for copper (the specimen a29), impacts 1, 2, 3,4.
1 -- velocity of the projectile = 5.71 m/s, strain rate $d\varepsilon/dt=977 \ c^{-1}$;
2-- velocity of the projectile 5.41 m/s, strain rate $d\varepsilon/dt=812 \ c^{-1}$
3 -- velocity of the projectile 5.26 m/s, strain rate $d\varepsilon/dt=450 \ c^{-1}$
4 -- velocity of the projectile 5.68 m/s, strain rate $d\varepsilon/dt=714 \ c^{-1}$

12. MECHANICAL RESPONSES OF SHOCKED MATERIALS

12.1. Constitutive Description of Deformation of Copper Based on the Use of the Mechanical Threshold Stress as an Internal State Variable

The observed change in the strain rate sensitivity at constant strain must then be due to the strain rate sensitivity of structure evolution. Follansbee extended the model proposed by Kocks [80] and Mecking and Kocks [81] into the high strain rate regime in copper. The important feature of the model is that evolution of the internal state variable (structure evolution) is treated separately from the determination of the strain-rate and temperature dependent flow stress for any microstructural state. This treatment was motivated by the observation in polycrystalline copper that the yield stress at any standart strain and temperature on samples prestrained at room temperature to a constant strain varied with strain rate of pre-strain process.

Results in copper [82] have indicated large strain or strain rate history effects. Measurements using the strain change test are usually limited to strain rates $< 10^3 \ s^{-1}$. The availability of mechanical threshold stress data measured in copper at strain rates as high as $10^4 \ s^{-1}$ permits extension of this model into the regime where the strain rate sensitivity (determined at constant strain) is known to increase dramatically. This allows the

proposal and testing of a single model based only on thermal activation controlled glide that describes results over a wide range of strain rates ($10^{-4} \ s^{-1} \leq \dot{\varepsilon} \leq 10^4 \ s^{-1}$).

In the Follansbee model the flow σ stress is determined as the function of mechanical threshold stress (or the flow stress at 0°K) $\hat{\sigma}$.

The mechanical threshold stress is separated into two components,

$$\hat{\sigma} = \hat{\sigma}_a + \hat{\sigma}_t, \tag{12.1}$$

where the component $\hat{\sigma}_a$ characterizes the rate independent interactions of dislocations with long-range barriers such as grain boundaries whereas the component $\hat{\sigma}_t$ characterizes the rate dependent interactions with short range obstacles.

At finite temperature, thermal activation can lead to a lowering of the second component of the flow stress, while leaving the first unchanged. The relation between the flow stress and the mechanical threshold stress becomes

$$\hat{\sigma} = \hat{\sigma}_a + \sigma_t = \hat{\sigma}_a + s(\dot{\varepsilon}, T)\hat{\sigma}_t, \tag{12.2}$$

where the strain rate and temperature dependencies are included in the factor s.

With equation (12.2) as the foundation for a model, there are two separate problems. First, the form of the factor s in equation (12.2) must be specified. Second, evolution of the mechanical threshold stress must be described.

Thermal activation at constant structure

The factor s in equation (12.2) specifies the ratio between the applied stress and the mechanical threshold stress. The value of s is defined by the glide kinetics. This factor is $s < 1$ for thermally activated controlled glide because the contribution of thermal activation energy reduces the stress required to force a dislocation past an obstacle. If deformation is instead in the dislocation drag controlled regime, then an applied stress greater than the mechanical threshold stress is required for continued deformation.

The exact form of the equation relating $\sigma(\hat{\sigma}, \dot{\varepsilon}, T)$ in the transition regime between these two rate controlling deformation mechanisms has been derived in [82].

The results for a copper indicate that at strain rates $\dot{\varepsilon} < 10^4 s^{-1}$ the rate controlling mechanism is thermal activation and that the contribution of dislocation drag is negligible.

In the thermally activated glide regime the interaction kinetics for short range obstacles are described by an Arrhenius expression of the form

$$\dot{\varepsilon} = \dot{\varepsilon}_0 \exp\left[\frac{\Delta G(\sigma_t / \hat{\sigma}_t)}{kT}\right] \tag{12.3}$$

where $\dot{\varepsilon}_0$ is a constant and k is the Boltzmann constant.

For the free energy ΔG the phenomenological relation was proposed [82]

$$\Delta G = g_0 \mu b^3 \left[1 - \left(\frac{\sigma_t}{\hat{\sigma}_t}\right)^p\right]^q, \tag{12.4}$$

where g_0 is a normalized activation energy, which is expected to remain constant providing the obstacle character does not vary, μ is the shear modulus, b is the magnitude of the Burgers vector, and p and q are constants that characterize the (statistically averaged) shape of the obstacle profile ($0 \leq p \leq 1; 1 \leq q \leq 2$) [82].

Combining equations (12.4), (12.3) and (12.2) and the arranging the result gives

$$\sigma = \hat{\sigma}_a + (\hat{\sigma} - \hat{\sigma}_a)\left\{1 - \left[\frac{kT \ln(\dot{\varepsilon}_0/\dot{\varepsilon})}{g_0 \mu b^3}\right]^{1/q}\right\}^{1/p}, \tag{12.5}$$

which is a specific form for the more general equation (12.2). The equation (12.5) express the dependence of flow stress as the function of current structure ($\hat{\sigma}$), strain rate and temperature. However, the evolution of the structure is more difficult and needs more precise study.

Structure Evolution

Structure evolution is considered as the balance between the dislocation accumulation and dynamic recovery. The strain hardening rate $\theta = \frac{d\hat{\sigma}}{d\varepsilon}$ is used to characterize the differential variation of the structure parameter with strain.

The fundamental relation between the competing process is written as

$$\theta = \theta_0 - \theta_r(T, \dot{\varepsilon}, \hat{\sigma}) , \qquad (12.6)$$

where θ_0 is the hardening due to the dislocation accumulation and θ_r is the dynamic recovery rate. Application of this equation to a variety of f.c.c. pure metals and alloys, using the data measured over a wide range of temperatures but a narrow range of strain rates allowed in [82] the conclusion that the first term on the right-hand side of equation (12.6) is roughly constant and equal to $\mu/20$, which is the strain hardening rate during Stage II deformation. According to the model expressed by equation (12.6) the important temperature and strain rate dependencies were found in the dynamic recovery term.

A linear variation of strain hardening rate with stress indicates Voce behavior

$$\theta = \theta_0 \left[1 - \frac{\hat{\sigma} - \hat{\sigma}_a}{\hat{\sigma}_s(T, \dot{\varepsilon}) - \hat{\sigma}_a} \right] , \qquad (12.7)$$

where $\hat{\sigma}_s$ is the stress at zero strain hardening rate (sometimes termed the saturation stress).

Most metals do not show Voce behavior over a wide range of stresses, but saturation-like behavior is common. That is, the strain hardening rate continues to decrease toward zero with increasing stress or strain, but true saturation behavior is rarely observed.

It was assumed in [82] that for the strains $\varepsilon < 1$ the strain hardening curve do saturate with a law given by the equation

$$\theta = \theta_0 \left[1 - F \left(\frac{\hat{\sigma} - \hat{\sigma}_a}{\hat{\sigma}_s - \hat{\sigma}_a} \right) \right] ,$$

where the function F is chosen to fit the measured data.

Results at constant structure

The mechanical threshold stress is measured by deforming several samples identically according to the strain and strain history that was chosen for the testing.

All loading was realized at ambient temperature and the reloading at various temperatures to measure the yield stress as a function of the reload temperature. The mechanical threshold is the flow stress at 0 K. Equation (12.7) provides this extrapolation as it describes in [82].

To fit the reload yield stress data to equation (12.7), the athermal stress was estimated as the yield stress on undeformed material

$$\hat{\sigma}_a = 40 MPa .$$

For the evaluation of the $\dot{\varepsilon}_0$ term in equation (12.7) the rests were performed in some ranges of the strain rates. The best agreement for all of the loading histories and temperatures is given by the value of $\dot{\varepsilon}_0$

$$\dot{\varepsilon}_0 = 10_7 \ s_{-1} .$$

No systematic variation in $\dot{\varepsilon}_0$ with the history was detected. However, as it was emphasized in [82], the low constant-structure rate sensitivity in copper makes it difficult to experimentally determine this quantity with precision.

The normalized activation energy is determined from the slope of the line through the data and the average of all data, which presented in [82] gives

$$g_0 = 1.6 .$$

It was underlined also in [82] the significance of the slight increase in g_0 with increasing $\hat{\sigma}$.

Application of the results to the description of structure evolution

The key of the successful application of equation (12.5) to the description of structure evolution is the choice of the function F. Several functions were investigated [83]. To fit the evolutionary equations to the mechanical threshold stress data the factors θ_0 and σ_s were varied until the lowest error between the experimental data points and the predicted $\hat{\sigma} \sim \varepsilon$ curve was achieved.

The form of the function F finally chosen uses the hyperbolic tangent function and is written as

$$F = \frac{\tanh(2x)}{\tanh 2} ,$$

where $x = \dfrac{\hat{\sigma} - \hat{\sigma}_a}{\hat{\sigma}_s - \hat{\sigma}_a}$.

Combining this expression with equation (12.7) gives

$$\theta = \theta_0 \left[1 - \frac{\tanh(2X)}{\tanh(2)} \right] \tag{12.8}$$

It was emphasize that the particular evolution law chosen to fit the results presented in [82] is merely a convenient mathematical form which happens to describe the data. It is satisfying that equation (12.8) approximates the Voce law at low strains. However, it was underlined that there is no physical significance to the particular form of equation (12.8), and the assumption was expressed concerning the existence of more universal, physically based evolution laws, which could give the fundamental understanding of texture evolution and Stage IV deformation are advanced.

Initial Strain Rate Hardening

A fundamental supposition of Meecking and Kocks [81] is that the initial portion of the stress-strain rate curve is affected strongly by the athermal dislocation accumulation rate, whereas the large strain regime of the strain-stress curve is affected strongly by dislocation rearrangement and therefore the saturation flow stress behavior.

The mechanical threshold stress data show an unusual large strain rate dependence at low strains. This behavior can not be described by the equation

$$\theta = \theta_0 \left[1 - F(\frac{\hat{\sigma} - \hat{\sigma}_a}{\sigma_s - \sigma_a}) \right]$$

unless the initial strain hardening rate is allowed to vary with strain rate. Thus, the observed variation of θ_0 with $\dot{\varepsilon}$ is not a function of the particular evolutionary law chosen.

These data indicate that the increased strain-rate sensitivity found at these strain rates is not due to change in the rate controlling deformation mechanism but rather is a strain rate history effect.

Discussion

The foundation of the Follansbee model is the separation of the constant structure part of the strain-rate sensitivity from the structure evolution part. There are fundamentally different processes, which require different theoretical models.

38

A combination of physically based equations

$$\sigma = \hat{\sigma}_a + (\hat{\sigma} - \hat{\sigma}_a)\left\{1 - \left[\frac{kT \ln(\dot{\varepsilon}_0/\dot{\varepsilon})}{g_0 \mu b_3}\right]^{1/q}\right\}^{1/p},$$

$$\log\left(\frac{\dot{\varepsilon}_0}{\dot{\varepsilon}}\right) = \frac{\mu b_3 A}{kT} \log\left(\frac{\hat{\sigma}_s}{\hat{\sigma}_{so}}\right),$$

and phenomenologically based equation

$$\theta = \theta_0\left[1 - F(\frac{\hat{\sigma} - \hat{\sigma}_a}{\sigma_s - \sigma_a})\right]$$

to describe these processes has been applied and fitted to mechanical threshold stress measurements from strain rates of $10^{-4} - 10^4 \, s^{-1}$.

The major conclusion of this work is that there is strong evidence that the dislocation accumulation rate, or Stage II hardening rate, begins to increase dramatically with a strain rates exceeding $\sim 10^3 \, s^{-1}$. This observation explains the origin of "the increased strain rate sensitivity" of the flow stress at constant strain found in copper and other f.c.c. metals at these strain rates.

One interesting implication of this finding is that at strain rates exceeding $\sim 10^5 \, s^{-1}$ the strain hardening will quickly saturate and the stress-strain behavior will approach perfect plasticity. The reason for this is that the strain rate sensitivity of the athermal hardening rate exceeds the strain rate sensitivity of the saturation stress at high strain rates. There is a limited experimental evidence which supports this prediction.

12.2. Structure of Stress Waves in Solid under Impact Loading

One dimensional plane shock waves have been widely used to study the mechanical response of solids to high velocity deformation. For many materials under a certain range of impact pressures, there exists a two-wave structures of which the first wave, the so-called, elastic precursor, travels at the velocity of sound waves, while the second wave, plastic shock wave, travels at a slower speed which increases with impact pressure. While the full two-wave structure is thus not steady (does not propagate without change of form), each component wave may be treated as steady after sufficient propagation distance.

In the case of the plane wave propagation in z direction the system of constitutive
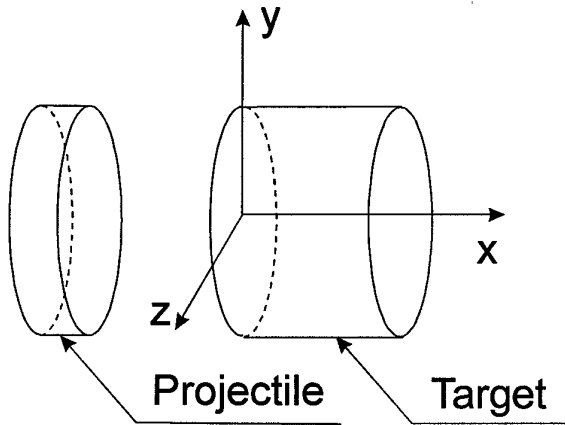
Figure 12.1. Scheme of loading

equations coupled with conservation laws of mass and momentum are written as

$$\dot{\varepsilon}_{zz} = \dot{\varepsilon}_{zz}^e + \dot{p}_{zz} \, , \qquad \dot{\varepsilon}_{zz}^e = \dot{\sigma}_{zz}/E , \qquad\qquad (12.9)$$

39

$$\rho \frac{\partial^2 u_z}{\partial t^2} = \frac{\partial \sigma_{zz}}{\partial z}, \qquad \varepsilon_{zz} = \frac{\partial u_z}{\partial z},$$ (12.10)

$$\frac{\partial p'_{zz}}{\partial t} = -L'_p \frac{\partial F'(p_{zz}, \delta)}{\partial p'_{zz}}, \qquad \frac{\partial p_0}{\partial t} = -L_p^0 \frac{\partial F^0(p_{zz}, \delta)}{\partial p_0}, \qquad \frac{\partial \delta}{\partial t} = -L_\delta \frac{\partial F'(p_{zz}, \delta)}{\partial \delta} .$$ (12.11)

where p'_{zz} and p_0 are deviatoric and isotropic parts of p_{zz}, δ is a parameter reflecting an evolution of equilibrium stress-plastic strain dependence, ρ is material density, L'_p, L_p^0 and L_δ are the kinetic coefficients. There is only p'_{zz} component in the compression waves.

The solution of the system has to satisfy the boundary and initial conditions:

$$\sigma_{zz}(0,t) = \sigma_0(t), \sigma_{zz}(h,t) = 0; v_z(z,0) = \sigma(z,0) = p_{zz}(z,0) = 0; \rho(z,0) = \rho_0,$$ (12.12)

where h is the plate thickness, $\sigma_0(t)$-function was determined on the basis of the solution of collision problem.

12.3.   The Equilibrium Stress-Strain Dependence with Controllable Degree of Metastability

The equilibrium dependence $\sigma(p)$ corresponding to the natural condition of the free energy minimum $\frac{\partial F}{\partial p} = 0$ plays the main role in material response under a slow loading. (The loading with a characteristic time much less than the characteristic time of structure evolution $\tau_p = L_p / G$).

The dependence presented on Fig. 4.1. can be written in form:

$$\sigma(p) = Ap\left(1 + Tanh\left(-L\frac{p - p_c}{p_c}\right)\right) + B\left(1 + Tanh\left(L\frac{p - (p_c + \delta)}{(p_c + \delta)}\right)\right),$$ (12.13)

where $A = \sigma_H / (2p_c)$, $2B$ is the critical stress, p_c is a strain corresponding to the beginning of plastic flow, σ_H is the Hugoniot elastic limit.
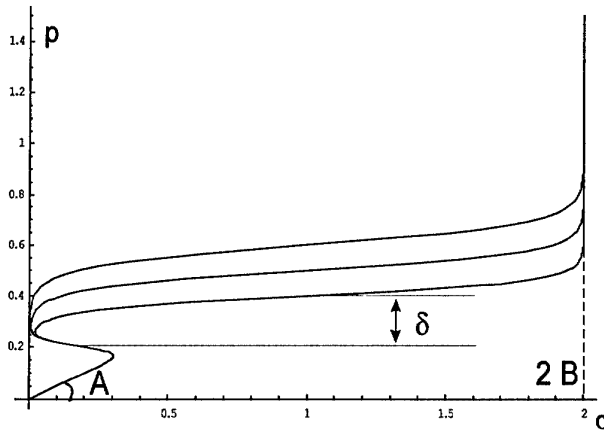
Figure 12.2. The evolution of the equilibrium dependence $\sigma(p)$ on δ. The equilibrium dependence with controllable degree of metastability.

Two type of law were tested for the evolution of the dependence. They can be writing as the following:

$$\dot{\delta}(p) = \dot{\delta}_0 p \text{ and } \dot{\delta}(p) = \dot{\delta}_0 \tanh(p). \tag{12.14}$$

The material parameters for the numerical simulation were determined for pure copper. Using (12.13), the constitutive equations for compressed loading can be written in dimensionless form:

$$\bar{\dot{p}} = -\bar{L}_p \left(\bar{A}\bar{p} \left(1 + Tanh\left(-L\frac{\bar{p}-\bar{p}_c}{\bar{p}_c} \right) \right) + \bar{B}\left(1 + Tanh\left(L\frac{\bar{p}-(\bar{p}_c+\delta)}{(\bar{p}_c+\delta)} \right) \right) - \frac{\bar{\sigma}}{p_{max}} \right), \tag{12.15}$$

where $A=0.6\cdot10^{11}, \bar{A}=\frac{A}{G}=1.54$, $B=2.5\cdot10^9, \bar{B}=Bp_{max}/G=12.82$, $\bar{p}_c = p_c/p_{max} = .1$, $L=7$,

$\bar{L}_p = LL_pG/\sqrt{G/\rho} = 10^2$ $L_p = 2.5\cdot10^{-4}, \bar{\dot{\delta}}_0 = LL_\delta/\sqrt{E/\rho} = 10^2$ $\dot{\delta}_0 = 5\cdot10^{-5}$.

To calculate the face front and rear front of stress wave we introduced in numerical algorithm the dependencies corresponding to loading and unloading conditions. The unloading in point x^* is determined by an inequality $\left.\frac{\partial\sigma}{\partial t}\right|_{x=x^*} < 0$. The rear front dependence were written as

$$\sigma(p) = -A(-p+p_0)\left(1 + Tanh\left(-L\frac{(-p+p_0)-\beta p_c}{\beta p_c} \right) \right) - B\left(1 + Tanh\left(L\frac{(-p+p_0)-(\beta p_c+\delta)}{(\beta p_c+\delta)} \right) \right) + \sigma_0 \tag{12.16}$$

where p_0 and σ_0 are, respectively, the strain and stress corresponding to the beginning of the unloading process, β is parameter describing the Baushinger effect. The "loading- unloading" dependencies are presented on Fig. 12.3.
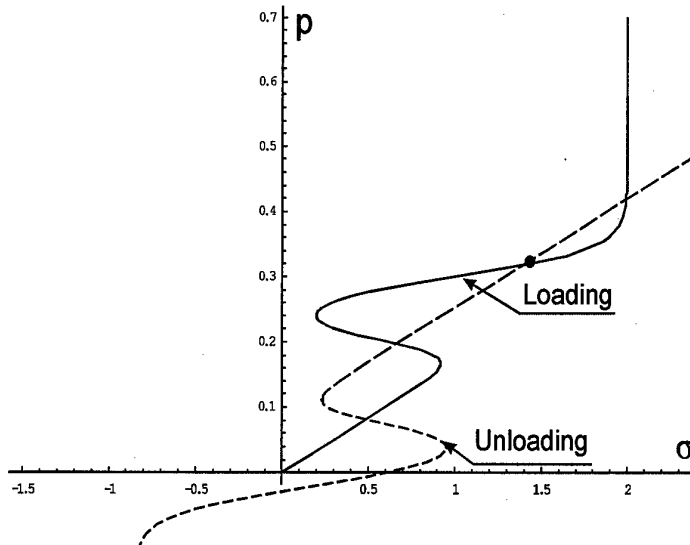
Figure 12.3. "Loading-Unloading" dependencies used in numerical simulation.

Presented in Fig. 12.3 dependencies are the results of numerical simulation of the stress wave propagation and the time-dependencies of stress. In the stress area corresponding approximately to the dynamic yield stress the orientation kinetic transition for the parameter p is realised which results in the abrupt increase in the stress relaxation tempo, a change in the plastic wave profile and the separation of the elastic precursor
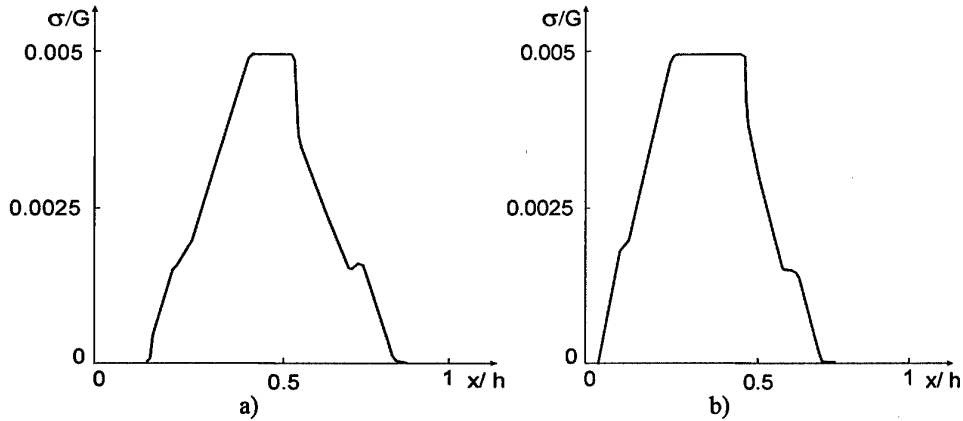
Figure 12.4. The stress profile in specimen for different under laws $\delta = \delta(\mathrm{p})$, *a)* $\dot{\delta}(p) = \dot{\delta}_0 p$ *b)*

$\dot{\delta}(p) = \dot{\delta}_0 \tanh(p)$. *Stress amplitude is 20 10^7 Pa, loading time 10^{-5} sec.*

15.3. The Landau Expansion.

The generalization of Ginzburg-Landau approach for system described by two interacting structural parameters (p and δ in our case) is an important problem under investigation of non-equilibrium systems. The main problem in this approach is the determining the law for $\delta(p)$. The equilibrium dependence was presented in the form:

$$\sigma(p) = Ap + Bp^3 + C_0 \frac{\delta - \delta_1}{\delta_2 - \delta_1} p^5, \qquad (12.17)$$

where A, B, C - constants determined as follow: $A = \dfrac{30\sigma_H}{23 p_c} = 1.56522 e11$,

$B = -\dfrac{10\sigma_H}{23 p_c^3} = -2.0869 e17$, $C_0 = \dfrac{3\sigma_H}{23 p_c^5} = 2.50435 e23$.

The dependence $\sigma(p)$ is presented on Fig. 12.5.
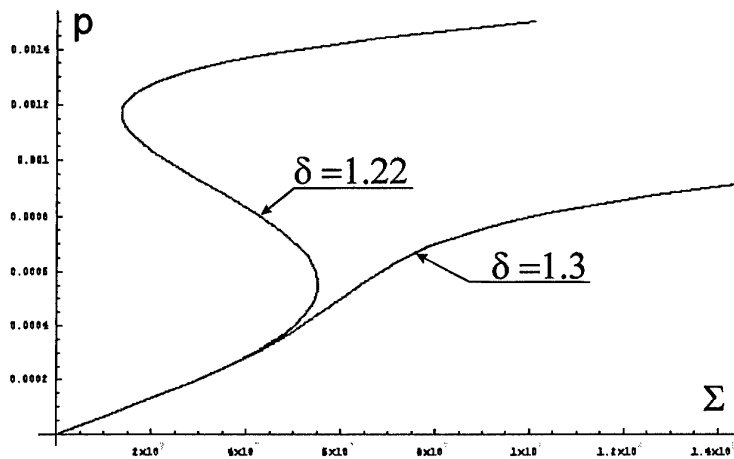
Figure 12.5. Dependence $\sigma(p)$ *on* δ *(The Landau expansion).*

For the determination of current value of δ instead of an analytical dependence $\delta(p)$ we proposed special numerical procedure based on double using of Newton's technique for non-linear algebraic equation. The procedure used the follow dependence $\delta(\sigma)$:

$$\dot{\delta}(\sigma) = \dot{\sigma}\tanh\left(\alpha(\sigma - \sigma_e)\right).$$

Using (12.7) the constitutive equations (12.1) for compressive loading were written in dimensionless form:

$$(\bar{p})_{\bar{t}} = -\bar{L}_p\left(\bar{A}\bar{p} + \bar{B}(\bar{p})^3 + \bar{C}_0\frac{\delta - \delta_1}{\delta_2 - \delta_1}(\bar{p})^5 - \bar{D}\bar{\sigma}\right),$$

where $\quad \bar{p} = p/p_{max}$, $\quad \bar{\sigma} = \sigma/G$, $\quad \bar{t} = tc/L_0$, $\quad A = 1.5522 \cdot 10^{11}$, $\bar{A} = \dfrac{A}{G} = 4.01338$;

$B = -2.08696 \cdot 10^{17}$, $\quad \bar{B} = Bp_{max}^2/G = -1.3378$, $\quad C = 2.50435 \cdot 10^{23}$, $\quad \bar{C}_0 = C_0 p_{max}^4/G = 0.401338$,

$D = 1$, $\quad \bar{D} = D/P_{max} = 2000$, $\quad \bar{L}_p = LL_p G/\sqrt{G/\rho} = 74.6897$ $\quad L_p = 2\,10^{-4}$, $\quad c$ is sound velocity, L_0 is space scale.

To calculate the front and back fronts of stress wave we introduced in numerical algorithm "loading" and "unloading" equilibrium dependencies (Fig. 5.) corresponding to loading and unloading conditions. The unloading in point x^* is determined by an inequality $\left.\dfrac{\partial\sigma}{\partial t}\right|_{x=x^*} < 0$. The "back" dependence can be written as

$$\sigma(p) = A\left(p - (p_0 - p_*)\right) + B\left(p - (p_0 - p_*)\right)^3 + C_0\frac{\delta - \delta_1}{\delta_2 - \delta_1}\left(p - (p_0 - p_*)\right)^5 - \sigma_0,$$

where $\quad p_* = \sqrt{\dfrac{\sqrt{9B^2 - 20AC} - 3B}{10C}} - \varepsilon$ is an auxiliary parameter, p_0 and σ_0 are, respectively, the strain and stress corresponding to the beginning of the unloading process.
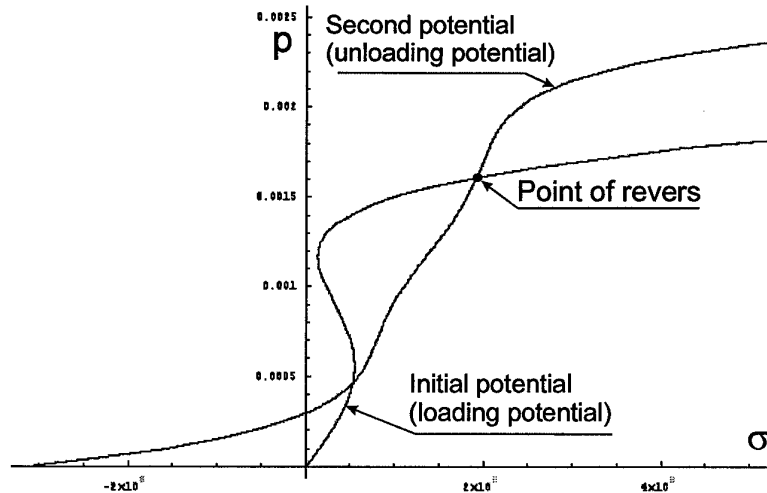
Figure 12.6. "Loading" and "Unloading" dependencies used in numerical simulation.

The results of numerical simulation are presented on Fig 12.7 and 12.8.
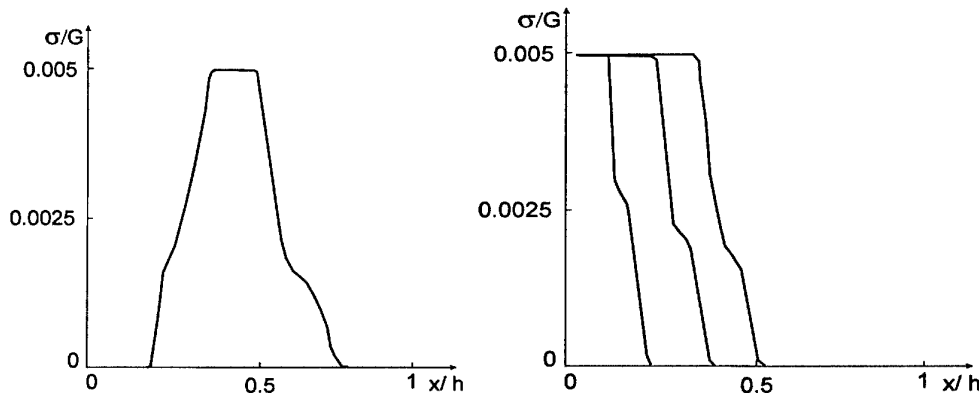
Figure 12.7. The stress profile in specimen a) stress amplitude $2 \cdot 10^8 Pa$, loading time 10^{-6} sec, b) elastic precursor decay (stress amplitude $2 \cdot 10^8 Pa$, loading time 10^{-7} sec).
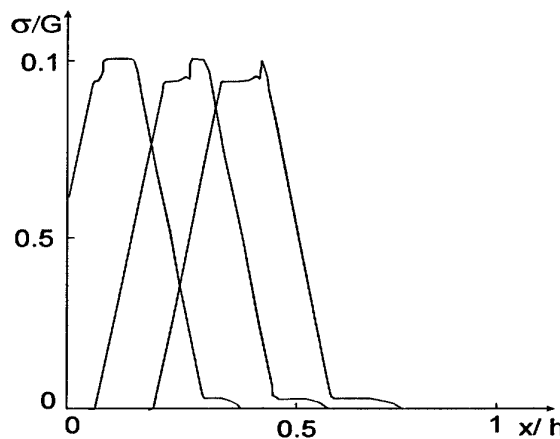
Figure 12.8. The stress profile in specimen a) stress amplitude is $3 \cdot 10^9 Pa$, loading time $6 \cdot 10^{-8} s$.

13. EVALUATION OF THE BODNER - PARTOM MODEL AT HIGH STRAIN RATES

13.1. Constitutive Equations for Elastic-Plastic Strain-Hardening Materials

The state variable model of Bodner and Partom [84] was formulated for the description of visco-plastic material responses with a broad range of load histories and found the wide application for the strain rate loading in the test were high enough to assume relevance to impact loading about 500 to 10^5 s^{-1} and range of stress states that are typical for split Hopkinson bar (SHB) (one-dimensional stress) and flat plate impact (one dimensional strain). The attractive features of the Bodner-Partom (B-P) model are the ease of determination of parameter values and adaptivity to finite difference and finite element computer codes. The basis of the formulation is the separation of the total deformation rate into elastic and inelastic components hat are functions of state variables and the deformation at all stages of loading and unloading. The theory does not require a yield criterion or loading and unloading conditions. The response of the system is calculated on a step-by-step basis and does not depend on reference integration from the "zero" state or the introduction of "memory" functions.

The total strain rate is assumed to be decomposable into elastic and inelastic components

$$\dot{\varepsilon}_{ik} = \dot{\varepsilon}_{ik}^e + \dot{\varepsilon}_{ik}^p \tag{13.1}$$

Both are nonzero for all lading-unloading conditions. The elastic strain rate is related to the stress rate by the elastic constants (Hooke's Law). The inelastic strain rate is assumed to be related to the stress through the flow rule of classical plasticity and is a function of stress, σ_{ik}, a state variable, Z, and to follow the Prandtl-Reuss rule

44

$$\dot{\varepsilon}_{ij}^{p} = \lambda S_{ij},$$
(13.2)

where $\dot{\varepsilon}_{ij}^{p}$ and S_{ij} are the deviatoric plastic strain rate and stress. Squaring equation (13.2) gives

$$\lambda^2 = D_2^p / J_2$$
(13.3)

where

$$D_2^p = \frac{1}{2} \dot{\varepsilon}_{ik}^p \dot{\varepsilon}_{ik}^p$$
(13.4)

is the second invariant of the plastic deformation rate deviator and J_2 is the second invariant of the stress deviator

$$J_2 = \frac{1}{2} \sigma_{ik}' \sigma_{ik}'.$$
(13.5)

Since D_2^p is the measure of the "effective" inelastic shear deformation rate and J_2 is the effective shear stress, the statement

$$D_2^p = f(J_2)$$
(13.6)

can be considered to be multimensional generalization of the uni-axial result. This hypothesis is motivated by the extensive work in the field of dislocation theory, which has shown that the dislocation velocity and therefore the uniaxial plastic strain rate is a function of the stress. The form of equation (13.6) that allows for flexibility in modeling actual material response and has a physical basis is

$$D_2^p = D_0 \exp\left[-\left(\frac{Z^2}{3J_2} \right)^n \right].$$
(13.7)

The material constants for equation (13.7) are D_0, n, and Z. The constant D_0 is the bound on D_2^p for large J_2 and influences the rate sensitivity, n is related to the steepness of the curve and therefore to the sharpness of yielding and also to the rate-sensitivity, and Z corresponds in a general way to the yield stress since the maximum slope occurs at $J_2 = Z^2/3$.

Work hardening corresponds to increased resistance to plastic flow, which means that D_2^p should vary inversely with the measure of strain hardening. The most significant and simplest state variable to present this property for straining histories having a constant sign of the stress is the plastic work W_p [86]. The latter seems to have a sounder physical basis and Z was proposed in the form

$$Z = Z_1 + (Z_0 - Z_1) \exp\left(-mW_p \Big/ Z_0 \right)$$
(13.8)

as the solution of the kinetic equation

$$\dot{Z} = m(Z_1 - Z)\dot{W}_p,$$
(13.9)

where Z_1, Z_0 and m are new material constants. A finite upper limit for Z is required since otherwise D_2^p would approach zero for large W_p. This would correspond to fully elastic behavior and an upward turning stress-strain curve at large strains, which is unrealistic. The proposed strain hardening law corresponds to isotropic hardening and therefore would not characterize the Baushinger effect.

13.2. The Bodner-Partom Model Simulation of Plate Impact Test for Copper

The split Hopkinson bar and plate impact tests are the principal technique employed to evaluate the B-P parameters under uniaxial stress and one dimensional strain conditions. The SHB can operate in compression or tension. The bar design and analysis procedure are described in Section 11.

Plate impact tests are used to observe very high strain rate yield behavior. In these tests, a flat flyer plate is made to impact against a target plate at a high velocity. Compressive stresses are produced and transmitted immediately from the plane of impact to the adjacent stress free areas of the material in the form of a stress pulse. Measurement of the free surface velocity on the rear of the target provides data for the loading (compression) and unloading (release) paths.

The plate impact tests are conducted to measure the Hugoniot elastic limit (HEL), which is the principal stress component under one dimensional strain at very high strain rates. The HEL is related under one dimensional stress (Y_0) by

$$Y_0 = \frac{\sigma_{HEL}}{\dfrac{K}{2G} + \dfrac{2}{3}},$$

where K and G are the bulk modulus and shear modulus, respectively.

Simulation of the plate impact test was aided by simulations with the original finite difference code. The plate impact test is investigated as the propagation of plane elastic-plastic wave in plane specimen in the z-direction. The statement of problem includes the mass and momentum conservation laws and constitutive equations for elastic and plastic strain rates

$$\frac{\partial \rho}{\partial t} = -\frac{\partial}{\partial z}(\rho v_z), \tag{13.10}$$

$$\frac{\partial (\rho v_z)}{\partial t} = -\frac{\partial}{\partial z}(\rho v_z^2 - \sigma_{zz}) \tag{13.11}$$

$$\dot{\varepsilon}_{zz} = \dot{\varepsilon}_{zz}^e + \dot{\varepsilon}_{zz}^p, \tag{13.12}$$

$$\dot{\varepsilon}_{zz}^e = \dot{\sigma}_{zz}/G, \tag{13.13}$$

$$\dot{\varepsilon}_{zz}^p = D_0 \exp\left[-\frac{1}{2}\left(\frac{Z^2}{3J_2}\right)^n\right]\frac{1}{\sqrt{J_2}}\sigma_{zz}', \tag{13.14}$$

where $J_2 = \frac{1}{2}\sigma_{ik}'\sigma_{ik}'$,

The conditions of plastic incompressibility and the elastic dilatation have the forms

$$\dot{\varepsilon}_{xx}^p + \dot{\varepsilon}_{yy}^p + \dot{\varepsilon}_{zz}^p = 0. \tag{13.15}$$

$$\sigma = K\varepsilon, \tag{13.16}$$

Kinetic equation for the hardening parameter Z was used as

46

$$\dot{Z} = m(Z_1 - Z)\dot{W}_p,$$ (13.17)

where $\dot{W}_p = \sigma_{ik}\dot{\varepsilon}_{ik}^p$.

Dynamic loading on the plate was introduced as the boundary conditions:
Loading surface, $z = 0$:

$$\sigma_{zz}(0,t) = f(t).$$ (13.19)

The function $f(t)$ describes the loading pulse with the shape close to rectangular.

Free surface, $z = h$:

$$\sigma_{zz}(h,t)=0.$$ (13.20)

The solution must satisfy to the following initial conditions:

$$v_z(z,0) = \sigma_{zz}(z,0) = \dot{\varepsilon}_{zz}^p(z,0) = 0,$$
$$Z(z,0) = Z_0$$ (13.21)
$$z \in [0,1], t \in [0,\infty).$$

The definition of (13.5) gives

$$J_2 = 4.5(\sigma_{zz}')^2,$$ (13.22)

that leads to presentation of the rate of plastic work

$$\dot{W}_p = 1.5\sigma_{zz}\dot{\varepsilon}_{zz}^p$$ (13.23)

Here are : ρ is specific density of material; t is time; z is the direction of wave propagation in the plate; v_z is the velocity component; $\sigma_{ik}, \sigma_{ik}', \dot{\varepsilon}_{ik}, \dot{\varepsilon}_{ik}^e, \dot{\varepsilon}_{ik}^p$ - are the components of stress, deviatoric stress, strain rate, elastic and plastic strain rates consequently; σ is the mean stress; G, K are shear and elastic modulus; h is the plate thickness.

Numerical simulation of the plate impact test was carried out by the finite element method. The following constants for a copper were used:

$$\rho = 8.6 \cdot 10^3 \ kg/m^3, \ G = 0.408 \cdot 10^{11} \ Pa, \ K = 1.45 \cdot 10^{11} \ Pa;$$
$$D_0 = 1.72 \cdot 10^7 \ s^{-1}, \ n = 0.4, \ m = 1.4 \cdot 10^{-8} \ J^{-1}, \ Z_1 = 65.5 \cdot 10^8 \ Pa.$$

Results of Numerical Simulation

The results of numerical simulation are presented in Fig. 1-3 for the initial pulse amplitude $\sigma_0 = 3.0 \cdot 10^9 \ Pa$, the pulse duration $\Delta t_0 = 0.25 \cdot 10^{-6} s \ s$ and the plate thickness $h = 5.0 \cdot 10^{-3} m$. The elastic-plastic wave propagation is accompanied by the relaxation of the deviatoric stress component for the stress close to the Hugoniot and the separation of wave on the elastic precursor and plastic wave front. The step appears on the back front corresponding to the elastic and then plastic unloading.

The accuracy of the numerical procedure was estimated by the variation in the large scale of the finite difference parameters.
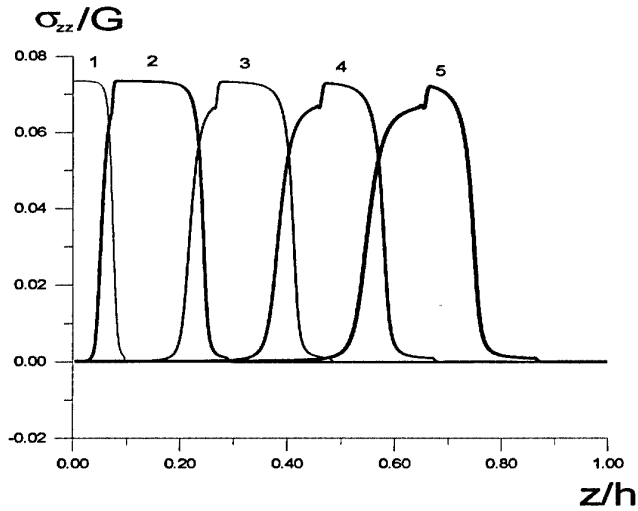
Figure 13.1. Propagation of plane stress wave σ_{zz} in plate for the moment of time:

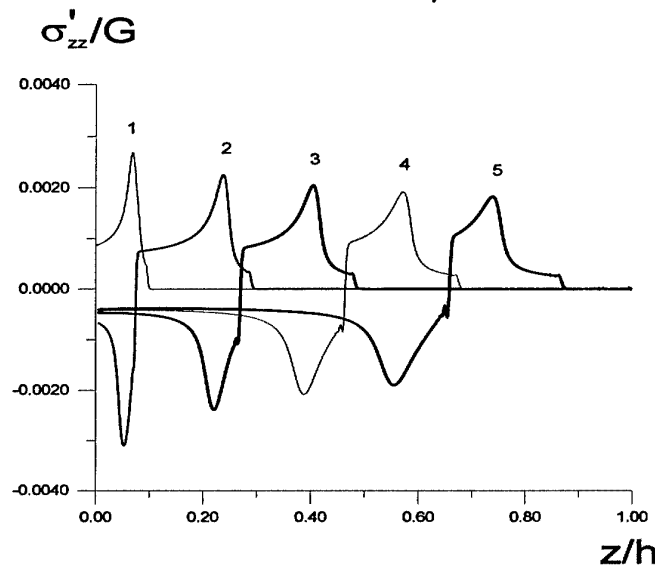*t=0.1; 0.3; 0.5; 0.7; 0.9 μs*

Figure 13.2. Evolution of deviatoric component of stress σ'_{zz} for different time t=0.1; 0.3; 0.5; 0.7; 0.9 μs.
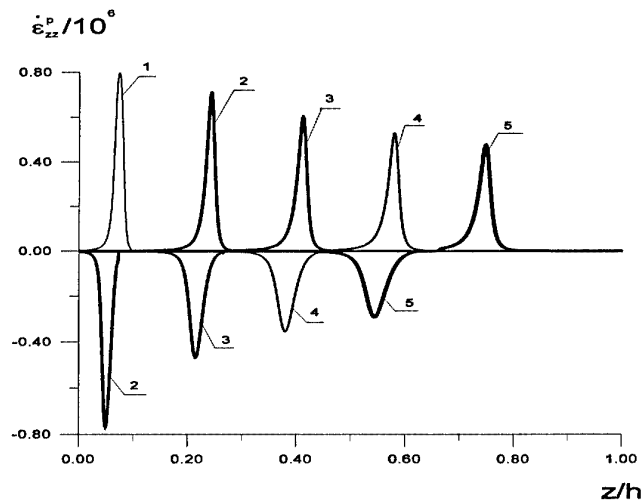

Figure 13. 3. Evolution of plastic strain $\dot{\varepsilon}^p_{zz}$ in time: t=0.1; 0.3; 0.5; 0.7; 0.9 μs

48

The Discussion of Results

Numerical study of the evolution of the stress wave front showed the qualitative and quantitative agreement given by the B-P model for a copper in dynamic test. The elastic precursor appears at stress level amplitude that is much less the total stress level. Similar situation was observed experimentally in [79], when the appearance of the elastic precursor was not measured. Most clear two-wave picture of elastic-plastic front is observed for deviatoric stress component, where the kinetics of the elastic precursor decay can be estimated. The decay of elastic precursor is the consequence of elastic-viscoplastic relaxation presented in the B-P model. The evolution of deviatoric parts of stress and strain in Fig. 13.3 confirmed this physical reason of relaxation of stress-strain variables in the B-P model.

The rate of decay of the amplitude of the leading elastic wave front in a stress wave propagation experiment can be used to deduce the form of the strain rate sensitivity of a material. Extensive numerical analysis of precursor decay was conducted in [87], where a mathematical definition of the HEL, the amplitude of the leading elastic wave under uni-axial strain conditions. The proposed definition of the HEL determines the amplitude of the HEL as the stress corresponding to a plastic strain of 0.0002 in the direction of the propagating wave. It should be noted that the amplitude of the HEL is often considered to be a material constant. The decrease in amplitude in the B-P model is a direct result of the rate sensitivity of material.

The positive feature of the B-P model is that there is no yield surface and no unloading condition. Thus, plastic flow is always nonzero but the yield behavior is modeled numerically using the property that the plastic strain rate is computationally small for low values of stress.

The plastic strain invariant D_2^p is taken in the form (13.7), where Z is the hardening parameter. A finite upper limit for Z is required since otherwise D_2^p would approach zero for large W_p. This corresponds to fully elastic behavior and an upward turning stress-strain curve at large strains which is unrealistic. A nonzero value of D_2^p for large W_p leads to the slope of the stress-strain curve approaching zero as the strains become large. The proposed strain-hardening law corresponds to isotropic hardening and therefore would not characterize the Baushinger effect.

A particularly attractive features of the B-P model are the ability for modeling high strain rate behavior, that is in the consistent with experimental observations which show that flow stresses increase very rapidly with increase in strain rate for strain rates above $10^4 \ s^{-1}$ for polycrystalline metals. The hardening term Z can be thought is usually taken to be in the range $10^6 - 10^8 \ s^{-1}$ for the problems involving very high strain rates.

14. SUMMARY

With the aim to establish the linkage of nonlinear behavior of the defect ensembles with relaxation properties (plasticity) and failure of solid microscopic and statistical theory was developed and phenomenological models of deformation and failure of dynamically and shock loaded materials were proposed. The microscopic model reflects the results of experimental study of defect evolution in the large range of strain-rate with the usage of X-ray and light microscopy method, defect induced density measurement, including the experiments «in-situ».

Multifield statistical approach is developed for the study of multiscale nature of plastic deformation and failure. The tensor order parameter, the defect density tensor, is introduced for typical mesoscopic defects, microcracks, microshears, that are the structural image of dislocation substructures of different material scales. Statistical model has established the existence of dimensionless structural parameter of scaling which provides the linkage of continuous growth of the defect density under deformation and the rescaling of structural level that is involved in the successive mechanism of momentum transfer due to the collective motion of defects. This parameter represents the ratio of the current scale of dislocation substructure and the distance between substructures. The statistical model revealed the variety in behavior of ensembles of mesoscopic defects caused by the interaction of defects with an external field and between defects. The collective properties of defects due to their interaction play most important role in the formation of large scale mesodefect substructures, and finally in the mechanisms of plastic flow and failure. The generation of large scale mesodefect substructure is realized as the orientation transition in the low scale mesodefect substructure. This transition occurs in the course of the excitation in material the auto-solitary strain waves with a front length corresponding to the orientation transition area. The important consequence of this result is the conclusion that the plastic flow develops as the continuous orientation ordering of dislocation substructures. The driving force of this transition is the free energy release in the conditions of growth of the defect density and the rescaling of structural level of material which provides the optimal mechanism of the momentum transfer.

The orientation transitions in mesodefect ensembles and the nucleation of spatial areas with pronounced orientation of defects can be considered as mechanisms of adiabatic shear bands and the strain localization. The spatial distribution of the initial susceptibility in term of above scaling parameter can lead to the multiply generation of the set of collective modes (auto-solitary strain waves) in the bulk of the specimen. These modes can be considered as new phase variables which subject the material behavior and decrease the system symmetry. The irregular character of plastic deformation (Yerrky flow) is the consequence of the stochastic dynamics due to the generation and the interaction of autosolitary collective modes in mesodefect system. The important result of statistical multifield theory is the determination of the type of bifurcation, which leads to qualitative change for the evolution equation of defect density tensor under the transition from plastic mechanism of structural relaxation to the damage localization and failure. This bifurcation type arises for the critical value of scaling parameter and leads to the generation of the collective modes – the dissipative structures with blow-up kinetics of the defect density growth on the corresponding spatial scales. The set of these collective modes correspond to the coordinates of the second attractor which defines another multiscale nature f damage-failure transition.

The collective mesoscopic modes of dislocation substructures (auto-solitary orientation waves and blow-up dissipative structures) have the meaning of the self-similar solution – eigen-function spectrum of corresponding nonlinear problems. The loading condition can provide the resonance excitation of this type of collective modes that can lead to the anomalous deformation responses in the form of specific type of strain rate localization, failure wave, self-similar structures of wave fronts in shocked condensed matter.

Statistical approach based on the solution of the multiparticle problem of the behavior of ensemble of mesoscopic defects (microcracks, microshears), characterizing by tensor order parameter (defect density tensor) , allowed the establishment the characteristic type of the non-linearity of thermodynamic potential (free energy) in the terms of deformation induced by the defects. Non-linearity type of the thermodynamic potential and derived evolution equation for macroscopic variable, related to the defect, explained the mechanisms of plastic strain instability as the non-equilibrium orientation transition and the kinetics of the transition from damage to failure due to the generation of localized structures in defect ensembles. Study of the properties of evolution equations showed the linkage of above nonlinear regimes with self-similar solutions having the nature of autosolitary waves of orientation transition, which determines the dynamics of the fronts of localized plasticity, and the dissipative blow-up structures related to the nucleation of failure hotspots.

Theoretical results related to the explanation of the linkage of the nonlinear defect kinetics and relaxation properties, failure allowed the interpretation and the description of essentially non-equilibrium effects that are observed under dynamically loaded and shocked materials.

The main results in this area are:

The explanation of the finite range of the Hugoniot elastic limits as the consequence of the existence of the orientation metastability area for the mesodefect ensemble.

The explanation of universality (the self-similarity) of steady-state plastic front for the strain rates $\dot{\varepsilon} \to 10^5 s^{-1}$ (the Barker-Grady data) as the consequence of penetration into the orientation metastability limit and the realization of the sequence of orientation transitions in the defect ensembles in the conditions of the self-organized criticality.

The explanation of mechanism of generation and propagation of failure waves in shocked glasses and ceramics as the consequence of the resonance excitation of localized blow-up modes in defect ensembles.

The explanation of the temporal regularities of failure in the stress waves (dynamic branch) including the multiply spall failure, as the consequence of the resonance excitation of above localized modes.

The explanation of the mechanism of transition from the steady-state crack propagation to the branching regime and the fragmentation due to the subjection of material behavior to the spectrum of localized blow-up collective modes of defects at the crack tip area.

The explanation of the scaling nature, including the scaling of fracture surface roughness, as the consequence of the symmetry properties of system «solid with defects» due to the subjection of their behavior to the spectrum of the collective modes of localized failure.

The developed approach and the continuum models of materials with defects were tested for the description of structure of stress waves and failure under impact loading and for dynamic crack propagation. The comparison of developed model (in the following ICMM-Model) with conventionally used models (Follansbee-MTS Model, Bodner-Partom Model) was carried out. Due to the analysis the following conclusion was made:

The correspondence of athermic and thermally dependent thresholds for MTS Model to the stress thresholds corresponding to the orientation metastability range.

The nonlinear hardening law (Voce law) in the MTS model is the consequence of characteristic type of the non-linearity in the area of orientation transition.

The difference of the hardening kinetics in the Bodner-Partom Model and the kinetics proposed in MTS Model and ICMM -Model of solid with defects.

The limited applicability of MTS Model, Bodner-Partom Model model for the description of the localization effects under dynamic and shock wave loading, the transitions from the elastic precursor to the plastic front, the relaxation of the elastic precursor and the plastic strain instability (adiabatic shear bands).

The following experiments were carried out for the verification of the ICMM-Model:

The study of nonlinear dynamics of crack propagation in the preloaded PMMA plate with the aim to support the mechanism of the transition from the steady-state crack propagation to the branching and the following fragmentation, the estimation of the critical velocities of crack propagation. Experiments were carried out with the usage of high speed digital camera REMIX (time lag between pictures $10\,\mu s$), the photoelasticity method, and under the recording with the usage of the laser system of stress phase portrait (the Poincare cross-section) at the vicinity of crack tip.

The study of fracture surface scaling (after the crack propagation in PMMA) and at the free surfaces of the strained copper specimens subjected to the quasi-static shear and dynamic Hopkinson-bar compression. Experiments were carried out with the usage of High Resolution Scanning System «New View» with the resolution $10\,nm$ with the aim to support the role of collective modes of defects in the development of localized plasticity and failure.

15. REFERENCES

1. Koneva, N.A., Lychagin, S.P., Trishkona, L.T. and Kozlov, E.V., In: *Strength of Metals and Alloys, Proceedings of the 7-th International Conference*, Montreal, Canada, v.1, 21 (1985).
2. Hansen, N. and Kuhlmann-Wilsdorf, D., *Materials Science and Engineering*, 81, 141 (1986).
3. Betechtin, V.I, Naimark, O.B. and Silbershmidt, V.V., In: *Proceedings of Int. Conf. of Fracture (ICF 7)*, 6, 38 (1989).
4. Betechtin, V.I. and Vladimirov, V.I., In: *Problems of Strength and Plasticity of Solids, Zhurkov*, S.N. (Ed.). Nauka, Leningrad, 142 (1979).
5. Naimark, O.B., In:*Proceedings of the IUTAM Symposium on Nonlinear Analysis of Fracture*, J.R.Willis (Ed). Kluver Academic Publishers, Dordrecht, 285-298 (1997).
6. Barenblatt, G.I. and Botvina, L.R., *Izv. AN. SSSR, Mech. Tv. Tela*, 4, 161 (1983), (in Russian).
7. Kadic, A. and Edelen, G.B., Lecture Notes in Physics, No 174, Springer, Berlin (1983) .
8. Raikher, Yu.L. and Shliomis M.I., In: *Relaxation Phenomena in Condensed Matter*, W.Coffey (Ed.), Advances in Chemical Physics Series, vol.LXXXVI, John Willey&Sons, 595 (1994).
9. Leontovich, M.A., *Introduction to Thermodynamics, Statistical Physics*, Chapter 3, Nauka, Moscow (1983).
10. Naimark, O.B. and Silbershmidt, V.V., *Eur.J.Mech., A/Solids*, 10, 607 (1991).
11. Landau, L.D. and Lifshitz, E.M. *Course of Theoretical Physics. Statistical Physics*, Pergamon Press, Oxford, (1980).
12. Naimark, O.B., *JETP Letters*, 67, 9, 751 (1998).
13. Kurdjumov, S.P., In: *Dissipative Structures and Chaos in Non-Linear Space*, Utopia, Singapure, 1, 431 (1988).
14. Fineberg, J., Gross, S.P. and Sharon, E., In: *Proceedings of the IUTAM Symposium on Nonlinear Analysis of Fracture*, J.R.Willis (Ed). Kluver Academic Publishers, Dordrecht, 177 (1997).
15. Ravi-Chandar, K. and Knauss, W.G., *Int. J. Fracture* 26, 65 (1982).
16. Freund, L.B., *Dynamic Fracture Mechanics*, Cambridge University Press, Cambridge, England (1990).
17. Fineberg, J., Gross, S., Marder, M. and Swinney, H., *Phys.Rev.Lett.*, 67, 457 (1991).
18. Sharon, E., Gross, S.P. and Fineberg, J., *Phys.Rev.Lett.*, 74, 5096 (1995).
19. Boudet, J.F., Ciliberto, S. and Steinberg, V., *J. de Physique*, 6, 1493 (1993).
20. Sharon, E., Gross, S.P., Fineberg, F., *Phys.Rev.Lett* , 76, 2117 (1996) .
21. Holian, B.L., Thomson, R., *Phys. Rev.*, E, 56, 1, 1071 (1997).
22. Griffith, A.A. *Phil.Trans. of the Royal Society*, London, A221, 163 (1921).
23. Mott, N.F., *Engineering*, 165, 16, (1948).
24. Irwin, G.R., *Journal of Applied Mechanics*. 24, 361 (1957).
25. Barenblatt, G.I., *Advances in Applied Mechanics*, 7, 55 (1962).

26. Rice, J.R., *Journal of Applied Mechanics*, **35**, 37 (1968).

27. Frenkel, Ya.I., *Journal of Technical Physics*, **22**, 11, 1857 (1952)

28. Naimark, O.B., Davydova, M.M. and Plekhov, O.A., In: *Proceedings of NATO Workshop "Probamat – 21 Century"*, G.Frantziskonis (Ed.). Kluwer, 127 (1998).

29. Naimark, O.B., Davydova, M.M., Plekhov O.A. and Uvarov, S.V., *Physical Mesomechanics*, **2**, 3, 47 (1999).

30. Naimark, O.B., Davydova, M.M. and Plekhov, O.A., *Computers and Structures*, **76**, 67 (2000).

31. Naimark, O.B., In: *Proceedings of EUROMAT 2000. Advances in Mechanical Behavior. Plasticity and Damage* (plenary lecture), D Miannay, P.Costa, D. Francois, A.Pineau (Eds.), Elsevier, 1, pp.15-28 (2000).

32. Mandelbrot, B.B., Passoja, D.E. and Paullay, A.J. *Nature*, **308**, 721 (1984).

33. Bouchaud, E., In: *Proceedings of IUTAM Symposium "Size-Scale Effects in Failure Mechanisms of Materials and Structures"*, A. Carpinteri (Ed.). Kluwer, 121 (1996).

34. Mecholsky, J.J., In: *Strength of Inorganic Materials*, C.R.Kurkjian (Ed.). Plenum Press, New York, 569 (1995).

35. Feder, J., *Fractals*, Plenum Press, New York and London (1988).

36. Naimark, O.B., Davydova, M.M., *J. de Physique III*, **6**, 259 (1996).

37. Galin, L.A. and Cherepanov, G.P., Sov. Phys. *Doklady*, **167**, 543 (1966).

38. Bourne, N., Millett, J., Rosenberg, Z. and Murray, N., J.Mech.Phys.Solids, **46**, 1887 (1998).

39. Rasorenov, S.V., Kanel, G.J., Fortov V.E. and Abasenov, M.M., *High Press. Res.*, **6**, 225 (1991).

40. Nikolaevskii, V.N., *Int. J. Engng. Sci.*, **19**, 41(1981).

41. Brar, N.K. and Bless, S.J., *High Press.Res.*, **10**, 773 (1992).

42. Bourne, N., Rosenberg, Z., Field, J.E., *J. Appl. Phys.* **78**, 3736 (1995).

43. Dandekar, D.P. and Beaulieu, P.A., In: *Metallurgical and Materials Applications of Shock-Wave and High-Strain-Rate Phenomena*, L.E. Murr, K.P. Staudhammer and M.A.Meyers (Eds.), Elsevier Science B.V., 211 (1995).

44. Bourne N.K., Rosenberg, Z., Field, J.E. and Crouch, I.G., *J. Physique IV, Colloq.C* **8**, 635(1994).

45. Gibbons, R.V., Ahrens, T.J., *J. Geophys. Res.* **76**, 5489 (1971).

46. Glifton, R.J., *Appl. Mech. Rev.* **46**, 540 (1993).

47. Naimark, O.B., In: *Proceedings of IX Int. Conference of Fracture, Sydney* (key-note lecture), B. Karihaloo (Ed.), **6**, 2795 (1997).

48. Plekhov, O.A., Eremeev, D.N. and Naimark, O.B., *J. Physique IV Colloq C.* **10**, 811 (2000).

49. Beljaev, V.V.and Naimark O.B., *Sov. Phys. Doklady.*, **312**, 2, 289 (1990).

50. Bellendir, E., Beljaev, V.V. and Naimark, O.B., *Sov. Tech. Phys. Lett.*, **15**, 3, 90 (1989).

51. Grady, D.E., *J. AppL. Phys.*, **53**, 322 (1982).

52. Kipp, M.E. and Grady D.E., *J. Mech. Phys. Solids*, **33**, 399 (1986).

53. Glenn, L.A. and Chudnovsky, A., *J. Appl. Phys.*, **59**, 1379 (1986).

54. Grady, D.E., *J. Mech. Phys. Solids*, **36**, 353 (1988).

55. Grady, D.E. and Kipp, M.E., *J. Appl. Phys.*, **58**(3), 1210 (1985).

57 Grady, D.E., *J. Appl. Phys.*, **68**, 6099 (1990).

58. Grady, D.E., *Fragmentation By Blasting*, Fourney and Costin (Eds.), Experimental Mechanics, Brookfield Center, 63 (1985).

59. Senf, H., Strauburger, E. and Rothenhausler, H., In: *Metallurgical and Material Applications of Shock Wave and High Strain-Rate Phenomena*, L.E. Murr, K.P. Staudhammer and M.A.Meyers (Eds.), Elsevier Science B.V., 163 (1995).

60. Naimark, O.B. and V.V.Belayev, V.V., *Physics of Combustion and Explosion*, **25**, 115 (1989).

61. Sakharov, A.D., Zaidel R.M., Mineev, V.N. and Oleinik A.G., *Sov.Phys.Dokl.* **9**, 1091 (1965); Mineev V.N. and Savinov, E.N, *Sov.Phys. JETP* **25**, 411 (1967); Mineev, V.N and Zaidel R.M., *Sov.Phys. JETP* **27**, 874 (1968).

62. Band, W. and Duval, G.E., *Amer. J. Phys,* **29**, 780 (1961).

63. Wallace, D.C., *Phys. Rev.*, B **24**, 5597 (1981) ; B **24**, 5607 (1981).

64. Barker, L.M., *Behavior of Dense Media Under High Pressures*, Gordon and Breach, New York, p.483 (1968).

65. Lord Rayleigh, *Proc.R. Soc.London*, **84**, 247 (1910).

66. Taylor,G.I., *Proc. R. Soc. London*, **84**, 371 (1910).
67. R. Von Mises, J.Aero.Sci, **17**, 551 (1950).
68. Lighthill, M.J., *Surveys in Mechanics*, Cambridge University, Cambridge, England, pp.250-351 (1965).
69. Swegle, J.W. and Grady, *D.E., J.Appl.Phys.*, **58**(2) (1985).
70. Naimark O.B., *Sov.Tech. Phys. Lett.* **23** ,7, 529 (1997).
71. Frenkel Ja.I, *Kinetic Theory of Liquids*, Clarendon Press, Oxford (1946).
72. B.V.Derjagin *et al.*, *Polymer*, **30**, 1 (1989).
73. Carlson, D.R, Widnall, S.E. and Peeters, M.F., *J. Fluid Mech.* **121**, 487 (1982).
74. Zaslavskii, G.M. and Sagdeev, R.Z., *Introduction to Nonlinear Physics* [in Russian], Nauka, Moscow (1988).
75. Klimontovich, Yu.L., *Physica* **B 229**, 51 (1996).
76. Nicholas, T.and Rajendran, A.M., In : High Velocity Impact Dynamics, Ed. J.A.Zukas, Willey, 127 (1990).
77. Follansbee, P.S. , Analysis of Strain Rate Sensitivity at High Strain Ratesin FCC and BCC Metals, Mechanical Properties of Materialsat High Rates of Strain, Ed.J.Harding, The Institute of Physics Publishing Ltd, 213-220(1989) .
78. Cheval, F. and Priester, L., Effect of Strain Rate on the Dislocation Substructurein Deformed Copper Polycrystals, Scripta Metall, 23, 1871-1876 (1989).
79. Duffy, J., Strain Rate History Effects and Dislocation Substructure at High Strain Rates, Material Behavior Under High Stress and Ultrahigh Loading Rates, Eds. J.Mescall and V.Weiss, N.Y., Plenum Press, 21-37 (1983).
80. Kocks, U.F., ASME J.Engn.Mat.Tech., 98, 76 (1976).
81. Mecking, H. and Kocks, U.F., Acta Metall., 29,1865 (1981).
82. Follansbee, P.S.,The Rate Dependence of Structure Evolutionin Copper and its Influence on the Stress-Strain Behavior at Very High Strain Rates, In: Impact Loading and Dynamic Behavior of Materials, DGM Informationgesselshaft Verlag, Germany, Vol.1, Eds. C.Y.Chiem,H.-D. Kunze, and L.W.Meyer, p.315 (1988).
83. Follansbee, P.S., The HEL and Rate-Dependent Yield Behavior, n: Shock Compression of Condensed Matter, Elsevier Science Publishers B.V, Eds. S.C,Schmidt, J.N.Johnson, L.W.Davison (1990).
84. Rajendran, A.M., Bless S.J., and Dawicke D.S., Evaluation of Bodner-Partom Model Parameters at High Strain Rate, ASME J.Eng.Mat.Tech., 108,75-80 (1986).
85. Bodner, S.R. and Y.Partom, Y., Constitutive Equations for Elastic –Viscoplastic Strain-Hardening Materials", J.Appl.Mech., Trans ASME,42,385-389 (1985).
86. Hill, R., *The Mathematical Theory of Plasticity*, Clarendon Press, Oxford (1950).
87. Nicholas, T.A., Rajendran A.M. and Grove, D.J., An Offset Yield Criterion from Precursor Decay Analysis, Acta Mech., 69, 205-218.

The main algorithm

Begin

Variables: $\sigma(x,t)=0, p(x,t)=0, \delta(x,t)=\delta_0$

$t=0, x=0$

p
calculation

$\sigma(x,t)<\sigma_H$

testing of local
loading condition

0

1

1

stress
calculation

0

delta
calculation

$x+=dx<L$

0

1

$t+=dt<T$

0

1

End
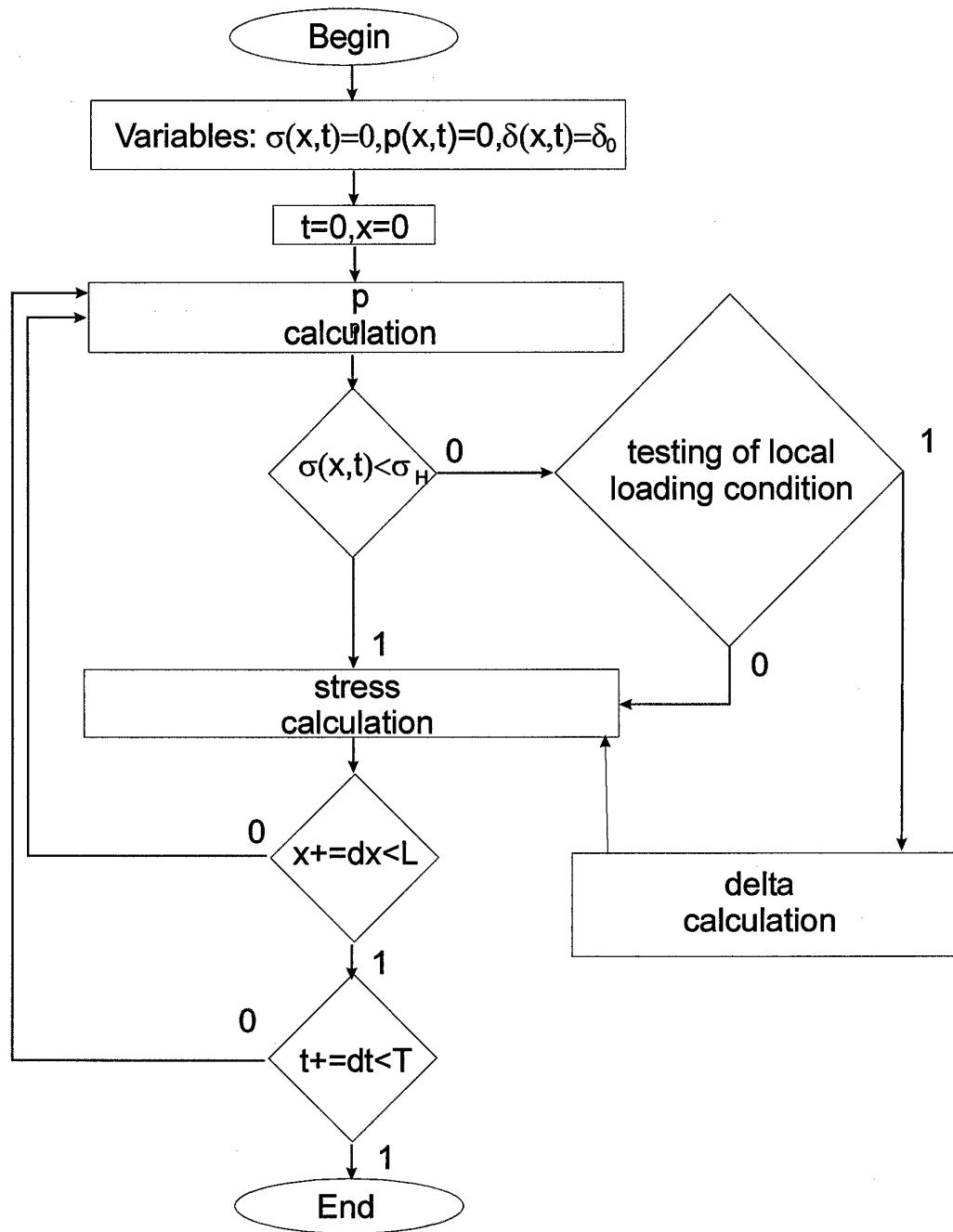
Testing of local loading condition

Comments

pointrevers(x)[1] -new stress revers
pointrevers(x)[0] - new strain revers
pointrevers(x)[2] - old delta revers

pointrevers(x)[3]=1 - point with coordinate x is unloading
pointrevers(x)[3]=0- point with coordinate x is loading

pointrevers(x)[5] - old strain revers
pointrevers(x)[6] - old stress revers

```
                    testing of local
                    loading condition
                           |
                           v
         1        +------------------+
     +<-----------|  pointrevers(x)[3]=1  |
     |            |       and         |
     |            |     dσ/t>0        |
     |            +------------------+
     |                     | 0
     |                     v
     |            +------------------+      1    +------------------+
     |            |  pointrevers(x)[3]=0  |--------->| Is there plasticity |
     |            |       and         |          |  flow? (δ!=δ´)      |
     |            |     dσ/t<0        |          +------------------+
     |            +------------------+           1 |            | 0
     |                     | 0                     v            v
     |                     v              +-----------------+  +------------------+
     |                  return 1          | poitnrevers(x)[3]=1 |  | poitnrevers(x)[3]=0 |
     |                                    |                 |  | recovery of old    |
     v                                    | save of current |  | potensial          |
+------------------+                      | potensial       |  | parameters         |
| Is there plasticity |                   | parameters      |  +------------------+
|  flow? (δ!=δ´)      |                   |                 |
+------------------+                      | recovery of old |
 1 |            | 0                       | potensial       |
   v            v                         | parameters      |
+-----------+  +------------------+       +-----------------+
| poitnrevers|  | poitnrevers(x)[3]=0 |
| (x)[3]=0   |  | recovery of old    |
|            |  | potensial          |
| save of    |  | parameters         |
| curent     |  +------------------+
| potensial  |
| parameters |         return 0
|            |
| recovery of|
| old        |
| potensial  |
| parameters |
+-----------+
```

Delta calculation

```
┌──────────────────┐
│      delta       │
│   calculation    │
└──────────────────┘
         │
         ▼
┌────────────────────────────────────┐
│ Variables: beta=0.01, precision=1e-6 │
└────────────────────────────────────┘
         │
         ▼
┌────────────────────────────────────┐
│    Newton's method for solving     │
│    the equation σ=F(p,deltaold)    │
│            return p0               │
└────────────────────────────────────┘
         │
         ▼
┌──────────────────────┐
│   deltanew=deltaold  │
└──────────────────────┘
         │
         ▼
┌──────────────────────┐
│         i=0          │
└──────────────────────┘
         │
         ▼
┌────────────────────────────────────┐
│    Newton's method for solving     │
│    the equation σ=F(p,deltanew)    │
│            return p                │
└────────────────────────────────────┘
         │
         ▼
┌──────────────────────────────────────────────┐
│ deltanew=deltaold+beta*(fabs(p-p0)-dpequlibrium) │
└──────────────────────────────────────────────┘
```

Decision nodes:

- `fabs(deltanew-deltaold)<precision and i<N` — 0 (left), 1 (right)
- `i<1` — 1 (up to precision/=2), 0 (right)
- `i>N` — 1 (up to beta*=2), 0 (right to return deltanew)

- `precision/=2`
- `beta*=2`

return deltanew

Unit12.cpp listing:

```cpp
//------------------------------------------------------------------------
#include <vcl.h>
#pragma hdrstop

#include "Unit1.h"
//------------------------------------------------------------------------
#pragma package(smart_init)
#pragma resource "*.dfm"

#include <math.h>

TForm1 *Form1;
//------------------------------------------------------------------------
__fastcall TForm1::TForm1(TComponent* Owner)
     : TForm(Owner)
{
}
//------------------------------------------------------------------------

void __fastcall TForm1::FormCreate(TObject *Sender)
{
  int i;

  Image1->Canvas->Brush->Color=clWhite;
  Image1->Canvas->Pen->Color=clRed;

  // Source
  A0=1.56522e11;
  B0=-2.08696e17;
  C0=2.50435e23;
  D0=1;
  Le=7;
  pc=0.5e-3;
  //constans of material
  M=1e4;
  E=3.9e10;
  ro=8.94e3;
  nu=0.345;
  //size of area
  L=0.1e-2;
  // kinetic constans
  Lp=7e-1;
  Lp1=7e-1;
  LDl=1e-4;

  Pmax=0.5e-3;
  delta1=1.1;
  delta2=1.3;

  N=2500; // Number of nodes
  h=1./N;
  tau=3e-5;
  Sect=30;

//------------------------------------------------------------------------/

  InitStress=.0000;
  MaxStress=2e9/E;
```

```
ImpactTime1=0.06e-6*sqrt(E/ro)/L;
ImpactTime2=0.03e-6*sqrt(E/ro)/L;

A=A0/E;
B=B0*Pmax*Pmax/E;
C=C0*Pmax*Pmax*Pmax*Pmax/E;
D=D0/Pmax;
Lp=L*Lp*E/sqrt(E/ro);
Lp1=L*Lp1*E/sqrt(E/ro);
LDl=L*LDl*E/sqrt(E/ro);
pc=pc/Pmax;

Fx=(9.*B*B-20.*A*C<0)?sqrt((-3*B)/(10*C)):sqrt((-sqrt(9.*B*B-20.*A*C)-3*B)/(10*C));
FFx=A*Fx+B*Fx*Fx*Fx+C*Fx*Fx*Fx*Fx*Fx;

  FlagOnTerminate=false;

PrevStress=new double[N];// Stress
for(i=0;i<N;i++)
 PrevStress[i]=InitStress;
CurStress=new double[N];
for(i=0;i<N;i++)
 CurStress[i]=InitStress;
NextStress=new double[N];


PrevP=new double[N];// Damage parameter
for(i=0;i<N;i++)
 PrevP[i]=0;
CurP=new double[N];
for(i=0;i<N;i++)
 CurP[i]=0;
NextP=new double[N];
for(i=0;i<N;i++)
 NextP[i]=0;

// Structural parameter
CurDl=new double[N];
for(i=0;i<N;i++)
 CurDl[i]=delta2;
NextDl=new double[N];
for(i=0;i<N;i++)
 NextDl[i]=delta2;

beta=new double[N];
for(i=0;i<N;i++)
 beta[i]=0.02;

al=new double[N];
for(i=0;i<N;i++)
 al[i]=0;

bt=new double[N];
for(i=0;i<N;i++)
 bt[i]=0;

PointRevers=new double*[N];
for(i=0;i<N;i++)
 {
 PointRevers[i]=new double[7];
```

```
    for(int j=0;j<7;j++) PointRevers[i][j]=0;
    PointRevers[i][2]=delta2;
    }

  CurTime=0.;
  Selastic=FFx/D;
  Pelastic=5e-4/Pmax;
  xr=0;
  fr=0;
  dl=delta2;
  p0=0;
  }
//-----------------------------------------------------------------

void __fastcall TForm1::StartClick(TObject *Sender)
{
  FlagOnProcess=true;

  Solving();
  Plot();

  FlagOnProcess=false;
}
//-----------------------------------------------------------------
double TForm1::SourceP(int i)
  {
  double koef=1.1;
  double S=CurStress[i],P=CurP[i];
  int Nin=5000;
  double dt=tau/Nin;
  double r=0,r1=0;

  fr=PointRevers[i][1];
  xr=PointRevers[i][0];
  dl=CurDl[i];

  double eps=1e-7;
  double epstec=1e-7;

  if(fr!=0) koef=1;

  if(fabs(S-fr)>koef*Selastic)
    Lpp=Lp1;
  else  Lpp=Lp;

   P=P+xr;
   r=CurP[i];
  double kr1,kr2,kr3,kr4;

  for(int j=0;j<Nin;j++)
    {
  kr1=Lpp*(D*(S-fr)-(A*P+B*P*P*P+C*(dl-delta1)*P*P*P*P*P/(delta2-delta1)));
  P=r+dt/2*kr1+xr;
  kr2=Lpp*(D*(S-fr)-(A*P+B*P*P*P+C*(dl-delta1)*P*P*P*P*P/(delta2-delta1)));
  P=r+dt/2*kr2+xr;
  kr3=Lpp*(D*(S-fr)-(A*P+B*P*P*P+C*(dl-delta1)*P*P*P*P*P/(delta2-delta1)));
  P=r+dt*kr3+xr;
  kr4=Lpp*(D*(S-fr)-(A*P+B*P*P*P+C*(dl-delta1)*P*P*P*P*P/(delta2-delta1)));
  r1=r+dt/6*(kr1+2*kr2+2*kr3+kr4);
  P=r1+xr;
```

```cpp
    if(fabs(r-r1)<eps)
    return r;
    r=r1;
      }
    return r;
    }
//--------------------------------------------------------------------------
double TForm1::Sourcedl(int i,double dp,double k)
    {
    double dold=0,dnew=0;
    double poldtec=1,pnewtec=0;
    double eps=(1e-8)*k*dp,epstec=1e-7;
    double S,zeroit;
    int flagenter=1;
    int n=10;

    fr=PointRevers[i][1];
    xr=PointRevers[i][0];
    dl=CurDl[i];
    S=CurStress[i];

    zeroit=(CurStress[i]<fr)?-300:300;
    if (fabs(eps)<1e-15) return dl;
    if(CurDl[i]==delta2) beta[i]=0.01;
    do{
    eps/=2;
    do{
    if(flagenter != 1) beta[i]/=5;
    if(n<1) {beta[i]=0.02;}
    flagenter=0;
    n=0;
    poldtec=pnewtec=zeroit;
      do{
        poldtec=pnewtec;
        pnewtec=poldtec-(A*(poldtec+xr)+B*(poldtec+xr)*(poldtec+xr)*(poldtec+xr)+(C*(dl-
delta1)*(poldtec+xr)*(poldtec+xr)*(poldtec+xr)*(poldtec+xr)*(poldtec+xr))/(delta2-delta1)-D*(S-
fr))/(A+3*B*(poldtec+xr)*(poldtec+xr)+(5*C*(dl-
delta1)*(poldtec+xr)*(poldtec+xr)*(poldtec+xr)*(poldtec+xr))/(delta2-delta1));
      }while(fabs(poldtec-pnewtec)>epstec);

    p0=pnewtec;
    dold=dnew=dl;
    do{
      dold=dnew;
      poldtec=pnewtec=zeroit;
      do{
       poldtec=pnewtec;
        pnewtec=poldtec-(A*(poldtec+xr)+B*(poldtec+xr)*(poldtec+xr)*(poldtec+xr)+(C*(dold-
delta1)*(poldtec+xr)*(poldtec+xr)*(poldtec+xr)*(poldtec+xr)*(poldtec+xr))/(delta2-delta1)-D*(S-
fr))/(A+3*B*(poldtec+xr)*(poldtec+xr)+(5*C*(dold-
delta1)*(poldtec+xr)*(poldtec+xr)*(poldtec+xr)*(poldtec+xr))/(delta2-delta1));
      }while(fabs(poldtec-pnewtec)>epstec);
      dnew=dold+beta[i]*(fabs(pnewtec-p0)-k*dp);
      }while((fabs(dold-dnew)>eps)&&(n++<=1000));
    }while(n>1000);
    }while(n<1);
    return dnew;
    }
//--------------------------------------------------------------------------
void TForm1::CheckRefers(int i)
```

```
    {
    double keycon=0.01;
    static double rememberPr=0;

    if((PointRevers[i][4]==1)&&(fabs(CurStress[i]-PrevStress[i])<keycon*tau)) return;
    PointRevers[i][4]=0;

    if((PointRevers[i][3]==0)&&((CurStress[i]-PrevStress[i])<=rememberPr))
      {
      if(CurDl[i]==delta2)
        {
        PointRevers[i][0]=PointRevers[i][5];
        PointRevers[i][1]=PointRevers[i][6];
        CurDl[i]=NextDl[i]=PointRevers[i][2];
        PointRevers[i][3]=1;
        PointRevers[i][4]=1;
        }
       else{
      PointRevers[i][5]=PointRevers[i][0];
      PointRevers[i][6]=PointRevers[i][1];
      PointRevers[i][2]=CurDl[i];
      PointRevers[i][3]=1;
      PointRevers[i][0]=-CurP[i]+Fx;
      PointRevers[i][1]=CurStress[i]-FFx/D;
      CurDl[i]=NextDl[i]=delta2;
      PointRevers[i][4]=1;
       }
      return;
      }
    if((PointRevers[i][3]==1)&&((CurStress[i]-PrevStress[i])>=rememberPr))
      {
      if(CurDl[i]==delta2)
        {
        PointRevers[i][0]=PointRevers[i][5];
        PointRevers[i][1]=PointRevers[i][6];
        PointRevers[i][3]=0;
        CurDl[i]=NextDl[i]=PointRevers[i][2];
        PointRevers[i][4]=1;
        }
       else{
      PointRevers[i][5]=PointRevers[i][0];
      PointRevers[i][6]=PointRevers[i][1];
      PointRevers[i][2]=CurDl[i];
      PointRevers[i][3]=0;
      PointRevers[i][0]=-CurP[i]+Fx;
      PointRevers[i][1]=CurStress[i]-FFx/D;
      CurDl[i]=NextDl[i]=delta2;
      PointRevers[i][4]=1;
       }
      return;
      }
    PointRevers[i][4]=0;
    rememberPr=(CurStress[i]-PrevStress[i])/100;
    }
//-------------------------------------------------------------------------

void TForm1::Solving()
{
  const double Z=1./(1-2*nu*nu/(1-nu)),K=Z*(1-nu/(1-nu))*Pmax;
  const int SN=8e4; // Not greater than 2e10
```

```
int i,j,k,m,MaxPosition;
double koef=1;

PrevTime=CurTime;
MaxPosition=ProgressBar1->Max;
ProgressBar1->Position=0;
for(k=0;k<SN+1;k++)
 {
 // Next layer for P and dl
    for(i=0;i<N;i++)
      {
      NextP[i]=SourceP(i);
      if(fabs(CurStress[i]-PointRevers[i][1])>=Selastic)
        {
      CheckRefers(i);
      if(PointRevers[i][4]==0)
      NextDl[i]=Sourcedl(i,2.3e+3*pow(fabs(CurStress[i]-
PrevStress[i])*pow(tanh(3e3*(fabs(CurStress[i]-PointRevers[i][1])-Selastic)),1),1),1.);
      }
      }

   // Next layer for stress
   for(i=1;i<N-1;i++)
   {
   NextStress[i]=(Z*(tau/h)*(tau/h))*(CurStress[i+1]-2.*CurStress[i]+CurStress[i-1])-
   K*(NextP[i]-2.*CurP[i]+PrevP[i])+2*CurStress[i]-PrevStress[i];
   }


   // Boundary conditions
   NextStress[N-1]=InitStress;
   if(CurTime<(2.*ImpactTime1+ImpactTime2))
   {
    if(CurTime<ImpactTime1)
    {
     NextStress[0]=((MaxStress-InitStress)/ImpactTime1)*CurTime+InitStress;
    }
    else
    {
     if(CurTime<(ImpactTime1+ImpactTime2))
       NextStress[0]=MaxStress;
     else
       NextStress[0]=2.*(MaxStress-InitStress)-((MaxStress-InitStress)/ImpactTime1)*(CurTime-
ImpactTime2)+InitStress;
    }
   }
   else
    NextStress[0]=InitStress;

   CurTime=PrevTime+tau*k;

   xr=PointRevers[Sect][0];
   fr=PointRevers[Sect][1];
   dl=CurDl[Sect];

   ProgressBar1->Position=((double)(1./SN)*(k+1)*MaxPosition);
   if(FlagOnTerminate)
   {
    k=SN+1;
```

```
    FlagOnTerminate=false;
    }
    Application->ProcessMessages();

    for(i=0;i<N;i++)
    {
      PrevStress[i]=CurStress[i];
      CurStress[i]=NextStress[i];
      PrevP[i]=CurP[i]; CurP[i]=NextP[i];
      CurDl[i]=NextDl[i];
    }
    }
    ProgressBar1->Position=0;
}
//-------------------------------------------------------------------------
void __fastcall TForm1::FormClose(TObject *Sender, TCloseAction &Action)
{
  delete[] PrevStress;
  delete[] CurStress;
  delete[] NextStress;
}
//-------------------------------------------------------------------------
void __fastcall TForm1::Timer1Timer(TObject *Sender)
{
  if(FlagOnProcess)
    Plot();
}
//-------------------------------------------------------------------------
void TForm1::Plot()
{
  int i;
  int left,top;
  double vscale,hscale;

  Clear();

  EditTime->Text=FloatToStr(CurTime*L/sqrt(E/ro));

  left=10;
  top=Image1->Height-30;
  vscale=((double)top-10.)/MaxStress;
  hscale=((double)Image1->Width-20.)/N;

  Image1->Canvas->Pen->Color=clRed;
  Image1->Canvas->MoveTo(left,top-CurStress[0]*vscale);
  for(i=1;i<N;i++)
   Image1->Canvas->LineTo(left+hscale*i,top-vscale*CurStress[i]);


  Image1->Canvas->Pen->Color=clBlue;
  vscale=2.e1;
  Image1->Canvas->MoveTo(left,top-0.1*CurP[0]*vscale);
  for(i=1;i<N;i++)
   Image1->Canvas->LineTo(left+hscale*i,top-0.1*vscale*CurP[i]);

}
//-------------------------------------------------------------------------
void TForm1::Clear()
{
  TRect r;
```

```
  r.left=0;//Image1->Left;
  r.right=Image1->Width;
  r.top=0;//Image1->Top;
  r.bottom=Image1->Height;

  Image1->Canvas->FillRect(r);
}
//---------------------------------------------------------------------

void __fastcall TForm1::ButtonTerminateClick(TObject *Sender)
{
  FlagOnTerminate=true;
}
//---------------------------------------------------------------------

void __fastcall TForm1::ButtonExitClick(TObject *Sender)
{
  exit(1);
}
//---------------------------------------------------------------------
```

Unit12.dfm listing:

```
object Form1: TForm1
  Left = 241
  Top = 235
  BorderIcons = [biSystemMenu, biMinimize]
  BorderStyle = bsSingle
  Caption = 'PlateImpact'
  ClientHeight = 454
  ClientWidth = 599
  Color = clBtnFace
  Font.Charset = DEFAULT_CHARSET
  Font.Color = clWindowText
  Font.Height = -11
  Font.Name = 'MS Sans Serif'
  Font.Style = []
  OldCreateOrder = False
  OnClose = FormClose
  OnCreate = FormCreate
  PixelsPerInch = 96
  TextHeight = 13
  object Image1: TImage
    Left = 8
    Top = 8
    Width = 585
    Height = 369
  end
  object Label1: TLabel
    Left = 95
    Top = 431
    Width = 26
    Height = 13
    Caption = 'Time:'
  end
  object Start: TButton
    Left = 360
    Top = 392
    Width = 73
    Height = 25
    Caption = 'Start'
    TabOrder = 1
    OnClick = StartClick
  end
  object ProgressBar1: TProgressBar
    Left = 7
    Top = 399
    Width = 325
    Height = 13
    Min = 0
    Max = 399
    Smooth = True
    Step = 1
    TabOrder = 2
  end
  object EditTime: TEdit
    Left = 136
    Top = 426
    Width = 150
    Height = 21
    TabStop = False
```

```
    ReadOnly = True
    TabOrder = 0
  end
  object ButtonExit: TButton
    Left = 512
    Top = 392
    Width = 73
    Height = 25
    Caption = 'Exit'
    TabOrder = 3
    OnClick = ButtonExitClick
  end
  object Timer1: TTimer
    Interval = 100
    OnTimer = Timer1Timer
    Left = 272
    Top = 152
  end
end
```

Unit12.h listing

```cpp
//----------------------------------------------------------------
#ifndef Unit1H
#define Unit1H
//----------------------------------------------------------------
#include <Classes.hpp>
#include <Controls.hpp>
#include <StdCtrls.hpp>
#include <Forms.hpp>
#include <ExtCtrls.hpp>
#include <ComCtrls.hpp>
#include <fstream.h>
#include <Math.h>
//----------------------------------------------------------------
class TForm1 : public TForm
{
__published:        // IDE-managed Components
    TImage *Image1;
    TButton *Start;
    TTimer *Timer1;
    TProgressBar *ProgressBar1;
    TEdit *EditTime;
    TLabel *Label1;
    TButton *ButtonExit;
    void __fastcall FormCreate(TObject *Sender);
    void __fastcall StartClick(TObject *Sender);
    void __fastcall FormClose(TObject *Sender, TCloseAction &Action);
    void __fastcall Timer1Timer(TObject *Sender);
    void __fastcall ButtonTerminateClick(TObject *Sender);
    void __fastcall ButtonExitClick(TObject *Sender);
private:  // User declarations
    bool FlagOnProcess,FlagOnTerminate;
    int N;
    double h,tau,CurTime,ImpactTime1,ImpactTime2,PrevTime;
    double InitStress, MaxStress;
    double *PrevStress,*CurStress,*NextStress,*CorP;
    double *PrevP,*CurP,*NextP;
    double *CurDl,*NextDl,*beta,*al,*bt;
    double A0,B0,C0,D0,C1,delta1,delta2,delta,Fx,FFx,GestStr,Q;
    double M,E,ro,nu,L,Lp,Lpp,Lp1,LDl,Pmax;
    void Solving();
    void Plot();
    void Clear();
    void CheckRefers(int i);
    double SourceP(int i);
    double Sourcedl(int i,double dp,double k);
public:             // User declarations
    double **PointRevers;
    double A,B,C,D,Le,pc;
    double xr,fr,dl;
    double p0;
    double Selastic,Pelastic;
    int Sect;
    fstream fin,fint;
    __fastcall TForm1(TComponent* Owner);
};
//----------------------------------------------------------------
extern PACKAGE TForm1 *Form1;
//----------------------------------------------------------------
#endif
```